# Spin Hall Effect Induced Ferromagnetic Resonance in Permalloy/Platinum Bilayers

Shigeyuki Hirayama

April 2018

# Spin Hall Effect Induced Ferromagnetic Resonance in Permalloy/Platinum Bilayers

Shigeyuki Hirayama

Submitted to the Graduate School of
Pure and Applied Sciences
in Partial Fulfillment of the Requirements
for the Degree of Doctor of Philosophy in
Engineering

at the
University of Tsukuba

# Contents

## Abstract

## 1 Introduction

## 2 Experimental Methods

## 3 Interface Perpendicular Magnetic Anisotropy of Ta/Py/Pt Layers

## 4 ST-FMR Measurement in Py/Pt Films at $\theta$=10° and 45°

## Abstract

Spintronics is the combined research field of the magnetics and electronics because the degrees of freedom of the spin and charge of the electron are utilized and manipulated in the emerging field. So far, there have been several practical devices proposed and launched, and this research field has contributed to our life.

The spin Hall effect enables us to manipulate the degree of freedom of spins of the electron in heavy metals. A pure spin current to a transverse direction is generated via the spin Hall effect by applying a charge current to a longitudinal direction and vise versa. The pure spin current can be probed with a neighboring ferromagnetic metal, namely ferromagnetic (FM)/ heavy metal (HM) bilayer films characterize the pure spin current.

Spin torque ferromagnetic resonance (ST-FMR) occurs in FM/HM bilayer films and is one of the candidates to characterize a pure spin current and evaluate spin Hall angle of heavy metals. The spin Hall angle is the conversion efficiency from a charge to spin current and is denoted as $\eta = J_c/J_s$, where $J_c$ and $J_s$ are charge current and generated pure spin current, respectively. In ST-FMR, the spin Hall angle can be evaluated by analyzing spectrum intensity of a symmetric and an asymmetric component, so-called spectrum intensity ratio (SIR) method. The spin Hall angle can be also evaluated by the effective damping modulation (EDM) in which the observed half width at half maximum is modulated by direct currents flowing in a heavy metal, and consequently the modulation give the spin Hall angle.

In our previous report demonstrated by S. Kasai et al., it was clarified that the EDM is the better method than SIR to evaluate the spin Hall angle with respect to the ferromagnetic larger thickness in ST-FMR measurements because a spin Hall angle should be a constant value at any condition. Namely, EDM show the constant spin Hall angle on FM thickness while SIR show linear thickness dependence of spin Hall angle, indicating the necessity of direct currents to evaluate spin Hall angles. However, systematic and comparative studies on SIR and EDM methods are still insufficient, while these methods are expected to be advantageous compared to other methods. The characterization of spin Hall angles and relevant materials development are of particular importance for the device applications such as next-generation magnetic random access memories.

In this study, Py/Pt bilayer films are prepared by an rf magnetron sputtering. ST-FMR measurement, particularly in the external magnetic field angle dependence, is systematically performed by using a lock-in amplifier and dc source. The spin Hall angle of Pt is evaluated by using aforementioned two methods. It is found in this study that the evaluated spin Hall angle by using a spectrum intensity ratio method shows an anomalous modulation caused by direct current, which cannot be described by a conventional framework, while that by using an effective damping modulation method show a constant and reliable value. The further investigation provides that the modulation in the spin Hall angle obtained by a spectrum intensity ratio method is linearly changed by the magnitude of a direct current. The linear modulation can be attributed to the linear modulation of an intensity of a symmetric component in ST-FMR spectra under a direct current. Finally, we could suggest that the modulation of a symmetric component is characterized by photoresistance-like effect.

# 1 Introduction

## 1.1 Overview

Spintronics is regarded as the combined research field of the electronics and magnetics because the emerging field requires us to manipulate and utilize the degree of freedom of the charge and spin of electron.

The history of Spintronics is considered to start when the giant magnetoresisntece (GMR) was individually discovered in 1987 by Albert Fert and Peter Grünberg who were awarded the Novel price in 2007 [1, 2]. The first device of GMR was a multi-layer of Fe/Cr which is called the current in-plane GMR (CIP-GMR).

In a CIP-GMR device, the charge currents flow to the in-plane direction under the external magnetic field swept and a relative configuration of magnetizations is changed to parallel and anti-parallel configurations. A magnetoresistance (MR) of CIP-GMR is determined by the spin dependent interface scattering [3]. While CIP-GMR sensor has been developed and contributed to realize a high capacity Hard Disc Drive (HDD), next type of magnetoresistance device was required [4]. The current perpendicular to plane GMR (CPP-GMR) was the next-generation GMR device whose MR is determined by spin dependent interface and bulk scatterings so that CPP-GMR generally show the higher MR than that of CIP-GMR. Moreover, CPP-GMR can be described well by the Varet-Fert equation based on the spin-diffusion model [5].

The Tunneling magnetoresisnace (TMR) is also an important phenomenon in which an insulator is sandwiched by two ferromagnetic materials. While, in the Jullière model, the TMR is determined by the spin polarizations of ferromagnetic layers [6], a recent progress with a single crystal MgO based magnetic tunneling junction (MTJ) insulator opens up the advanced research field in not only application and but also fundamental point of view [7, 8].

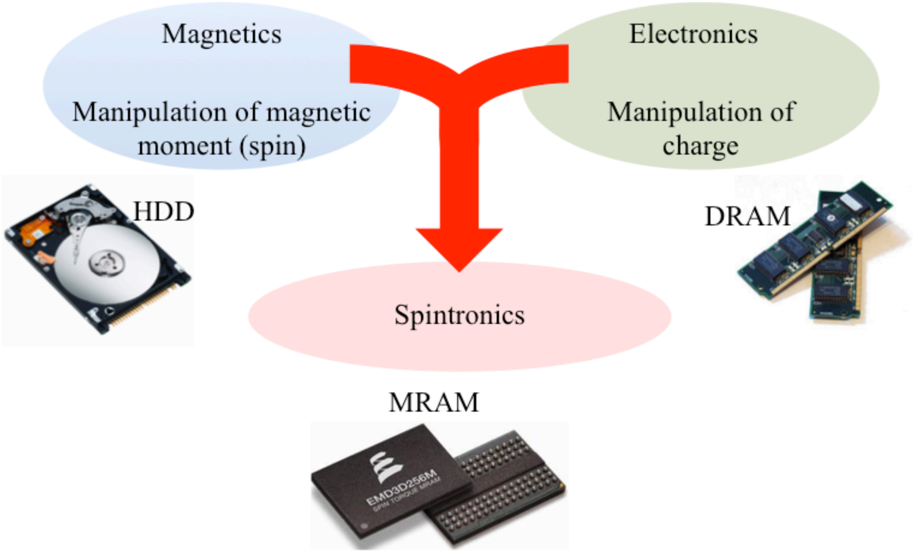

Figure 1.1 overview of spintronics including the magnetics and electronics.

In both of CPP-GMR and MTJ devices, the spin polarization of ferromagnetic materials is quite important because spin polarization means how many spins of electron are allied to the same direction as the magnetization of ferromagnetic material and MR is proportional to a spin polarization. In addition, a spin polarization determines a spin-polarized current which contains the flows of charges and aligned spins to the direction of the magnetization. The flow of the aligned spins corresponds to the flow of spin angular momenta called spin transfer torques. Thus, a spin-polarized current can be thought as one of the ways to manipulate a spin angular momentum and also to manipulate a magnetization of a ferromagnetic layer [9, 10].

The spin Hall effect is also the way to manipulate spin angular momentum, as will be discussed later in detail in section 2.2, because the spin Hall effect enables to generate a pure spin current which is the flow of spin torques without a net charge current when a charge current is applied in a heavy metal. The spin Hall effect occurs in a heavy metal which has a spin orbit interaction and realizes a spin accumulation at the edge of the sample [11, 12]. The Spin Hall effect was theoretically predicted by Russian physicists Mikhail I. Dyakonov and Vladimir I. Perel in 1971 and experimentally observed by K. Kato in 2004 [13,14]. The spin Hall effect can be distinguished into an intrinsic and extrinsic effect. Besides the extrinsic spin Hall effect is distinguished into the skew scattering and side jump [15,16,17]. The intrinsic spin Hall effect is influenced by the band structure of metal while the extrinsic spin Hall effect is influenced by scattering events. The skew scattering is influenced by not only the scattering event but also diffusion after the scattering, which cause the spin dependent deflection. On the other hand, the side-jump effect influences to a spin dependent displacement in a scattering event.

A lot of the first principles calculations have been performed to understand how much each transition metal possesses intrinsic spin Hall conductivity. Especially platinum (Pt) used in this study is well known as one of the heavy metal possessing high spin Hall conductivity. G. Y. Guo et. al., in 2008 have studied the first principles calculation in respect of the intrinsic spin Hall conductivity of Pt [18]. Furthermore, T. Tanaka et.al., in 2008 have demonstrated the intrinsic spin Hall conductivity of 4d and 5d transition metals and They could have demonstrated the magnitude and sign of the spin Hall conductivity [19]. Nowadays, following the paper, Pt, Tantalum and Tungsten have been widely used as a material to produce the spin Hall effect because these materials possess a large spin Hall conductivity. In regard to an extrinsic spin Hall effect, not only aforementioned materials but also alloys have been experimentally examined. Especially, Niimi et. al., have demonstrated a large extrinsic spin Hall effect of CuBi alloys in 2012 and Yamanouchi et. al., have studied that of CuIr in 2013 [20, 21].

Why manipulation of spin angular momentum is important in spintronics? Because manipulation of a spin angular momentum enable to achieve phenomena such as an oscillation and a magnetization switching in which a damping parameter of ferromagnetic layer is compensated or overcome by spin transfer torques [22, 23, 24, 25, 26, 27, 28, 29, 30, 31]. In the CPP-GMR and MTJ, a spin-polarized current generated in a ferromagnetic layer works to make magnetization in another ferromagnetic layer oscillated and/or switched [32, 33]. Thanks to the much improvement on micro-fabrication techniques, recently microwave generator and detector with spintronics devices could have been realized. Microwave generator and detector are generally considered to be in the field of quartz. However, the scalability with semiconductor is limited and it is difficult to achieve a device with a less than 1 μm in size for an application while a CPP-GMR and MTJ enables us to fabricate the microwave generator and detector with a less than sub-micron in size. Moreover, the MTJ based microwave generator made by AIST in japan could have overcome the output power of conventional application devices in 2016 [34]. The achievement probably enables us to replace the application device of microwave generator made of quartz.

The spin Hall effect is also a candidate to inject a spin transfer torque into a ferromagnetic layer and the spin Hall effect can be utilized in a study of the ferromagnetic dynamics because a ferromagnetic material can absorb a pure spin current generated due to spin Hall effect and show the ferromagnetic resonance (FMR) when ferromagnetic metal is placed adjacent to heavy metal. L. Liu et. al., firstly demonstrated the FMR with a spin transfer torque induced by the spin Hall effect called spin transfer torque induced FMR (ST-FMR) in 2011 in Permalloy (NiFe alloy)/ Pt bilayer films by using a radio frequency (RF) current and a constant external magnetic field [35]. The output voltage of a ST-FMR spectrum is detected by the rectification effect via anisotropy magnetoresistance

(AMR) to be discussed later in chapter 1.7. The FMR spectra enable to evaluate spin Hall angle $\eta$ which is the efficiency of the conversion form a charge to a spin current. Furthermore, an additional direct current (DC) bias modulates the half width at the half maximum of the FMR spectra which is firstly demonstrated by K. Ando et. al., in 2008 by using cavity FMR set-up [36].

In analogy with a microwave generator in CPP-GMR and MTJ devices, the microwave generator with the spin Hall effect can be realized by compensating a damping parameter with spin transfer torques [23, 24, 25]. Although the output power of the ST-FMR device is expected to be quite small compared to that of MTJ because ST-FMR detection is performed via AMR, a microwave generator can work in large area because spin transfer torques can be injected perpendicular to a ferromagnetic layer from heavy metal. The spin-Hall-effect-induced-auto-oscillator in an extended film was already achieved in low temperature in 2014 [26]. However, more developments and understandings are required to realize a spin Hall based microwave generator performing at room temperature.

## 1.2 Spin Hall Effect

The explanation of the spin Hall effect generally starts from the conventional Hall effect. In the conventional Hall effect, the effect occurs in any conductor and the transverse voltage is generated with the external magnetic field applied normal to film and longitudinal charge current applied due to the Lorentz force. Subsequently, the anomalous Hall effect is described because a spin dependent scattering induces the transverse voltage with the same manner of the spin Hall effect. The effect occurs in ferromagnetic conductor because the effect is characterized by orthogonal relations of a magnetization of the ferromagnetic conductor and applied charge current. As a result of the relations, the transverse voltage is generated due to spin orbit scattering in the ferromagnetic conductor.

The spin Hall effect is one of the option to generate a pure spin current and a phenomenon which converts a charge to spin current in a heavy metal having relatively large spin orbit interaction [11-21]. The origins of SHE are divided into three parts: intrinsic, skew scattering and side jump effect. Skew scattering and side jump effect are classified as extrinsic effects. From now, I will introduce the intrinsic SHE because the origin of SHR in the platinum used in this study is know as the intrinsic SHE.

An intrinsic SHE is characterized by a band structure including a spin orbit interaction. In normal metal, spin orbit interaction at the Fermi level is written as ***l•s***, which is characterize spin Hall conductivity, $\sigma_{xy}^{S} \sim \frac{e}{a}\frac{<l \bullet s>}{\hbar^2}$. According to the Hund's third rule, the spin Hall conductivity is expected to be negative in less than half filling of the d-bands and positive in more than half filling of the d-bands, which was proposed by T. Tanaka et al., in 2008 shown in Fig 2.3.1. Pt, which is used in this study, is theoretically demonstrated as a material having a high intrinsic spin Hall conductivity [19].

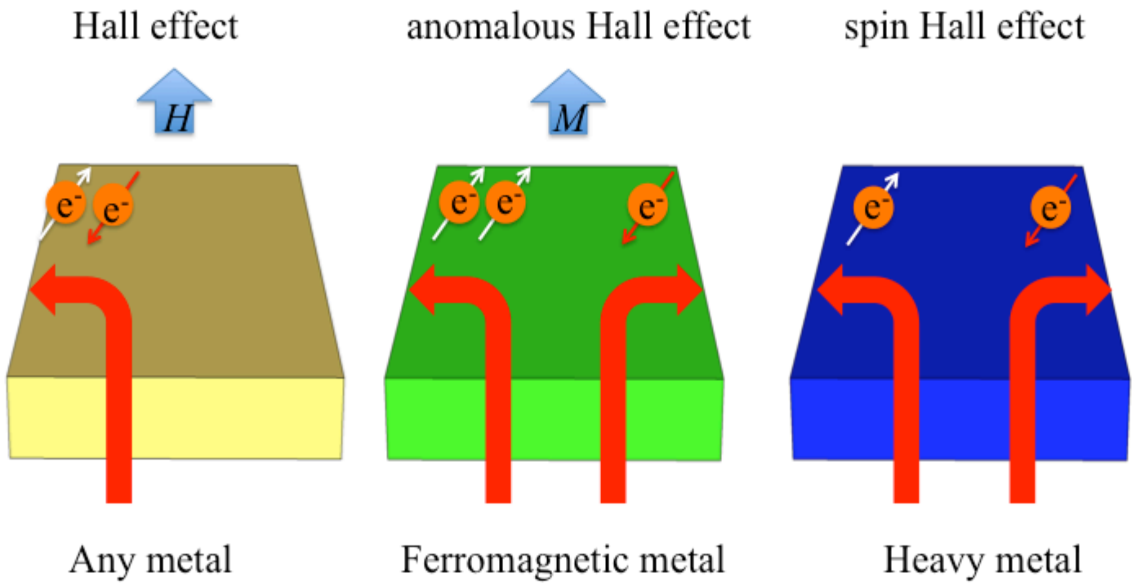

1.2.1 the comparison of the Hall effect, anomalous Hall effect and spin Hall effect.

### 1.3 Spin Polarized Current And Pure Spin Current

Ferromagnetic materials work as a spin polarizer because of its spin polarization P characterized by band structure and generate a spin-polarized current especially at the Fermi level for a transport property. Figure 1.3.1 shows the density of state (DOS) of a ferromagnetic and normal metal. In a ferromagnetic metal, the DOS at the Fermi level of up and down spin are not the same value, namely the DOS of the up-spin is larger than that of the down-spin, which characterizes spin polarized currents in a ferromagnetic metal. On the other hand, in normal metal the DOS of the up and down spin is compensated, which indicates that conduction currents are totally polarized. The spin polarization P for conduction electrons is defined as $P = \frac{DOS(\text{up-spin}) - DOS\,(\text{down-spin})}{DOS(\text{up-spin}) + DOS\,(\text{down-spin})}$, and most ferromagnetic metals show the spin polarization with less than 1 (e.g. Ni=0.35, Fe= 0.45) while the half metals such as several Heuslar alloys theoretically show P=1 [28, 29].

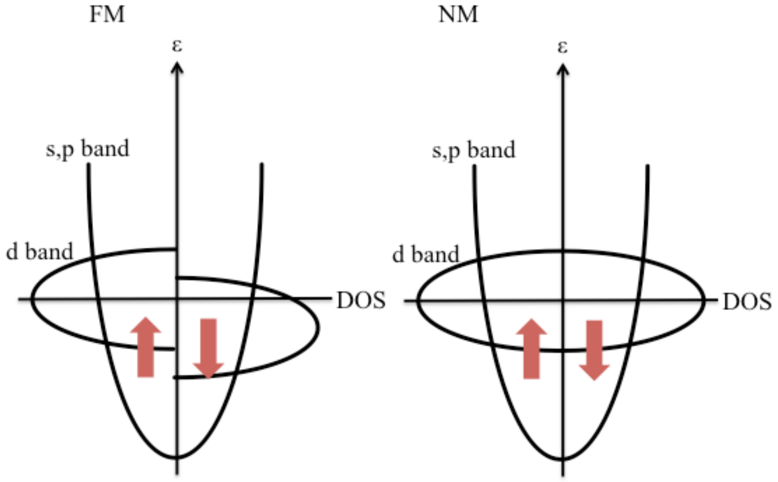

Figure 1.3.1 the density of state of ferromagnetic metal and non magnetic metal.

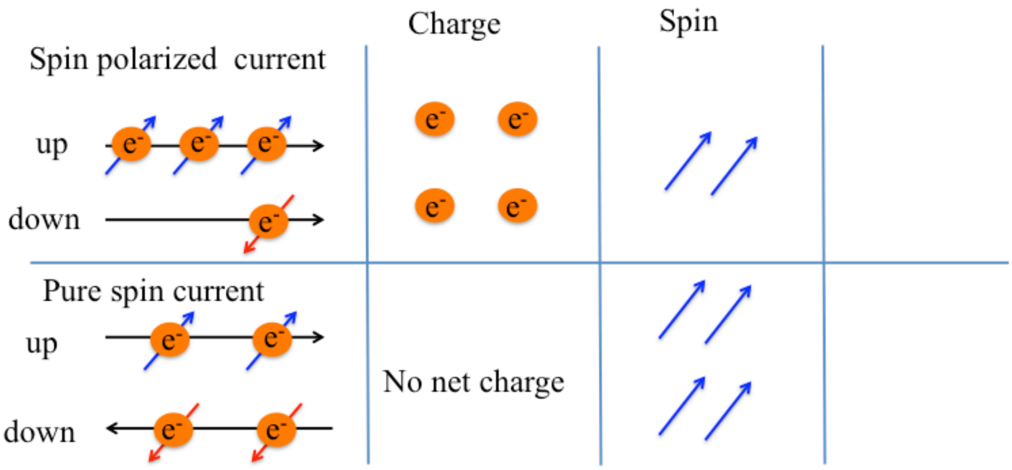

Figure 1.3.2 comparison of spin polarized current and pure spin current.

When external magnetic field is applied and electron passes in a ferromagnetic material with the thickness larger than the spin diffusion length that is the characteristic length to make spin fully aligned to the direction of the magnetization, the spins of conduction electron are polarized to the direction of the external magnetic field. Namely, Spin polarized current has the degree of freedom of charge and spin of the electron shown in the figure 1.3.2 [37, 38, 39].

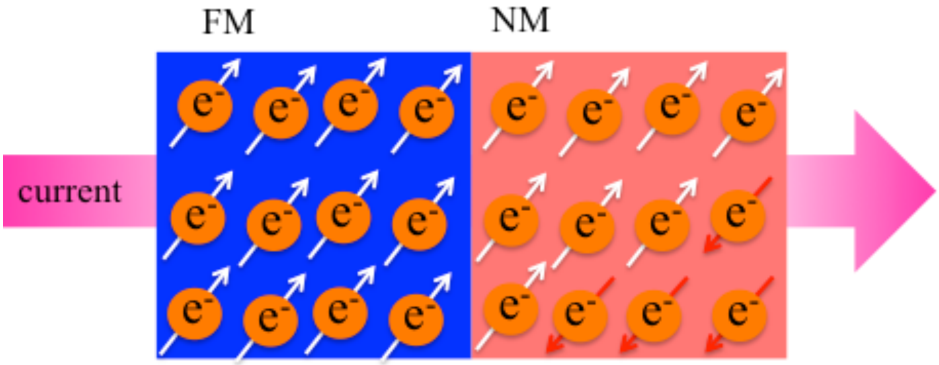

Figure 1.3.3 spin polarized current injecting a normal metal from a ferromagnetic metal

Figure 1.3.3 shows the schematic illustration on the transport of electrons flowing a ferromagnetic metal and a normal metal. When spin polarized currents are injected into the normal metal, the degree of freedom of a charge is conserved while the degree of freedom of a spin is not conserved because the numbers of up-spins and down-spins are originally same in normal metals, indicating that spins can be injected into a normal metal from ferromagnetic metal although the degree of freedom of spins are gradually dissipated according to the spin diffusion length λ of the normal metal. Figure 1.3.4 shows the schematic illustration of the chemical potentials of up-spins and down-spins in a ferromagnetic half metal and normal metal. A half metal possesses only the up-spins so that the chemical potential of up-spin in the half metal is constant. On the other hand, again, the numbers of up-spins and down-spins are originally same in normal metals so that the numbers of up-spins and down-spins are finally compensated with that of down-spins. The chemical potential of up-spins are characterized by the decay length, so-called spin diffusion length λ, and it is exponentially decreased with exp(λ/d). Here, d is the length from the interface of ferromagnetic metal and normal metal.

Therefore, spin polarized current is an option to convey the information of spins within a certain length.

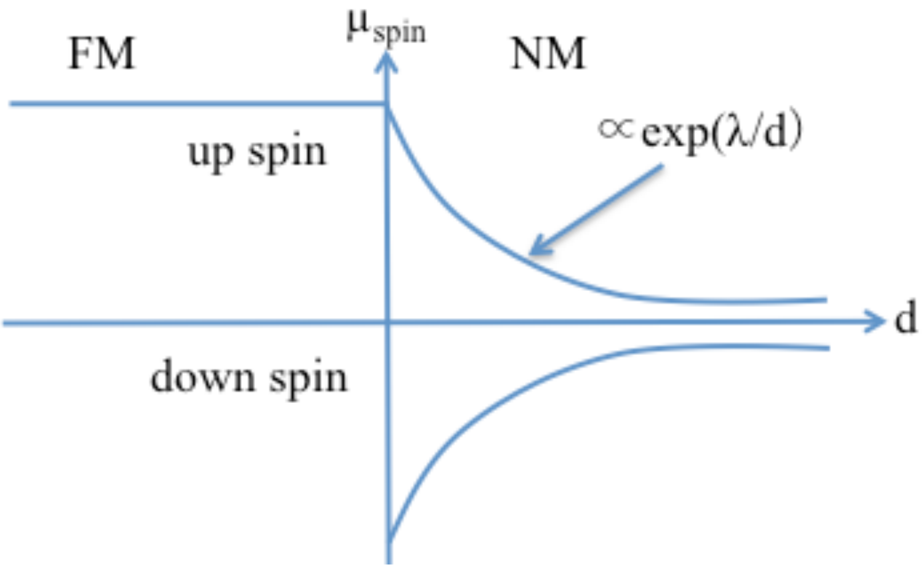

Figure 1.3.4 the chemical potential for up-spins and down-spins in ferromagnetic half metal and normal metal.

Another option is pure spin current. The pure spin current is only the flow of spins shown in figure 1.3.2 and figure 1.3.5, and it can be generated in normal metal because the numbers of up-spins and down-spins are originally same and compensated. Namely the directions of the flow of electrons with up-spins and down-spins are an opposite direction.

Pure spin current can be generated due to diffusions of spins in non-local configuration. Spin Hall effect described in a section 1.2 generates pure spin currents to the transverse direction when charge currents to the longitudinal direction are applied. In non-local spin valves consisting two ferromagnetic wires bridged by a wire of a normal metal shown in figure 1.3.6, pure spin currents can exist in the non-magnetic wire because of spin diffusion form the left junction to the right junction. This configuration allows us to evaluate spin Hall angles which is introduced in section 1.2 [12,20].

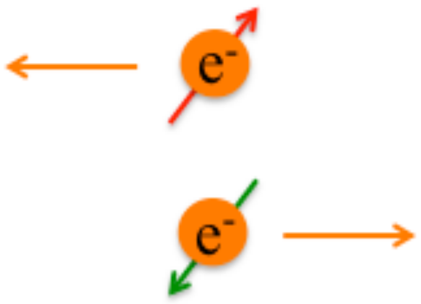

Figure 1.3.5 schematic illustration for pure spin currents

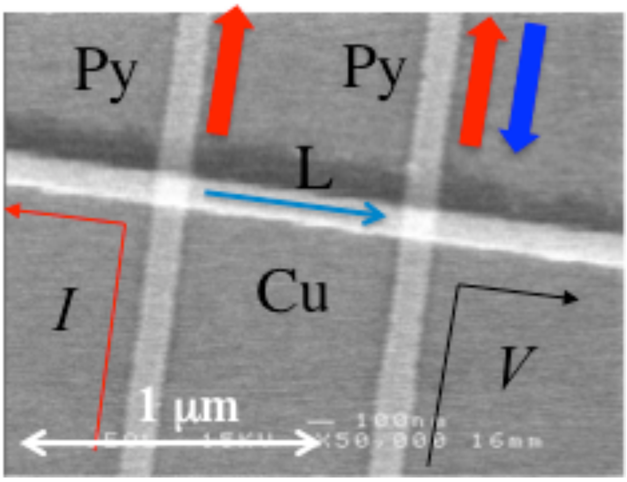

Figure 1.3.6 SEM image for a lateral spin valve

## 1.4 Ferromagnetic Resonance

Ferromagnetic resonance occurs when a magnetic moment is placed in an external magnetic field due to the precession of the magnetic moment [40, 41]. The torque induced by an external field exerts to the magnetic moment and a precession of the magnetic moment starts. The frequency of the resonance is characterized by the gyromagnetic ration and effective magnetic field and evaluated by the Kittle formula [42]. The magnetic motion, namely magnetic dynamics, can be described by the Landau–Lifshitz–Gilbert equation (LLG eg.) [43]. Here, I would like to introduce and derive both of Kittle furmula and LLG eq., respectively.

When the magnetic moment $M$ is placed in the external magnetic field $H$, $M$ feels the torque $\tau$, which can be described as

$$\boldsymbol{\tau} = \boldsymbol{M} \times \boldsymbol{H}. \qquad (1.2.1).$$

On the other hand, $\boldsymbol{M}$ is defined by an angular momentum $\boldsymbol{L}$ with the gyromagnetic ratio $\gamma$ as

$$\boldsymbol{M} = -\gamma \boldsymbol{L}. \qquad (1.2.2)$$

Therefore, the equation of the motion in respect to $\boldsymbol{M}$ can be written as

$$\frac{\mathrm{d}\boldsymbol{M}}{\mathrm{d}t} = -\gamma \frac{\mathrm{d}\boldsymbol{L}}{\mathrm{d}t} = -\gamma \boldsymbol{\tau} = -\gamma \boldsymbol{M} \times \boldsymbol{H}. \qquad (1.2.3)$$

The eqation (1.2.3) describes the Larmor precession. While the Larmor precession can explain the rotation of the magnetic moment, only the term of the Larmor precession can not describe the actual phenomenon because magnetic moment is finally aligned with the direction of the external magnetic field. Therefore, it is required to introduce the phenomenological damping term $\alpha \boldsymbol{M} \times \frac{\mathrm{d}\boldsymbol{M}}{\mathrm{d}t}$ to equation (1.2.3) as follows:

$$\frac{\mathrm{d}\boldsymbol{M}}{\mathrm{d}t} = -\gamma \boldsymbol{M} \times \boldsymbol{H} + \alpha \boldsymbol{M} \times \frac{\mathrm{d}\boldsymbol{M}}{\mathrm{d}t}, \qquad (1.2.4)$$

$\alpha$ is the damping parameter. The equation (1.2.4) is called LLG equation.

From the LLG equation, it is possible to derive the Kittle formula. I would like to introduce the Kittle formula before introducing LLGS equation which is employed to demonstrate the phenomena in the practical spintronics devices. I would like to assume a uniaxial anisotropy and replace $\boldsymbol{M}$ and $\boldsymbol{H}$ with $\boldsymbol{M}_{\mathrm{eff}}$ and $\boldsymbol{H}_{\mathrm{eff}}$, respectively. $\boldsymbol{H}_{\mathrm{eff}}$ is denied as

$$\boldsymbol{H}_{\mathrm{eff}} = \boldsymbol{H}_{\mathrm{zeeman}} + \boldsymbol{H}_{\mathrm{ex}} + \boldsymbol{H}_{\mathrm{sta}} + \boldsymbol{H}_{\mathrm{ani}}, \qquad (1.2.5)$$

where $\boldsymbol{H}_{\mathrm{zeeman}}$, $\boldsymbol{H}_{\mathrm{ex}}$, $\boldsymbol{H}_{\mathrm{sta}}$ and $\boldsymbol{H}_{\mathrm{ani}}$ mean the field induced by the Zeeman energy, exchange interaction, magnetostatic energy and anisotropic energy, respectively. (Although the context of $\boldsymbol{H}_{\mathrm{eff}}$ is not required to derive the Kittel equation, it is needed later.)

An ideal uniaxial anisotropy can be realized in an infinite two-dimensional ferromagnetic plate. The observed anisotropy exists in the perpendicular direction to the plane. In addition, an in-plane anisotropy field can be observed if the width of the plate is so narrow that we regard the plate as a one-dimensional wire. When the external magnetic field is applied to the z direction, the magnetic dynamics in x and y direction can be written as follows:

$$\frac{\mathrm{d}M_{\mathrm{x}}}{\mathrm{dt}} = \gamma\left(M_{\mathrm{y}}H_{\mathrm{z}} - M_{\mathrm{z}}H_{\mathrm{y}}\right), \frac{\mathrm{d}M_{\mathrm{y}}}{\mathrm{dt}} = \gamma(M_{\mathrm{z}}H_{\mathrm{x}} - M_{\mathrm{x}}H_{\mathrm{z}}). \qquad (1.2.6)$$

An effective field including a demagnetizing field in each direction can be written as follows:

$$H_{\mathrm{x}} = H_{\mathrm{x}}^{0} - \mu_0 N_{\mathrm{x}} M_{\mathrm{x}}, H_{\mathrm{y}} = H_{\mathrm{y}}^{0} - \mu_0 N_{\mathrm{y}} M_{\mathrm{y}}, H_{\mathrm{z}} = H_{\mathrm{z}}^{0} - \mu_0 N_{\mathrm{z}} M_{\mathrm{z}}, \qquad (1.2.7)$$

where N is a demagnetization field coefficient and $\mu_0$ is a magnetic permeability in vacuum. Within a first approximation of the dynamics it is possible to consider $M_{\mathrm{z}} = M, \frac{\mathrm{d}M_{\mathrm{z}}}{\mathrm{dt}} = 0$. Because the magnetization dynamics has time dependence of exp(-i$wt$), eq. (1.2.6) is solved though the obtained 2×2 matrix

$$\begin{vmatrix} iw & \gamma(B_0 + (N_y - N_z)\mu_0 M \\ -\gamma(B_0 + (N_x - N_z)\mu_0 M & iw \end{vmatrix} = 0 \qquad (1.2.8)$$

$$\omega_0 = \mu_0 \gamma\{[H_0 + \left(N_y - N_z\right)M][(H_0 + (N_x - N_z)M]\}^{1/2} \qquad (1.2.9)$$

Eq. (1.2.9) is called the Kittle formula. I would like to define an in-plane anisotropy field $H_\mathrm{c}$, an out-of-plane anisotropy field $H_\mathrm{d}$ and the observed effective magnetic field $H_\mathrm{eff}$ as follows in this study, $H_c = N_y\mu_0 M, H_d = N_z\mu_0 M, H_\mathrm{eff} = N_x\mu_0 M$, respectively.

Resonant frequencies of FMR in the uniform mode can fit in the Kittle formula.

Landau–Lifshitz–Gilbert-Slonczewski equation (LLGS.eq) is an advanced equation of the LLG eq. and describes FMR with the spin transfer torque and field like torque [9]. The schematic illustration is shown in Figure 1.4.1 and the equation is written as follows:

$$\frac{\mathrm{d}\boldsymbol{M}}{\mathrm{d}t} = -\gamma\boldsymbol{M}\times\boldsymbol{H}_\mathrm{eff} + \alpha\boldsymbol{M}\times\frac{\mathrm{d}\boldsymbol{M}}{\mathrm{d}t} + \tau_\perp\boldsymbol{M}\times(\boldsymbol{\sigma}\times\boldsymbol{M}) + \tau_\parallel(\boldsymbol{\sigma}\times\boldsymbol{M}).$$

Here, $\boldsymbol{\sigma}$ is the spin torque. The third and forth term describes the spin transfer torque and field like torque, respectively. Spin transfer torque is also known as anti-damping torque because the direction is opposite to the direction of the damping torque. If the damping torque is compensated or overcome by the spin transfer torque, an oscillator or magnetization switching can be achieved [27, 28, 29, 30].

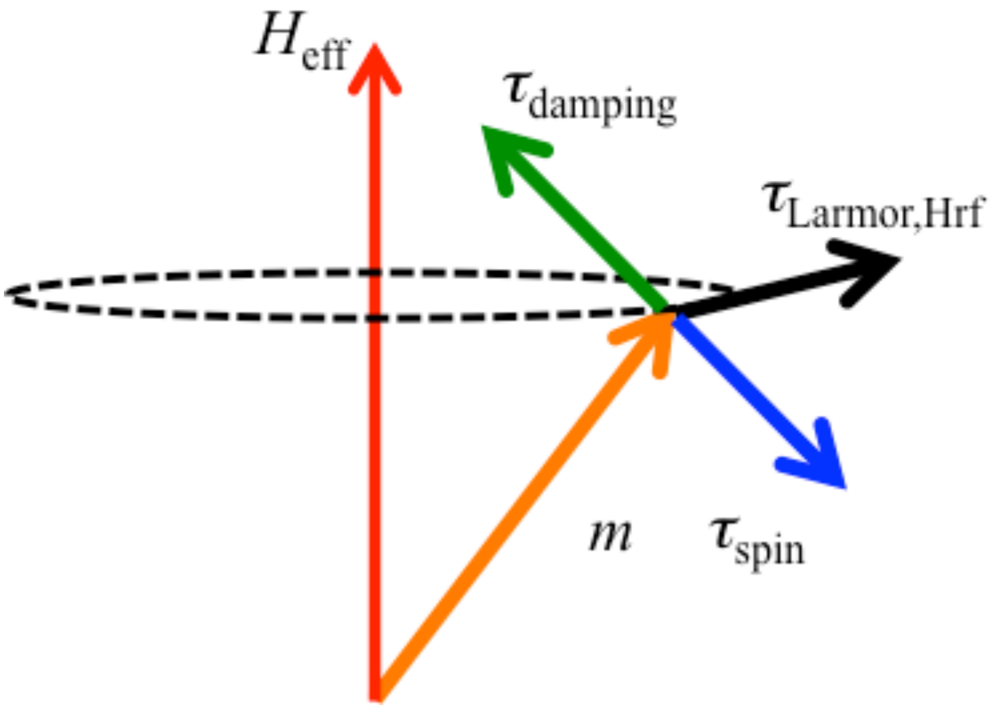

Figure 1.4.1 Schematic illustration for magnetization precession with torques based on LLGS equation.

### 1.5 Interface Perpendicular Magnetic Anisotropy

Interface perpendicular magnetic anisotropy (PMA) occurs at an interface such (e.g. ferromagnetic metal/insulator and ferromagnetic metal/heavy metal) due to the symmetric breaking, and the interface PAM is attracting issue in spintronics to develop MRAM device.

At the interface of FM/Insulator, quite large interface PMAs has been observed so far. CoFeB/MgO and Fe(001)/MgO are famous systems. The origin of the interface PMA of FM/Insulator is the hybridization of $3d_z^2$ orbit of Fe and $2P_z$ orbit of O in MgO, which gives rise to the interface PMA $K_\mathrm{i}$ of 2 mJ/m$^2$ [44, 45, 46]. The large interface PAM is consistent with theoretical prediction.

On the other hand, at the interface of FM/HM, smaller interface PMAs have been observed compared to FM/insulator interfaces. The origin of the interface PMA of FM/HM films is the hybridizations of the 3d orbit of FM and the 4d or 5d orbit of HM. Especially, Fe/Pt and Co/Pt has a typical interface showing interface PMA [47, 48].

The interface PMA is included in $H_\mathrm{ani}$ in the effective magnetic field $H_\mathrm{eff}$ obtained by FMR measurements, and the enhancement of the interface PMA in the in-plane magnetized films reduces the value of saturation field $H_\mathrm{k}$, which suggesting that the magnetic anisotropy energy $E_\mathrm{u} = \frac{M_S H_k}{2}$ can be reduced by enhancing interface PMA in the in-plane magnetized films. Finally, the reduction of the magnetic anisotropic energy in the in-plane magnetized films facilitates the magnetization auto oscillation and magnetization switching (see section 1.5 and 1.9) because, for example, the critical current for magnetization switching is proportional to $H_c + 2\pi H_\mathrm{eff}$. Here, Hc is the coercive field. Therefore, the enhancement of interface PMA can pave the way for spintronics device application with in-plane magnetized films.

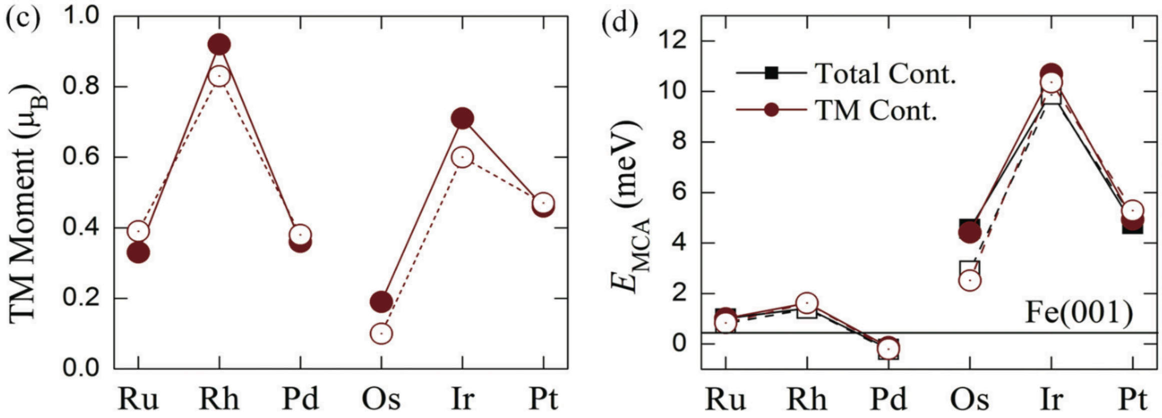

Figure1.5.1 First-principles calculations for interface PMA on 5d materials [48]. Reprinted figures with permission from D. Odkhuu et at., Physical Review B **88**, 184405 (2013). Copyright 2018 by the American Physical Society.

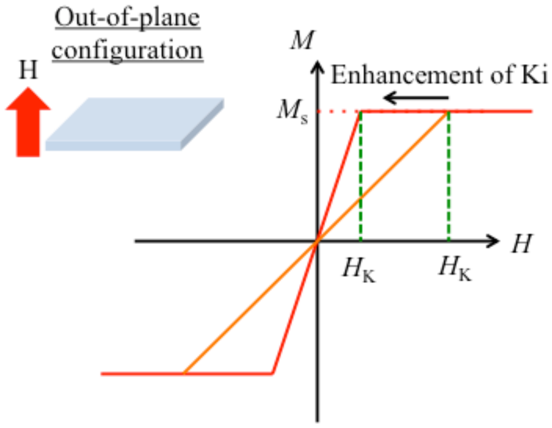

Figure1.5.2 Schematic illustration of the hysteresis loops with interface PMAs.

### 1.6 Effective Damping Modulation

The effective damping modulation describes that the HWHM and the related damping parameter of the FMR. The effective damping modulation occurs when direct currents flow in a neighboring heavy metal of a ferromagnetic metal in which the FMR is excited. The direct currents induce the injection of pure spin current into ferromagnetic metal; namely, spin torques, also called anti-damping torques, are injected into a ferromagnetic metal due direct currents in a heavy metal.

The effect was firstly demonstrated by K. Ando et al., in 2008 and the demonstration has contributed to realization of a magnetization switching and auto oscillation via the spin Hall effect [36]. It is known that the damping parameter of Py/Pt is higher than that of Py single layer due to the inverse spin Hall effect caused by high spin-orbit interactions in Pt. when the dc currents is applied to the Pt layer, spin currents appears due to spin Hall effect, and the spin current propagates into Py layers. The spin polarization of the spin current $\boldsymbol{\sigma}$ is $\boldsymbol{J}_c \times \boldsymbol{n}$, where $\boldsymbol{J}_c$ is the charge current in Pt and $\boldsymbol{n}$ is the direction normal to the film.

Figure 1.6.1 is the FMR spectra with dc current [36]. The direct currents dependence of FMR spectra shows at $\theta$=90˚ shows the modulation on the half width at half maximum and spectrum intensity. On the other hand, at $\theta$=0˚, these modulations are hardly shown. Here, $\theta$ is a relative angle of current direction and magnetization. The results demonstrated that the injected spin torque characterized by dc currents works as the anti-damping torque and modulate the half width at half maximum and the related damping parameter. The modulation factor of the damping parameter is written as $\Delta\alpha = (\frac{\hbar\gamma\eta_{SHE}}{2\pi f e M_s V})J_C$, where $\hbar, \gamma, \eta_{SHE}, f$ and $V$are the Dirac constant, the gyromagnetic ratio, the spin Hall angle and the frequency of the magnetic field, and the volume of ferromagnetic layer, respectively, and the expression suggests that the modulation factor is proportional to a current density flowing in Pt and the spin Hall angle can be evaluated from the modulation factor. In this study, spin Hall angle is evaluated with Py/Pt bilayer films by using the damping modulation. The detailed will be described in the section 1.8.

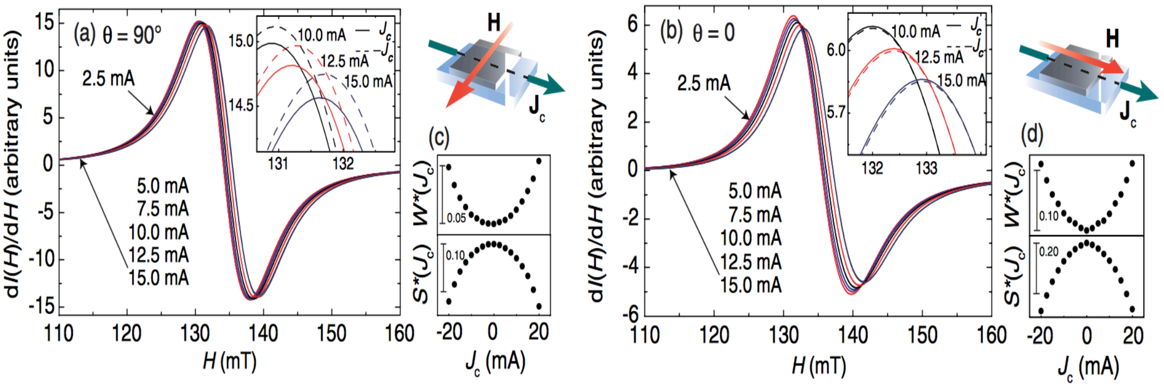

Figure 1.6.1 the experimental data on FMR spectra with the damping modulation [36] Reprinted figures with permission from K. Ando et at., Physical Review Letters **101**, 036601 (2008). Copyright 2018 by the American Physical Society.

### 1.7 Anisotropy Magnetoresistance

Figure 1.7.1 shows the schematic illustration for the anisotropy magnetoresistance (AMR) [49]. The AMR occurs when electrons and a magnetic field are applied to a ferromagnetic material. The magnetoresistance has relative angle dependence between the direction of a charge current and a magnetic field (magnetization direction). Namely, in the case of a perpendicular configuration of a magnetization and a current AMR gives a smallest resistance while AMR gives a highest resistance in the case of a parallel configuration of a magnetization and a current. Although the output of AMR is several percent which is quite small compared to GMR and TMR, in this study, AMR works as the detector for dc voltage induced by FMR [35, 50, 51, 52, 53, 54, 55, 56, 57].

AMR effect is simply characterized by spin-orbit interaction, namely the interaction of conduction electron and the orbit of d-band characterize the anisotropy magnetoresistance. The spin-orbit interaction give rise to a change of various resistivity as follows,$\rho = \rho_{\perp} + \Delta\rho cos2\theta$, where $\rho_{\perp}$ is the resistivity of perpendicular configuration of magnetization, current directions and $\Delta\rho$ is the deference of the resistivity of perpendicular and parallel configurations, and $\theta$ is the relative angle of magnetization and current direction. In the case of Py, AMR is around 1%.

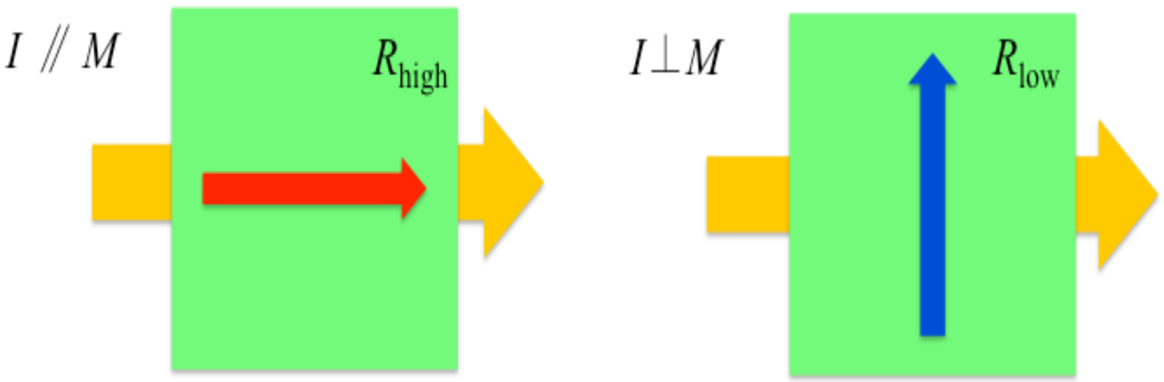

Figure1.7.1 Schematic illustration for AMR

### 1.8 Rectification Effect

The rectification effect is the detection method for a dc voltage from the applied AC voltage and the effect is employed to detect the dc output voltage from radiofrequency current (rf-current) flowing in Py in this study [58, 59, 60, 61]. The magnetization in FM precesses with the same frequency of rf-current like the schematic illustration in figure 1.8.1. Thus, magnetization m(t) can be written as follows, $m(t)=m_0\sin(wt+\varphi)$. Here $w$ is the frequency of the applied rf- current $I(t)=I_0\cos wt$ and $\varphi$ is the phase, and the corresponding resistance R(t) can be written as follows, $R(t)=R_0+\Delta R\sin(wt+\varphi)$. Here, $R_0$ is the resistance at t=0 and $\Delta R$ is the resistance change characterized by AMR shown in figure 1.8.2. Therefore, magnetization dynamics reflects the corresponding sample resistance via AMR so that the homodyne detection in FM, so-called spin torque diode effect, can be performed in this study [62, 63]. Namely, time-independent voltage $\langle V\rangle = \langle \mathrm{I}(t)\,\mathrm{R}(t)\rangle = \langle I_0\cos(\varpi t)(R_0 + \Delta R sin\varpi t + \varphi))\rangle$ shows dc output voltage. The time-independent voltage $\langle V\rangle \sim I_0\Delta R sin\varphi$ is detected in the rectification effect through AMR in FM. Here, $\Delta R$ can be considered as ${}^{dR}/_{d\theta}\,\Delta\theta$ so that $\langle V\rangle$ is finally treated as $\langle V\rangle = \frac{1}{2} I_0 \Delta R sin2\theta cos\theta cos\varphi$.

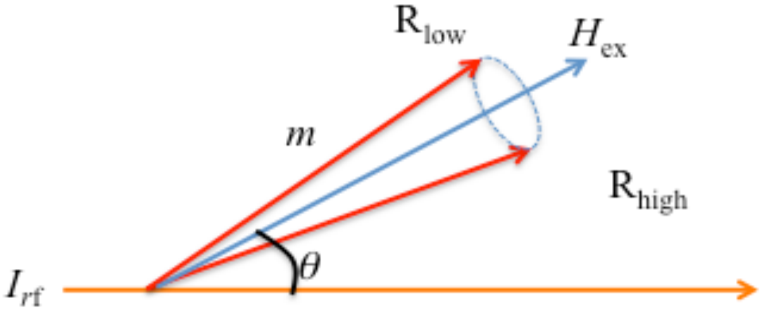

Figure 1.8.1 the schematic illustration for rectification effect with AMR

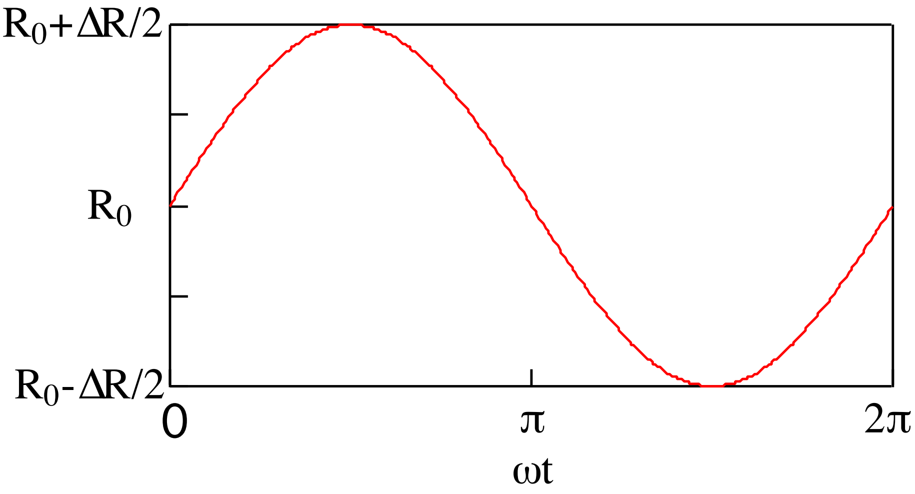

Figure 1.8.2 time dependent resistance due to AMR

### 1.9 Spin Torque FMR in The Ferromagnetic Metal/ Heavy Metal Bilayer Films

Spin torque ferromagnetic resonance (ST-FMR) is induced in the ferromagnetic/heavy metal bilayer films when rf-currents are applied into the films. Therefore, the effects mentioned in previous sections can be applied, namely the rectification via AMR and FMR in FM and spin Hall effect in HM can be introduced in the FM/NM bilayer films.

ST-FMR in FM/HM bilayer thin films is firstly demonstrated by L.Liu in 2011 and enables us to evaluate spin Hall angle $\eta = J_S/J_C$with ferromagnetic resonance [24, 25, 35, 50, 51, 52, 53, 54, 55, 56, 57, 64, 65]. When the charge current $J_c$ flow in the FM/NM bilayer films, the longitudinal charge currents flowing in NM generate transverse spin currents $J_s$ and the Oersted field. The spin current is injected and diffused into FM through the interface and the injected spin current also can be considered to be the spin torque. On the other hand, the Oersted field generated in HM and crossing FM can be the torque whose direction is the same as that of the effective magnetic field. Because of the dimensions of the device, the Oersted field can considered to be proportional to magnitude of charge currents, the ratio of these torques is consequently proportional to spin Hall angle of HM. Therefore, the current density in HM characterized spin Hall angle of HM in the device.

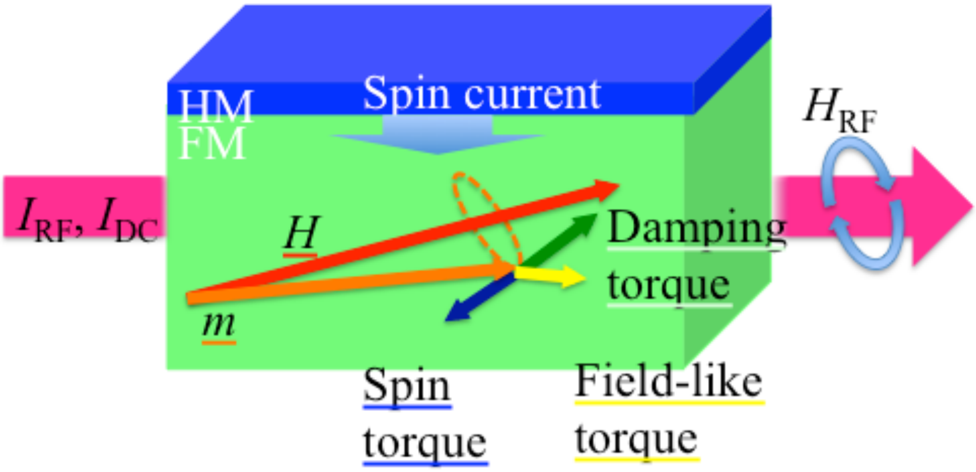

Figure 1.9.1 schematic illustration on ST-FMR in the FM/HM bilayer film

Figure 1.9.1 shows the schematic illustration of the spin transfer torque FMR in bilayer films consisting of a ferromagnetic metal and heavy metal. When rf-current and external magnetic filed are applied to the devices, rf-current flowing in the ferromagnetic metal can realizes the ferromagnetic resonance, and the rf-current flowing in the heavy metal characterizes the excitations of spin transfer torque and the Oersted field torque. The detection of dc voltage is performed by AMR (see section 1.7) and a rectification effect (see section 1.8). The intensity is determined by the relative angle of currents and an external magnetic field direction. Eventually, the output dc voltage can describe as follows,

$V = \frac{k}{\Delta}[SF_{\mathrm{S}}(H_{\mathrm{ext}}) + AF_{\mathrm{A}}(H_{\mathrm{ext}})]$.

Here, $k$ is a prefactor characterized by a sample resistance, $k = \frac{1}{4}\frac{d\Delta R_{\mathrm{AMR}}(\theta)}{d\theta}\frac{\gamma J_{\mathrm{rf}}^{\mathrm{FM}}\cos\theta}{2\pi(df/dH)_{H=H_{\mathrm{ext}}}}$ ,$F_{\mathrm{S}}(H_{\mathrm{ext}}) = \frac{\Delta^2}{[\Delta^2+(H_{\mathrm{ext}}-H_0)^2]}$ is a Lorentzian function excited at H=$H_{\mathrm{ext}}$, $F_{\mathrm{A}}(H_{\mathrm{ext}}) = F_S(H_{\mathrm{ext}})\frac{(H_{\mathrm{ext}}-H_0)}{\Delta}$ is an asymmetric Lorentzian function, $S = \frac{\hbar J_{\mathrm{rf}}^{\mathrm{FM}}}{2e\mu_0 M_{\mathrm{s}}t_{\mathrm{FM}}}$is symmetry of a spectrum, $A = \frac{J_{\mathrm{rf}}^{\mathrm{HM}}d_{\mathrm{HM}}}{2}[1 +$

$\frac{M_{\text{eff}}}{H_{\text{eff}}}]^{1/2}$ is asymmetry of a spectrum, Δ is a half width at half maximum of the spectrum, respectively. Moreover, $M_S$, $M_{\text{eff}}$, $H_{\text{eff}}$, $t_{\text{FM}}$, $d_{\text{HM}}$, is a saturation magnetization, an effective magnetization, an effective magnetic filed, a thickness of a ferromagnetic metal, and a thickness of a heavy metal, respectively. Thus, ST-FMR spectrum shown in figure 1.9.2 can be observed. A symmetric component and an asymmetric component are characterized by a spin transfer torque and the Oersted filed torque, respectively. It should be noted that the generated Oersted field due to the current flowing in FM does not influence to the magnetization dynamics because the Oersted fields are cancelled out inside the FM while the fields are active outside the FM.

According to the abave expression, the amplitude of ST-FMR has sin2θcosθ dependence shown in figure1.9.3. On the other hand, S/A, $H_0$ and Δ is independent of the relative angle θ shown in figure 1.9.3. Figure 1.9.4 shows ST-FMR spectra at t= 5 and 1.7 nm. In the case of t= 5nm, ST-FMR spectra show the assymmetric shapes, which suggests that the Oersted field is the dominant contribution as the resonant source. On the other hand, in the case of t=1.7nm, ST-FMR spectra show the symetri shapes, which suggests that the spin torque generated by spin Hall effect in Pt is the dominant contribution as the resonant source.

Additionally, the spin Hall angle $\eta = J_S/J_C$ can be obtained with this following equation, $\eta_{SIR} = t_{\text{FM}} d_{\text{HM}} \frac{S}{A} \frac{e\mu_0 M_S}{\hbar} \frac{2\pi f}{\gamma H_{\text{ext}}}$. The evaluation method is called Spectrum Intensity Ratio method (SIR), and according to the previous repots, spin Hall angle of Pt in Py/Pt bilayer films is varied from 0.01 to 0.19 [[24, 25, 35, 50, 51, 52, 53, 54, 55, 56, 57, 64, 65]. Note that The spin Hall angle described by L.Liu et al, is written to be $\eta = j_S/j_c$, where $J_{\text{rf}}^{\text{FM}}$and $J_{\text{rf}}^{\text{HM}}$ are spin current injected into FM from HM and charge current density applied into HM, respectively. Therefore, the ratio can be considered to be the efficiency of spin injection from HM into FM, which indicates that the authentic spin Hall angle is larger than the efficiency of spin injection obtained in ST-FMR measurement based on the model described by L. Liu et al.

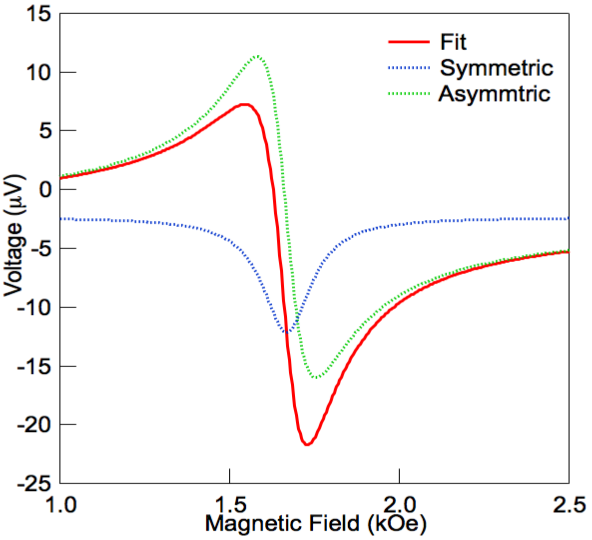

Figure 1.9.2 the typical observed spectra and the derived symmetric and asymmetric components.

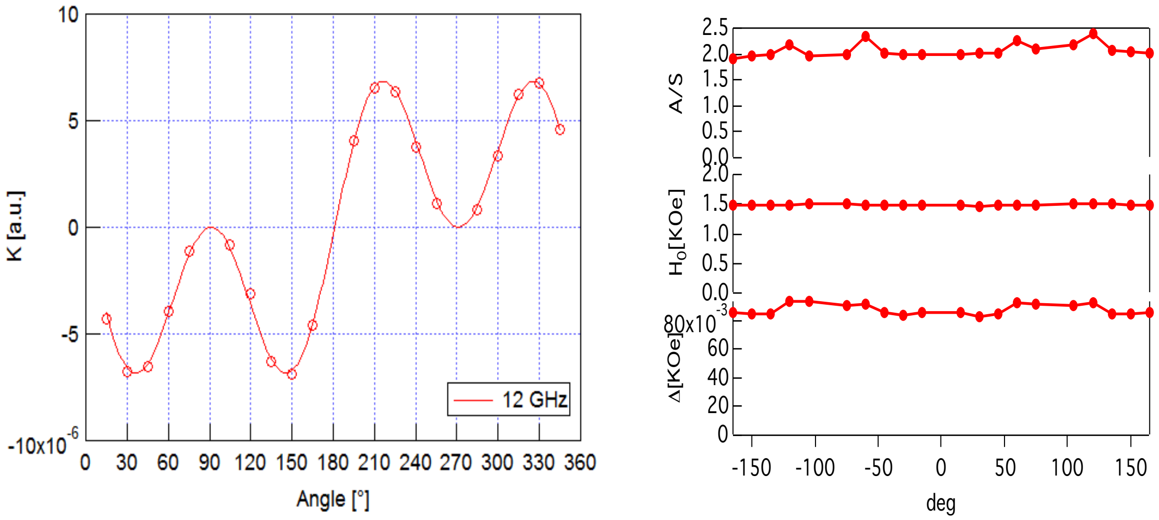

Figure 1.9.3 (Left) typical angle dependence of magnitude of ST-FMR spectrum. (Right) typical angle dependence of the ratio of symmetric and asymmetric components, the resonant field, and the half width at half maximum, respectively. (Courtesy of Kasai)

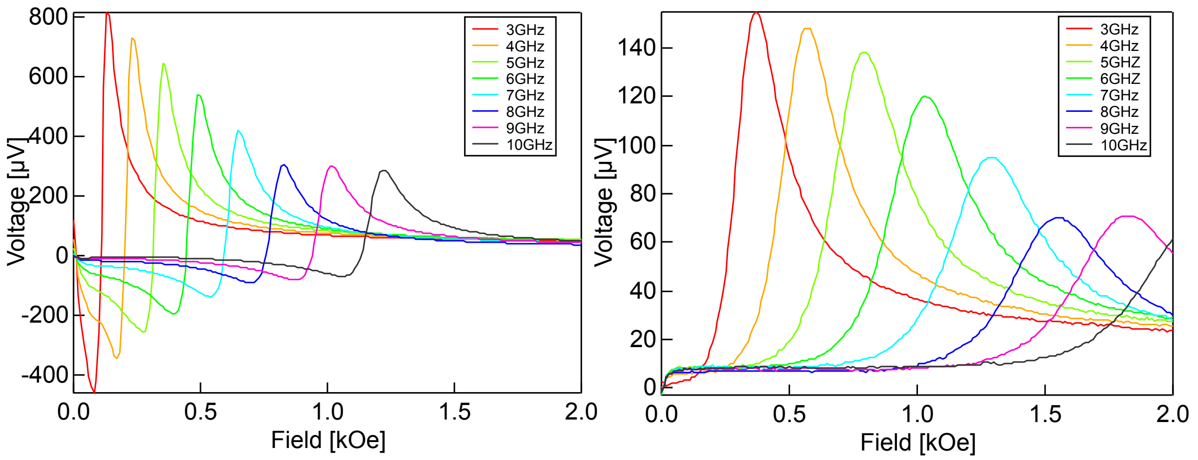

Figure 1.9.4 ST-FMR spectra at (Left) t=5nm (Right) t=1.7nm

Another evaluation method for spin Hall angle in FM/HM bilayer films is also proposed by L. Liu et al. in 2011 and called the effective damping modulation method (section 1.5) [35, 36]. Spin transfer toques characterized by DC flowing in HM change an equilibrium state of magnetization in ferromagnetic metal, and the change can modify HWHM of FMR spectra. As mentioned in section 1.5, the change of HWHM allow us to evaluate spin Hall angles which are proportional to the magnitudes of current densities flowing in HM. The HWHM Δ can be described as $\Delta = \frac{2\pi f}{\gamma}(\alpha + \Delta\alpha)$, where $f, \gamma, \alpha$ and $\Delta\alpha$ are the frequency of rf currents, the gyromagnetic ratio, the damping parameter at zero DC and damping modulation characterized by direct currents flowing in HM, respectively. The damping modulation $\Delta\alpha$ is proportional to the direct current density flowing in HM and can be described as follows, $\Delta\alpha = \frac{sin\theta}{(H_{\mathrm{ext}}+2\pi M_{\mathrm{eff}})\mu_0 M_{\mathrm{S}} t_{\mathrm{FM}}}\eta_{\mathrm{EDM}} J_{\mathrm{DC}}^{\mathrm{HM}}$ . Here, $H_{\mathrm{ext}}$ ,

$M_{\text{eff}}, \mu_0, \eta_{\text{EDM}}, and\ J_{\text{DC}}^{\text{HM}}$ are the external magnetic field, the effective magnetization, the permeability at the vacuum, the spin Hall angle evaluated by the effective damping modulation method and the density of current flowing in HM, respectively. Consequently, the evaluated spin Hall angle can be described as $\eta_{\text{EDM}} = \frac{(H_{\text{ext}}+2\pi M_{\text{eff}})\mu_0 M_S t_{\text{FM}}}{sin\theta}\frac{\Delta\alpha}{J_{\text{DC}}^{\text{HM}}}$.

By using two methods, Liu could evaluate spin Hall angle of Pt, and the evaluated spin Hall angle of SIR and EDM are 0.056 and 0.048, respectively, indicating that the evaluated spin Hall angle is varied by the methods. However, spin Hall angle is the physical constant so that it should be constant, suggesting that there exist unrevealed phenomena and/or effects in ST-FMR. To find them, there have been many studies performed.

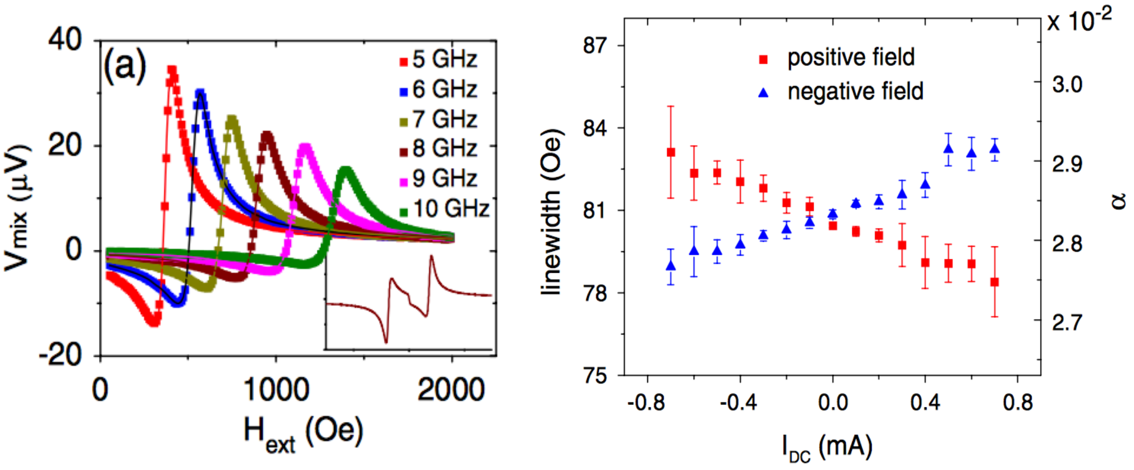

Figure 1.9.5 (Left) Experimental data for ST-FMR with various frequencies (Right) the effective modulation on damping parameters and HWHM with respect to DC [35]. Reprinted figures with the permission from L. Liu et al., Physical Review Letters, **109**, 186602 (2012). Copyright 2018 by the American Physical Society.

The current topic on ST-FMR in bilayer films is how accurately spin Hall angle is evaluated. In the first demonstration by Liu et al., they did not argue the contribution of spin diffusion length, spin mixing conductance, and related spin dependent effect. In 2012, K. Kondou et al. demonstrated the thickness dependence of FM and NM for spin Hall angles of NM in Py/Pt and Py/Pd bilayer films with SIR [50]. While they obtained the constant spin diffusion length $l_s$ of Pt and Pd of 1.2 and 2.0 nm which are independent of FM thickness, and also spin Hall angles of Pt and Pd according to the phenomenological equation $\eta = \eta_1[1 - \text{sech}\,(\frac{t}{l_s})]$. Here, $\eta_1$ is the evaluated spin Hall angle of HM and t is the thickness of FM. The equation implies that the zero thickness limit of FM provides the effective spin Hall angle without any contribution of ferromagnetic properties of FM. The obtained spin Hall angle of Pt and Pd at zero thickness limit are 0.022 and 0.008 while the spin Hall angle of Pt and Pd shows the thickness dependence of Py, which indicates that magnetic properties affects the evaluation of spin Hall angle in ST-FMR or rf-current flowing in Py influences to the evaluation as an inverse spin Hall effect or a non-uniform spin wave mode at the edge.

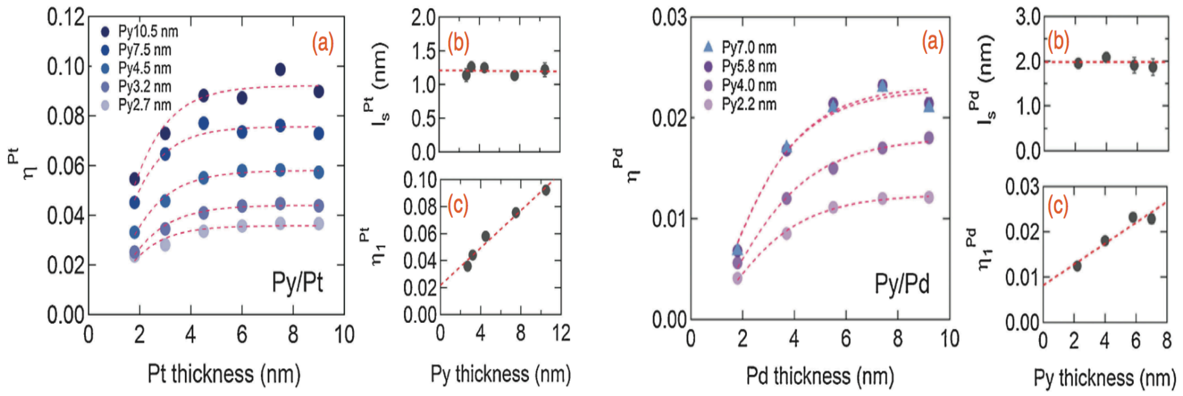

Figure 1.9.6 (Left) (a) Experimental data for Pt thickness dependence of the spin Hall angles (b) Py thickness dependence of spin diffusion length (c) the spin Hall angles of Pt. (Right) (a) Experimental data for Pd thickness dependence of the spin Hall angles, (b) Py thickness dependence of spin diffusion length and (c) the spin Hall angles of Pd, respectively [50]. Copyright 2018 The Japan Society of Applied Physics.

In 2014, S.Kasai et al. demonstrated the evaluation of spin Hall angles of Pt by using EDM method [51]. While Kondou et al shows the thickness dependence of spin Hall angles evaluated by SIR method, Kasai et al. shows the constant spin Hall angle of Pt, which reveals that the EDM method is better evaluation method than SIR and rf current possibly induces the unexpected phenomena and/or effects such as the inverse spin Hall effect, spin Hall magnetoresistance and non-uniform spin waves mode.

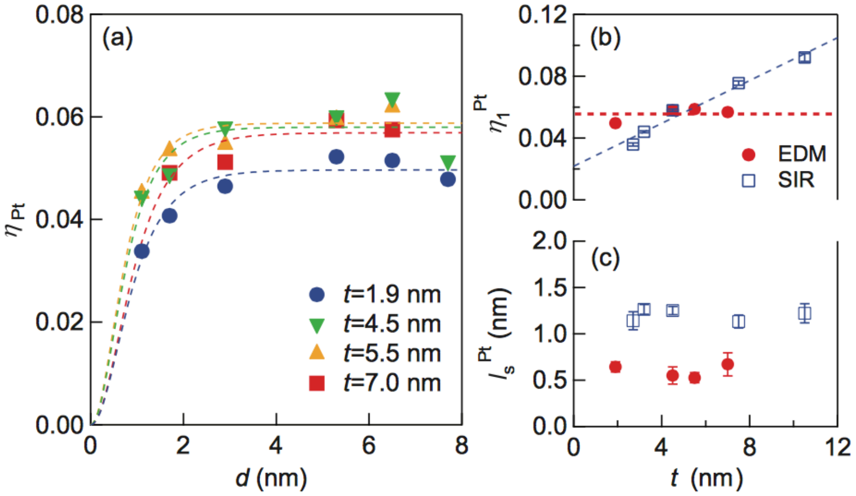

Figure 1.9.7 (a) the spin Hall angles of Pt on the various Py thicknesses (b,c) the spin Hall angles and spin diffusion length of Pt on various Py thicknesses with the SIR and EDM, respectively [51]. Reprinted from S. Kasai et al., Applied Physics. Letters. **104**, 092408 (2014), with the permission of AIP Publishing.

A. Guangly et al., compared ST-FMR spectra and the evaluated spin Hall angles in Py/Pt and CoFe/Pt [64]. Firstly, they demonstrated the spin Hall angles with SIR with zero thickness limit and obtained 0.022 in both films, which suggests that the evaluated spin Hall angles in zero thickness limit is independent of the materials of FM. In addition, they compared the sloops of thickness dependence of the evaluated spin Hall angles in SIR and determined that the sloop in CoFe/Pt films is larger than that of Py/Pt. they considered the reason why the sloop in CoFe/Pt is larger is the inverse spin Hall effect. The inverse spin Hall effect is related to spin mixing conductance which is proportional to the saturation magnetization. The saturation magnetization of CoFe and Py are 2.3T and 1.0T in their study, respectively, so that it is expected that the sloop of CoFe/Pt is larger than that in Py/Pt. Moreover, CoFe shows the smaller AMR compared to Py, indicating that the influence of ISHE to ST-FMR spectra in CoFe/Pt is relatively higher than that in Py/Pt. In the paper, they show the FM thickness dependence of the spin Hall angles evaluated by EDM method. The evaluated spin Hall angles in CoFe/Pt and Py/Pt are independent of the FM thickness, and the value of CoFe/Pt and Py/Pt is obtained to be 0.085 and 0.056, respectively. The origin of the difference is not clear yet. The paper concludes that the evaluated spin Hall angles by using SIR and EDM are not good agreement with each other, and the FM thickness dependence of the evaluated spin Hall angles in SIR is possibly the ISHE.

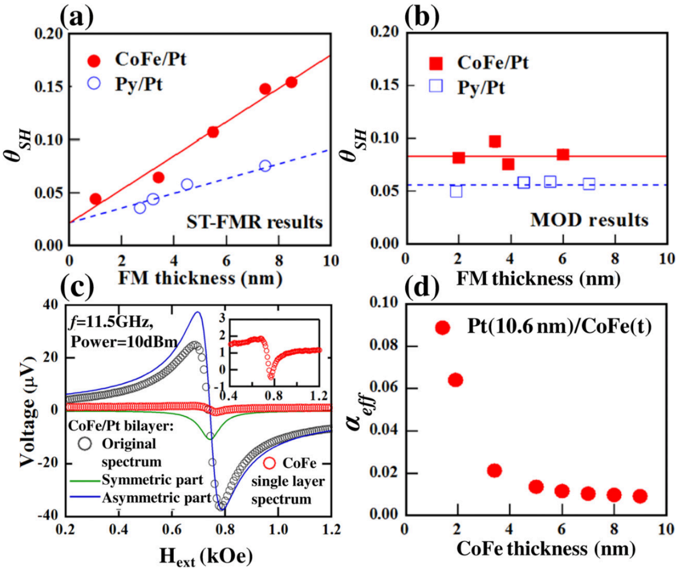

Figure 1.9.8 FM thickness dependence of Spin Hall angles of Pt in (a) The SIR and (b) EDM. (c) ST-FMR spectrum with 11.5 GHz (d) the damping parameter on CoFe thickness [64]. Reprinted from A. Ganguly et al., Applied Physics. Letters. **104**, 072405 (2014), with the permission of AIP Publishing.

Kondou et al., in 2016 showed further investigation on the contribution of the ISHE in ST-FMR by using CoFeB/Ta and Py/Ta, and They evaluated $\eta = \frac{V_{ST-FMR}}{V_{ST-FMR}+V_{ISHE}}$ [53]. They obtained 0.39 and 0.99 of η in CoFeB/Pt and Py/Ta, which suggests that CoFeB/Ta shows quite large contribution of the ISHE to ST-FMR spectra compared to Py/Ta. The differences are caused by the AMR and the resistivity of FM. The AMR of CoFeB (0.06%) is quite low compared to Py (1.6%), and the resistivity of CoFeB and Py is 190 and 32μΩcm, respectively.

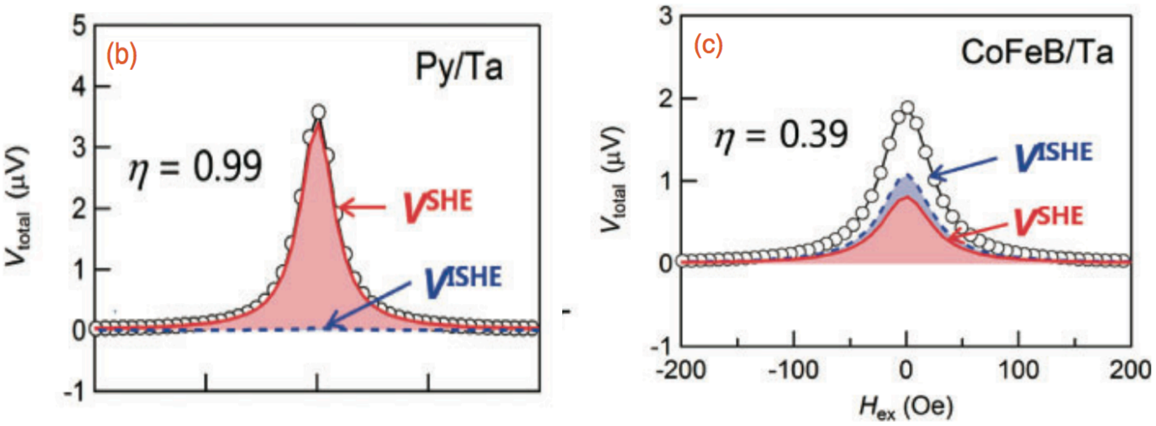

Figure 1.9.9 the experimental data of the components on SHE and ISHE in ST-FMR spectra in Py/Ta and CoFeB/Ta films [53]. Copyright 2018 The Japan Society of Applied Physics.

So far, while I introduced the problem on ST-FMR happening in the bulk, there exist the phenomena and/or effects at the interface between FM and HM. In the ST-FMR measurements, the exerted spin torques thorough the interface and the Oersted fields generated by charge currents in NM characterizes the spin Hall angles. In the condition that the interface is transparent, namely the generated spin torques are completely injected into FM and influence to the magnetic dynamics. To account for the phenomena and/or effects happening at the interface, the spin diffusion length of FM, the spin memory loss effect and transparency have been discussed.

Y. Wang et al., in 2014 discussed ST-FMR with spin diffusion length of FM [54]. As mentioned before, the spin Hall angles evaluated by SIR method show the FM thickness dependence while the spin Hall angles should be constant at any FM thickness. However, their data somehow does not show linear FM thickness dependence on spin Hall angles so that several possibilities to fit the observed spin Hall angles against FM thicknesses can be considered. To find the best-fit curve, they applied the equation $\tau_{ST}^{Total} = J_S \cos(\theta)\,(k_0^2/k^2)\,[\cosh(kt) - 1]/\cosh(kt)$ to review the total injected spin torques into FM and thus the spin Hall angles. Here, $k = \sqrt{\lambda_s^2 + \lambda_\phi^2}, k_0 = \sqrt{\lambda_\phi^2}$, where $\lambda_s$ and $\lambda_\phi$ are the spin diffusion length and the spin decoherence length of FM, respectively. They finally deduced the spin Hall angle of Pt to be 0.068 that is consistent with other studies.

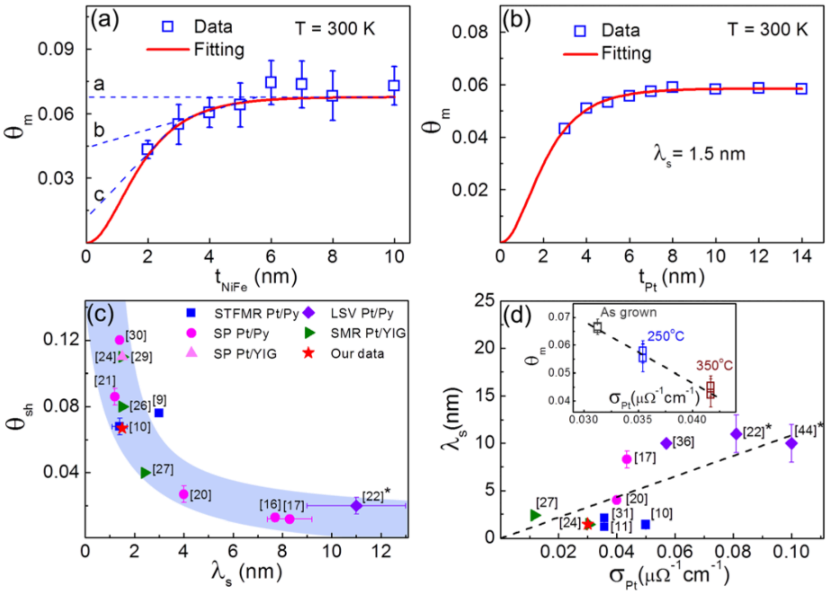

Figure 1.9.10 (a) the spin Hall angles of Pt on Py thickness (b) with the best filling curve with the spin diffusion length of Pt to be 1.5nm (c) The spin Hall angles on spin diffusion length of Pt in previous reports. (d) Spin diffusion length on the spin Hall conductivity of Pt [54]. Reprinted from Y. Wang et al., Applied Physics. Letters. **104**, 152412 (2014), with the permission of AIP Publishing.

The spin memory loss effect and the transparency were proposed to understand how the spin torques would be transmitted to the FM through the FM/HM interface. The spin memory loss effect proposed and applied to the spin pumping by J.-C. Rojas-Sánchez et al., in 2014 is the effect happening at the interface and expresses the ratio of injected spin torques into the ferromagnetic layer versus the total spin torques incident at the FM/NM interface [55]. On the other hand, the transparency was applied by W. Zhang et al., in 2015. In the paper by Zhang et al., they verified how much the spin memory loss effect works in their samples [56]. They tried to rule out the spin memory loss effect by inserting the Cu layer between FM and HM which possesses the low spin orbit interaction so that little spin-flip scattering occurs at the interface between FM/Cu and HM/Cu. They compared Py/Cu/Pt and Co/Cu/Pt samples on spin Hall angels and, they found the less decrease of spin Hall angles in Co/Cu/Pt films on the Cu thickness compared to those in Py/Cu/Pt films due to the elimination of proximity effects in Co/Cu/Pt films. Moreover, they compared the experimental and theoretical spin Hall angles in Co/Pt and Py/Pt films by taking the spin memory loss effect into account, and they demonstrated that the spin Hall angles in Co/Pt is theoretically 10 times larger than that of Py/Pt although the spin Hall angles in Co/Pt is experimentally 2 times larger than that of Py/Pt, which is not consistent with each other. Despite their clear demonstration on the transparency and spin memory loss effect, they are still in debates.

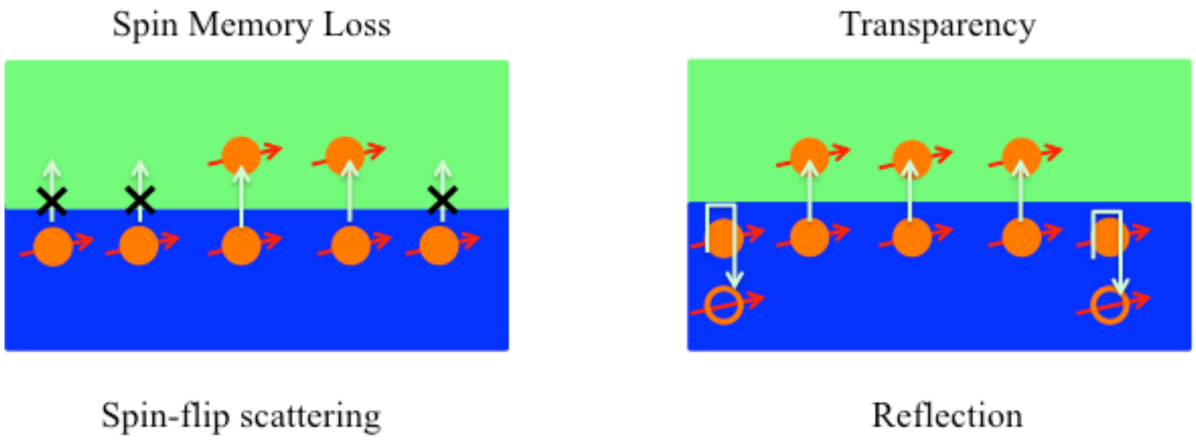

Figure 1.9.11 the schematic illustrations for the spin memory loss effect and the transparency

I would like to summarize this section. First demonstration on ST-FMR by L.Liu et al., was not enough to fully describe the phenomenon on ST-FMR so that many researches have performed especially in order to evaluate authentic spin Hall angle. There are three problems remained. One is the thickness dependence on the spin Hall angle in SIR. Every candidate I mentioned above is experimentally denied including non-uniform spin wave mode at the edges. Second thing is the interface problem. Still, there is a heated debate in which the spin memory loss effect and the transparency are more reliable and reasonable for ST-FMR. The problem is related to materials and mixing conductance so that it is possible to consider that we need more time to solve the problems. The last problem is the materials dependence of the spin Hall angle evaluated by the EDM. I think the problem is related to second problem. Finally, to conclude this section, I consider that ST-FMR is useful to roughly evaluate spin Hall angle but now it is not easy to identify the authentic spin Hall angle because of many problems I mentioned.

What is the evaluated spin hall angle in this study? The spin Hall angle described by L.Liu et al, is written to be $\eta = j_S/j_c$, where $j_s$ and $j_c$ are spin current injected into FM from HM and charge current density applied into HM, respectively. Therefore, the ratio can be considered to be the efficiency of spin injection from HM into FM, which indicates that the authentic spin Hall angle is larger than the efficiency of spin injection obtained in ST-FMR measurement based on the model described by L. Liu et al [35].

### 1.10 Potential Device Application of A Ferromagnetic/Heavy Metal Bilayer Films

As mentioned in the section 1.5, the spin transfer torques caused by direct current flowing in HM can modulate the effective damping parameter which characterizes the dissipative effect in magnetization dynamics. If the torques characterized by the damping parameter, so-called the damping torque, is compensated by the spin torques due to direct currents, the spin Hall auto oscillation can be realized, and moreover it is possible to realize magnetization switching when the spin torques overcomes the damping torques.

Z. Duan et al., in 2014 demonstrated the spin torque auto oscillator in low temperature regions [26]. The oscillator gives rise to magnetization dynamics and the related microwave voltage. While auto oscillators due to spin transfer torque had already been realized with MTJ, it is difficult to realize one with large devices because of the characteristic problem on MTJ. The diameter is 325 nm in the paper demonstrated by S. Tsunegi et al., in 2016 [34]. On the other hand, the FM/NM bilayer could show the spin Hall auto oscillation in a rectangular device in 0.16μm in width and 6μm in length, which is larger device compared to the MTJs. While the oscillation in FM/NM films occurs via AMR so that the magnitude of the emission spectrum is small compared to MTJs, the realization of the oscillation with larger devices is the merit of the spin Hall oscillation. It should be noted that the sample should be narrower than the characteristic length on the four-magnon scattering to kill the non-linear magnon scattering. Until now, it is still quite difficult to realize the spin Hall auto oscillation in FM/HM bilayer films at R.T. because spin Hall angle is so small that the direct currents more than $1\times10^{12}$A/m$^2$ is required, which suggests that the Joule heating effect is quite large. The suppression of the Joule heating effects is quite important because the saturation magnetization decrease with increasing the device temperature according to the Curie–Weiss law. To realize the spin Hall auto oscillation working at R.T., it is needed to solve the problem.

As is mentioned before, the spin Hall auto oscillation in FM/HM bilayer films is difficult to be developed while the spin Hall auto oscillation by using 3-terminal MTJ was already demonstrated by L.Liu et al., in 2012 [31]. At the same time, the magnetization switching was demonstrated by L. Liu et al., in 2012 and it is another possible device application [25]. They achieved the auto oscillation and magnetization switching by using CoFeB/Ta films at R.T. The phenomenon is applicable to the MRAM technology so that it enables to develop the next generation MRAM.

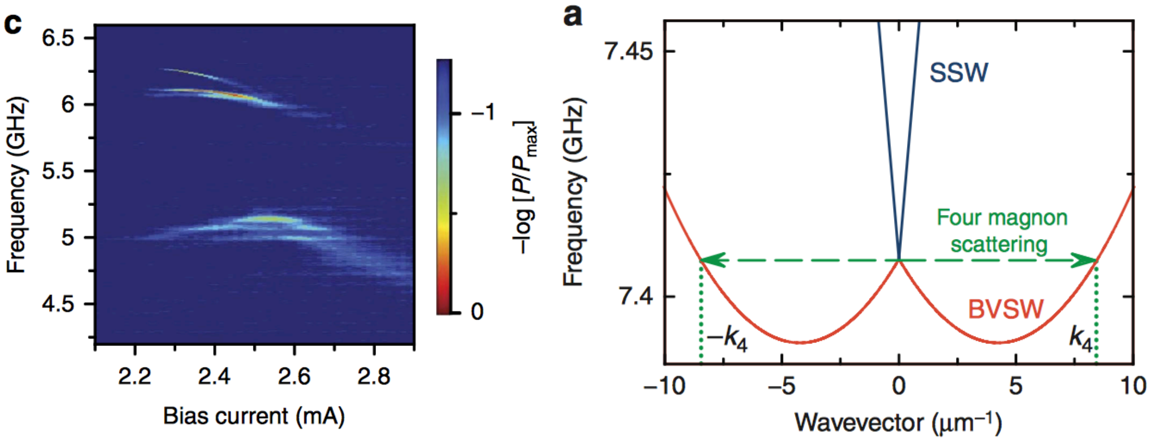

Figure 1.10.1 (Left) Experimetal data for spin Hall auto oscillation (Right) Calculated Spin wave dispersion relation for backward volume spin waves(red) and surface spin waves (blue) modes [26]. Reprinted figures from Z. Duan et al., Nature Communications **5**, 5616 (2014), with the permission of Springer Nature.

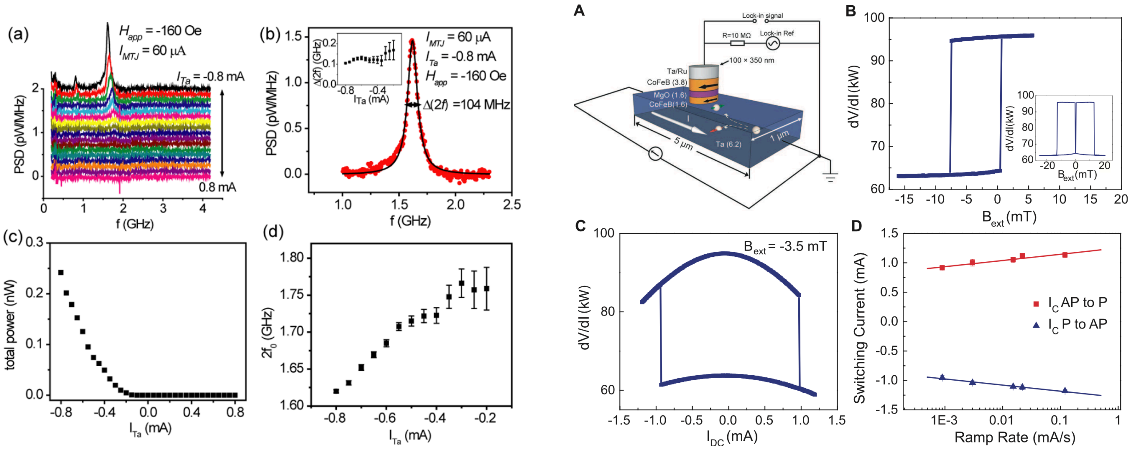

Figure 1.10.2 (Left) Experimental data on Spin Hall auto oscillation in MTJs [31]. Reprinted figures with permission from L. Liu et al., Physical Review Letters **109**, 186602 (2012) with the permission from American Physical Society.
(Right) Experimental data on magnetization switching in MTJs [25]. Reprinted figures with permission from L. Liu et al., Science **336**, 555 (2012) with the permission from AAAS.

## 1.11 Comparison of The Spin Hall Angles Evaluated among Various Methods

It is known that the evaluated spin Hall angles were varied by the methods so that I will compare the spin Hall angles obtained by various methods such as spin pumping, lateral spin valves, spin Hall magneto resistance effect and ST-FMR.The table 1.11.1 show the reported spin Hall angles by using spin pumping, lateral spin valves, spin Hall magnetoresistance and ST-FMR measurements.

The observed spin Hall angles by using spin pumping and ST-FMR measurements are comparable although those by using the lateral spin valve measurements are relatively small. Someone considers that the obtained values of spin Hall angles have a certain relation with spin diffusion shown in figure 1.9.10 (c). Until now, there are still debate on the reason why spin Hall angles are varied by methods.

Table 1.9.1 the observed spin Hall angles in previous reports

| | **Spin Hall angle** | **Measurement** | **Reference** |
|---|---|---|---|
| Co/Pt | 0.056 | Spin pumping | 55 |
| Py/Pt | 0.006-0.08 | Spin pumping | 36, 55, 63, 66, 67, 68, 70, 71, 72, 73 |
| Py/Pt | 0.022-0.19 | ST-FMR | 35, 50, 51, 52, 53, 54, 56 |
| CoFe/Pt | 0.022-0.085 | ST-FMR | 64 |
| YIG/Pt | 0.03 | Spin pumping | 74, 75 |
| YIG/Pt | 0.08 | SMR | 76 |
| Py/Pt | 0.0037-0.021 | LSV | 12, 62 |

### 1.12 Motivation

ST-FMR by using FM/HM bilayer films is firstly demonstrated by Liu.et al. [35] The FMR is excited by the two kinds of torques; one is the spin transfer torque caused by the spin Hall effect and the other is the torque caused by the Oersted field due to the electric current in the HM layer In this spin Hall effect induced ST-FMR, spin Hall angles of HM can be easily evaluated through the analysis methods called the spectrum intensity ratio (SIR) and the effective damping modulation (EDM). However, it has also been suggested that their model analyses should be too simple to evaluate authentic spin Hall angles, while the ST-FMR has several advantages compared to other methods. As the problems on the ST-FMR are discussed in this chapter, further systematic studies are needed to establish the ST-FMR technique In the spintronic device application, evaluation of spin Hall angles (or efficiency of spin current generation) for materials is of particular importance. A three-terminal device architecture was demonstrated for the development of next-generation magnetic random access memories that work with spin transfer torques due to the spin Hall effect [21, 25]. Further, the EDM method is expected to develop into the spin Hall auto oscillation [23, 24, 26].

In this study, interface perpendicular magnetic anisotropy was first investigated in Py/Pt bilayer films, where Py and Pt are chosen as FM and HM layers, respectively. If enhancement of the interface perpendicular magnetic anisotropy is obtained, it can decrease the magnitude of the applied direct currents needed to implement magnetization switching and spin Hall auto oscillations.

In the main part of this study, the ST-FMR phenomena in the Py/Pt bilayer films and the spin Hall angle of Pt were systematically investigated in the framework of the SIR and EDM methods. In particular, the dependence of ST-FMR on the external magnetic field direction was examined in detail. In fact, although the magnetic field direction dependence certainly includes rich information about the magnetization dynamics of ST-FMR, it has been little investigated in previous studies. Through these experimental studies, I aimed at contributing to the establishment of the spin Hall effect induced ST-FMR technique that can be a powerful tool to develop HM materials for MRAM and auto oscillation applications, as well as the better understanding on the ST-FMR phenomena.

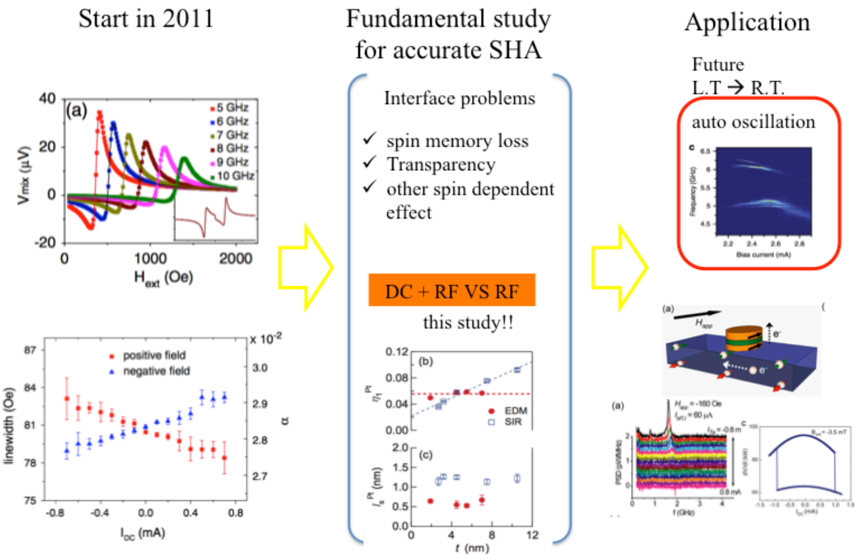

Figure 1.11.1 History and the position of this study in ST-FMR researches

## References

[1] M. N. Baibich, J. M. Broto, A. Fert, F. Nguyen Van Dau, F. Petroff, P. Etienne, G. Creuzet, A. Friederich, and J. Chazelas.
Giant Magnetoresistance of (001)Fe/(001)Cr Magnetic Superlattices.
Phys. Rev. Lett**.** **61**, 2472 (1988).

[2] G. Binasch, P. Grünberg, F. Saurenbach, and W. Zinn.
Enhanced magnetoresistance in layered magnetic structures with antiferromagnetic interlayer exchange.
Phys. Rev. B **39**, 4828(R) (1989).

[3] J.Bass.
CPP magnetoresistance of magnetic multilayers: A critical review.
J.Magn.Magn.Mater., **408**.15 (2016).

[4] J.M. Daughton.
GMR applications.
J.Magn.Magn.Mater., **192** 224 (1999).

[5] T. Valet and A. Fert.
Theory of the perpendicular magnetoresistance in magnetic multilayers.
Phys. Rev. B **48**, 7099 (1993).

[6] M. Jullière.
Tunneling between ferromagnetic films
Phys. Lett. A **54**, 225 (1975).

[7] S. S. P. Parkin, C. Kaiser, A. Panchula, P. M. Rice, B. Hughes, M. Samant, and S. H. Yang.
Giant tunnelling magnetoresistance at room temperature with MgO (100) tunnel barriers.
Nat. Mater. **3**, 862 (2004).

[8] S. Yuasa, A. Fukushima, T. Nagahama, K. Ando, and Y. Suzuki.
Giant room-temperature magnetoresistance in single-crystal Fe/MgO/Fe magnetic tunnel junctions
Nat. Mater. **3**, 868 (2004).

[9] J. C. Slonczewski.
Current-driven excitation of magnetic multilayers.
J. Magn. Magn. Mater. **159**, 1 (1996).

[10] L. Berger.
Emission of spin waves by a magnetic multilayer traversed by a current.
Phys. Rev. B **54**, 9353–9358 (1996).

[11] S. O. Valenzuela and M. Tinkam.
Direct electronic measurement of the spin Hall effect.
Nature **442**, 176 (2006).

[12] T. Kimura, Y. Otani, T. Sato, S. Takahashi, and S. Maekawa.
Room-Temperature Reversible Spin Hall Effect.
Phys. Rev. Lett. **98**, 156601 (2007).

[13] M. I. Dyakonov and V. I. Perel.
Current-induced spin orientation of electrons in semiconductors
Phys. A **35**, 459 (1971).

[14] Y. K. Kato, R. C. Myers, A. C. Gossard, and D. D. Awschalom.
Observation of the Spin Hall Effect in Semiconductors.
Science **306**, 1910 (2004).

[15] S. Murakami, N. Nagaosa, and S.-C. Zhang.
Dissipationless Quantum Spin Current at Room Temperature.
Science **301**,1348 (2003).

[16] Hans-Andreas Engel, Bertrand I. Halperin, and Emmanuel I. Rashba.
Theory of Spin Hall Conductivity in n-Doped GaAs.
Phys. Rev. Lett. **95**, 166605 (2005).

[17] R. V. Shchelushkin and Arne Brataas.
Spin Hall effects in diffusive normal metals.
Phys. Rev. B **71**, 045123 (2005).

[18] G. Y. Guo, S. Murakami, T.-W. Chen, and N. Nagaosa.
Intrinsic Spin Hall Effect in Platinum: First-Principles Calculations.
Phys. Rev. Lett. **100**, 096401 (2008).

[19] T. Tanaka, H. Kontani, M. Naito, T. Naito, D. S. Hirashima, K. Yamada, and J. Inoue.
Intrinsic spin Hall effect and orbital Hall effect in 4d and 5d transition metals.
Phys. Rev. B **77**, 165117 (2008).

[20] Y. Niimi, Y. Kawanishi, D. H. Wei, C. Deranlot, H. X. Yang, M. Chshiev, T. Valet, A. Fert, and Y. Otani.
Giant Spin Hall Effect Induced by Skew Scattering from Bismuth Impurities inside Thin Film CuBi Alloys.
Phys. Rev. Lett. **109**, 156602 (2012).

[21] M. Yamanouchi, L.Chen, J. Kim, M. Hayashi, H, Sato, S. Fukami, S. Ikeda, F. Matsukura and H. Ohno.

Three terminal magnetic tunnel junction utilizing the spin Hall effect of iridium-doped copper.
Appl. Phys. Lett. **102**, 212408 (2013).

[22] S. Zhang, P. M. Levy, and A. Fert.
Mechanisms of Spin-Polarized Current-Driven Magnetization Switching.
Phys. Rev. Lett. **88**, 236601 (2002).

[23] V. E. Demidov, S. Urazhdin, H. Ulrichs, V. Tiberkevich, A. Slavin, D. Baither, G. Schmitz, and S. O. Demokritov.
Magnetic nano-oscillator driven by pure spin current.
Nat. Mater. **11**, 1028 (2012).

[24] R. H. Liu, W. L. Lim, and S. Urazhdin.
Spectral Characteristics of the Microwave Emission by the Spin Hall Nano-Oscillator.
Phys. Rev. Lett. **110**, 147601 (2013).

[25] L. Liu, C.-F. Pai, Y. Li, H. W. Tseng, D. C. Ralph, and R. A. Buhrman.
Spin-Torque Switching with the Giant Spin Hall Effect of Tantalum.
Science **336**, 555 (2012).

[26] Z. Duan, A. Smith, L. Yang, B. Youngblood, J. Lindner, V. E. Demidov, S. O. Demokritov, and I. N. Krivorotov.
Nanowire spin torque oscillator driven by spin orbit torques.
Nat. Commu. **5**, 5616 (2014).

[27] J.A. Katine, F. J. Albert, R. A. Buhrman, E. B. Myers, and D. C. Ralph.
Current-Driven Magnetization Reversal and Spin-Wave Excitations in Co /Cu /Co Pillars.
Phys. Rev. Lett. **84**, 3149 (2000).

[28] Z. Diao, D. Apalkov, M. Pakala, Y. Ding, A. Panchula, and Y. Huai.
Spin transfer switching and spin polarization in magnetic tunnel junctions with MgO and $AlO_x$ barriers.
Appl. Phys. Lett. **87**, 232502 (2005).

[29] H. Sukegawa, Z. C. Wen, K. Kondou, S. Kasai, S. Mitani, and K. Inomata.
Spin-transfer switching in full-Heusler $Co_2FeAl$-based magnetic tunnel junctions.
Appl. Phys. Lett. **100**, (2012) 182403.

[30] H. Sukegawa, S. Kasai, T. Furubayashi, S. Mitani, and K. Inomata.
Spin-transfer switching in an epitaxial spin-valve nanopillar with a full-Heusler $Co_2FeAl_{0.5}Si_{0.5}$ alloy.
Appl. Phys. Lett. **96**, 042508 (2010).

[31] L. Liu, C. F. Pai, D. C. Ralph, and R. A. Buhrman

Magnetic Oscillations Driven by the Spin Hall Effect in 3-Terminal Magnetic Tunnel Junction Devices
Phys. Rev. Lett **109**, 186602 (2012)

[32] M. Tsoi, A. G. M. Jansen, J. Bass, W.-C. Chiang, M. Seck, V. Tsoi, and P. Wyder.
Excitation of a Magnetic Multilayer by an Electric Current.
Phys. Rev. Lett. **80**, 4281 (1998).

[33] S. I. Kiselev, J. C. Sankey, I. N. Krivorotov, N. C. Emley, R. J. Schoelkopf, R. A. Buhrman and D. C. Ralph.
Microwave oscillations of a nanomagnet driven by a spin-polarized current.
Nature **425**, 380 (2003).

[34] S. Tsunegi, K. Yakushiji, A. Fukushima, S. Yuasa, and H. Kubota.
Microwave emission power exceeding 10 μW in spin torque vortex oscillator.
Appl. Phys. Lett. **109**, 252402 (2016).

[35] L. Liu, T. Moriyama, D. C. Ralph, and R. A. Buhrman.
Spin-Torque Ferromagnetic Resonance Induced by the Spin Hall Effect.
Phys. Rev. Lett. **106**, 036601 (2011).

[36] K. Ando, S. Takahashi, K. Harii, K. Sasage, J. Ieda, S. Maekawa, and E. Saitoh.
Electric Manipulation of Spin Relaxation Using the Spin Hall Effect
Phys. Rev. Lett. **101**, 036601 (2008).

[37] J. Bass, and W. P. Pratt.
Spin-diffusion lengths in metals and alloys, and spin-flipping at metal/metal interfaces:
an experimentalist's critical review.
J. Phys.: codens. Matter **19**, 183201 (2007).

[38] S. Takahashi, and S. Maekawa.
Spin Current in Metals and Superconductors.
J. Phys. Soc. Jpn. **77**, 031009 (2008).

[39] I. Galanakis, and P. Mavropoulos.
Zinc-blende compounds of transition elements with N, P, As, Sb, S, Se, and Te as half-metallic systems.
Phys. Rev. B **67**, 104417 (2003).

[40] L. D. Landau, and E. M. Lifshitz.
On the Theory of the Dispersion of Magnetic Permeability in Ferromagnetic bodies.
Phys. Z. Sowjet. **8**, 153 (1935).

[41] J. H. E. Griffiths.
Anomalous High-frequency Resistance of Ferromagnetic Metals.

Nature **158**, 670, (1946).

[42] C. Kittel.
On the Theory of Ferromagnetic Resonance Absorption
Phys. Rev. **73**, 155 (1948).

[43] T. L. Gilbert.
A Phenomenological Theory of Damping in Ferromagnetic Materials.
IEEE. Trams. Magn **40**, 6 (2004).

[44] S. Ikeda, K. Miura, H. Yamamoto, K. Mizunuma, H. D. Gan, M. Endo, S. Kanai, J. Hayakawa,F. Matsukura, and H. Ohno.
A perpendicular-anisotropy CoFeB–MgO magnetic tunnel junction.
Nature Mater. **9**, 721-724 (2010)

[45] H. X. Yang, M. Chshiev, B. Dieny, J. H. Lee, A. Manchon, and K. H. Shin
First-principles investigation of the very large perpendicular magnetic anisotropy at Fe|MgO and Co|MgO interfaces
Phys. Rev. B **84**, 054401 (2011)

[46] J. W. Koo, S. Mitani, T. T. Sasaki, H. Sukegawa, Z. C. Wen, T. Ohkubo, T. Niizeki, K.Inomata, and K. Hono
Large perpendicular magnetic anisotropy at Fe/MgO interface
Appl. Phys. Lett. **103**, 192401 (2013)

[47] F. J. A. den Broeder, W. Hoving, and P. J. H. Bloemen.
Magnetic anisotropy of multilayers.
J. Magn. Magn. Mater. 93, 562 (1991).

[48] D. Odkhuu, S. H. Rhim, N. Park, and S. C. Hong
Extremely large perpendicular magnetic anisotropy of an Fe(001) surface capped by 5d transition metal monolayers: A density functional study
Phys. Rev. B **88**, 184405 (2013)

[49] T. R. Mcguire, and R. I. Potter.
Anisotropic Magnetoresistance in Ferromagnetic 3d Alloys.
IEEE Trans. Magn **11**,4 (1975).

[50] K. Kondou, H. Sukegawa, S. Mitani, K. Tsukagoshi, and S. Kasai.
Evaluation of Spin Hall Angle and Spin Diffusion Length by Using Spin Current-Induced Ferromagnetic Resonance.
Appl. Phys. Express **5**, 073002 (2012).

[51] S. Kasai, K. Kondou, H. Sukegawa, S. Mitani, K. Tsukagoshi, and Y. Otani.
Modulation of effective damping constant using spin Hall effect.

Appl. Phys. Lett. **104**, 092408 (2014).

[52] S. Hirayama, S. Mitani, Y.Otani, and S. Kasai.
Anomalous modulation of spin torque-induced ferromagnetic resonance caused by direct currents in permalloy/platinum bilayer thin films.
Appl.Phys Express **11**, 013002 (2018).

[53] K. Kondou, H. Sukegawa, S. Kasai, S. Mitani, Y. Niimi, and Y. Otani,
Influence of inverse spin Hall effect in spin-torque ferromagnetic resonance measurements.
Appl. Phys. Express **9**, 023002 (2016).

[54] Y. Wang, P. Deorani, X. Qiu, J. H. Kwon, and H. Yang.
Determination of intrinsic spin Hall angle in Pt.
Appl. Phys. Lett. **105**, 152412 (2014).

[55] J.-C. Rojas-Sánchez, N. Reyren, P. Laczkowski, W. Savero, J.-P. Attané, C. Deranlot, M. Jamet, J.-M. George, L. Vila, and H. Jaffrès.
Spin Pumping and Inverse Spin Hall Effect in Platinum: The Essential Role of Spin-Memory Loss at Metallic Interfaces.
Phys. Rev. Lett. **112**, 106602 (2014).

[56] W. Zhang, W. Han, X. Jiang, S. Yang, and S. S. P. Parkin.
Role of transparency of platinum–ferromagnet interfaces in determining the intrinsic magnitude of the spin Hall effect.
Nat. Phys. **11**, 496 (2015).

[57] K. Kondou, R. Yoshimi, A. Tsukazaki, Y. Fukuma, J. Matsuno, K. S. Takahashi, M. Kawasaki, Y. Tokura, and Y. Otani.
Fermi-level-dependent charge-to-spin current conversion by Dirac surface states of topological insulators,
Nat. Phys. **12**, 1027-1031 (2016).

[58] A. A. Tulapurkar, Y. Suzuki, A. Fukushima, H. Kubota, H. Maehara, K. Tsunekawa, D. D. Djayaprawira, N. Watanabe and S. Yuasa
Spin-torque diode effect in magnetic tunnel junctions
Nature 438,339 (2005)

[59] Y.Suzuki and H.Kubota
Spin-torque diode effect and its application
J.Phys.Soc.Jpn.**77**, 031002 (2008)

[60] R. Matsumoto, A. Chanthbouala, J. Grollier, V. Cros, A. Fert, K. Nishimura, Y. Nagamine, H. Maehara, K. Tsunekawa, A. Fukushima, and S. Yuasa
Spin-torque diode measurements of MgO-based magnetic tunnel junctions with asymmetric electrodes

Appl. Phys. Express **4**, 063001 (2011)

[61] Y. S. Gui, L. H. Bai, and C. M. Hu
The physics of spin rectification and its application
Sci, Chi. Phys. Mecha. and Astro. **56**, 121 (2013)

[62] Y. Niimi, and Y. Otani
Reciprocal spin Hall effects in conductors with strong spin–orbit coupling: a review
Rep. Prog. Phys. 78 124501 (2015).

[63] O. Mosendz, J.E. Pearson, F.Y. Fradin, G.E. W. Bauer, S.D. Bader, and A. Hoffmann
Quantifying Spin Hall Angles from Spin Pumping: Experiments and Theory
Phys. Rev. Lett **104**,046601 (2010).

[64] A. Ganguly, K. Kondou, H. Sukegawa, S. Mitani, S. Kasai, Y. Niimi, Y. Otani, and A. Barman
Thickness dependence of spin torque ferromagnetic resonance in $Co_{75}Fe_{25}$/Pt bilayer films
Appl. Phys. Lett. **104**, 072405 (2014)

[65] T. X. Nan , S. Emori , C. T. Boone , X. J. Wang , T. M. Oxholm , J. G. Jones , B. M. Howe , G. J. Brown , and N. X. Sun
Comparison of spin-orbit torques and spin pumping across NiFe/Pt and NiFe/Cu/Pt interfaces
Phys. Rev. B **91**, 214416 (2015)

[66] X. Zhou, M.Tang, X.L. Fan, X.P. Qiu, and S. M. Zhou
Disentanglement of bulk and interfacial spin Hall effect in ferromagnetic/normal metal interface
Phys. Rev. B **94**, 144427 (2016)

[67] O. Mosendz, V. Vlaminck. J.E. Pearson, F.Y. Fradin, G.E.W. Bauer, S.D. Bader, and A. Hoffmann
Detection and quantification of inverse spin Hall effect from spin pumping in permalloy/normal metal bilayers
Phys. Rev. B **82**, 214403 (2010)

[68] K. Ando, S. Takahashi, J. Ieda, Y, Kajiwara, H. Nakayama, T. Yoshino, K. Harii, Y. Fujikawa, M. Matsuo, S. Maekawa, and E. Saitoh
Inverse spin-Hall effect induced by spin pumping in metallic system
Jour. Appl. Phys. **109**, 103913 (2011)

[69] A. Azevedo, L. H. Vilela-leao, R.L.Rodriguez-Suarez, A.F. Lacerda Santos, and S.M. REzende
Spin pumping and anisotropic magnetoresistance voltages in magnetic bilayers: Theory and experiment

Phys. Rev. B **83**, 144402 (2011)

[70] Z. Feng, J. Hu, L. Sun, B. You, D. Wu, J. du, W. Zhang, A. Hu, Y. Yang, D. M. Tang, B. S. Zhang, and H.F. Ding
Spin Hall angle quantification from spin pumping and microwave photoresistance
Phys. Rev. B **85**, 214423 (2012)

[71] H. Nakayama, K. Ando, K. Harii, T. Yoshino, R. Takanashi, K. KAjiwara,K. Uchida, Y. Fujikawa, and E. Saitoh
Geometry dependence on inverse spin Hall effect induced by spin pumping in $Ni_{81}Fe_{19}$/Pt films
Phys. Rev.B **85**, 144408 (2012)

[72] V. Vlaminck, J.E. Pearson, S.D. Bader, and A. Hoffmann
Dependence of spin-pumping spin Hall effect measurements on layer thickness and stacking order
Phys. Rev. B **88**,064414 (2013)

[73] L. Bai, P. Hyde, Y.S. Gui, C.M.Hu, V. Vlaminck, J.E. Pearson, S.D. Bader, and A. Hoffmann
Universal method for separating spin Hall pumping from spin rectification voltage of ferromagnetic resonance
Phys. Rev. Lett **111**, 217602 (2013)

[74] C. Hahn, G. de Loubens, O Klein, M. Viret, V. V. Naletov, and J. Ben Youss
Comparative measurements of inverse spin Hall effects and magnetoresistance in YIG/Pt and YIG/Ta
Phys. Rev B **87**, 174417 (2013)

[75] N. Vlietstra, J Shan, V. Castel, J. Ben Youssef, G. E. Bauer, and B. J. van Wees
Exchange magnetic field torques in YIG/Pt bilayers observed by the spin-Hall magnetoresistance
Appl. Phys. Lett. **103**, 032401 (2013)

[76] H. Nakayama, M. Althammer, Y.T. Chen, K. Uchida, Y. Kajiwara, D. Kikuchi, T. Ohtani, S. Geprags. M. Opel, S. Takahashi, R. Gross, G. E. W. Bauer, S. T. B. Goennenwein, and E. Saitoh
Spin Hall magnetoresistance induced by a nonequilibrium proximity effect
Phy. Rev. Lett **110**, 206601 (2013)

## 2 Experimental Methods

This chapter describes the preparation condition of films and microfabrication for the device in this study and measurement set-up. Films for the interface perpendicular magnetic anisotropy (PMA) were constructed with Ta/Py/Pt on thermal oxidized non-doped Si substrates and those for spin torque ferromagnetic resonance (ST-FMR) were with Py/Pt on a-sapphire and a thermal oxidized non-doped Si substrate. Microfabrication was performed to realize the devices for ST-FMR. PMA study was performed by using a vibrating sample magnetometer (VSM) and ST-FMR study was performed by using a lock-in amplifier.

### 2.1 Film Preparation

All films in this study were prepared by using RF-sputtering system (ES-350,EIKO shown in Figure 2.1) and with the base pressure less than $5\times10^{-5}$ Pa. Films for PMA were deposited onto a thermal oxidized non-doped Si substrate while those for ST-FMR were onto a sapphire and a thermally oxidized non-doped Si substrate.

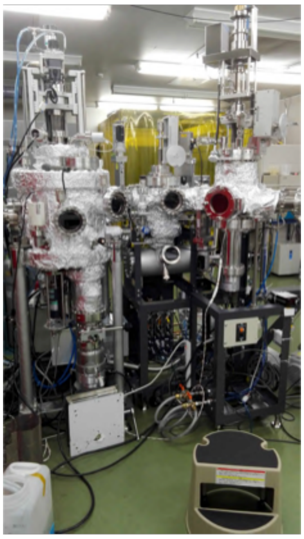

Figure 2.1.1 RF-magnetron sputtering

### 2.2 Microfabrication

Microfabrication was performed for pattering ST-FMR device into 0.2-1.0 μm in width and 6 μm in length. Our process includes 4 steps including the process on global marks, rectangular devices, small electrodes and big electrodes. It is worthy to mention that global marks play a necessary role to make precise devices with electron beam lithography (EBL). If more than twice lithography is required, global marks exhibit its importance for determination of the scanning area.

The first process is started after a preparation of films. PMMA (polymethyl methacrylate, micro resist technology GmbH, Germany) including MMA, 495MMA and 950MMA and ESPACER (SHOWA DENKO K.K., Japan) were utilized. PMMA is positive tone resist and ESPACER is conductive polymer to prevent charge-up during EBL. It is noted that PMMA can realized an undercut profile so that it is useful for deposition by rf-sputtering which has worse directionality than evaporation has. After the performance of EBL and development, Ta (10 nm)/Au (100 nm) bilayer was formed by using rf sputtering (ULVAC). Finally, remaining resists were removed.

The second process is for rectangular devices. HMDS (hexamethyldisilazan), ma-N1407(micro resist technology GmbH, Germany) and ESPACE were employed. HMDS work as a promoter and ma-N1407 is negative tone resist. After the performance of EBL and development, Ar-ion milling was employed to fabricate rectangular devices. The incident angle is firstly fixed at 45° and it will be changed to 10° that is almost normal to the substrate after film component is not detected by end-point detector to prevent re-deposition onto the sidewall. Finally remaining resists were removed, and the devices are fabricated into 6μm in length and 0.2, 0.6 and 1.0μm in width.

The third process is for small electrodes that are connections between rectangular devices and big electrodes. This process is completely same as the first one. However, the deposited thickness of Ta is varied to 3 nm from 10 nm because the resistivity of Ta is much higher than that of Au so that the thickness of Ta should be lower than that of Py to apply the current into Py.

The last process is for big electrodes that are formed through a photolithography process. HMDS and na-M2403 were used. Na-M2403 is a negative tone resist. After an exposure and a development, Ta (10nm)/Au (100nm) bilayer was formed by rf magnetron sputtering of ULVAC. Finally a remaining resist was removed.

### 2.3 Measurement

This section describes measurements in this study including PMA and ST-FMR study. In PMA study Vibrating sample magnetometer (VSM) was employed to obtained magnetic properties of Ta/Py/Pt trilayers. In ST-FMR study 3-terminal prober was employed to manipulate magnetic dynamics of Py/Pt.

#### 2.3.1 Vibrating Sample Magnetometer

VSM is a fundamental instrument for observing magnetic properties such as a saturation magnetization, coectivity and remanence. In this study LakeShore 7410 shown in figure 2.3.1 was employed and all measurements are performed at RT. Calibration for magnetic moment was performed with Ni plate that possesses 3.96 emu. In order to obtain hysteresis loops external magnetic fields were swept from 15 kOe to -15 kOe and reversed for both of In-plain and perpendicular configuration.

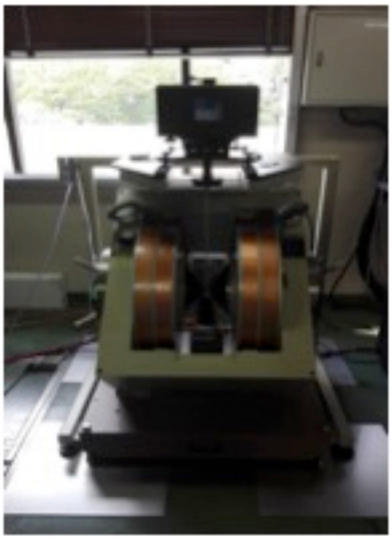

Figure 2.3.1 vibrating Sample Magnetometer

#### 2.3.2 3-Terminal Probe Measurement

3-terminal probe measurements shown in figure 2.3.2 were performed with a lock-in amplifier (LI5640, NF CORPORATION, Japan) and a signal generator (69147B, ANRITSU CORPORATION, Japan) for the spin torque ferromagnetic resonance (ST-FMR) with dc source (GS200, Yokogawa Electric Corporation, Japan). Also, the combination of a nano-voltmeter (2182A, Keithley Instruments, America) and a signal generator was employed. Moreover, in the case of the measurement for anisotropy magnetoresistance, the combination of the nano-voltmeter and another dc source (2400-C, Keithley Instruments, America) was utilized. External magnetic fields were applied (swept from 2.8 to 0 kOe). All measurements are performed at R.T.

A time constant of the lock-in amplifier was 300 ms and a measurement time for each point is 1000 ms. The Power and frequency of rf- current were varied and DC voltages also were varied.

Figure 2.3.3 shows the ST-FMR devices and GSG-prober that has a contact with Ta/Au electrodes. GSG prober is employed to make the more uniform Oersted field shown in figure 2.3.4. The Oersted field caused by applied currents into the device in GSG probers can be uniformly generated like the illustration compared to the GS prober case, which could realize better experimental conditions.

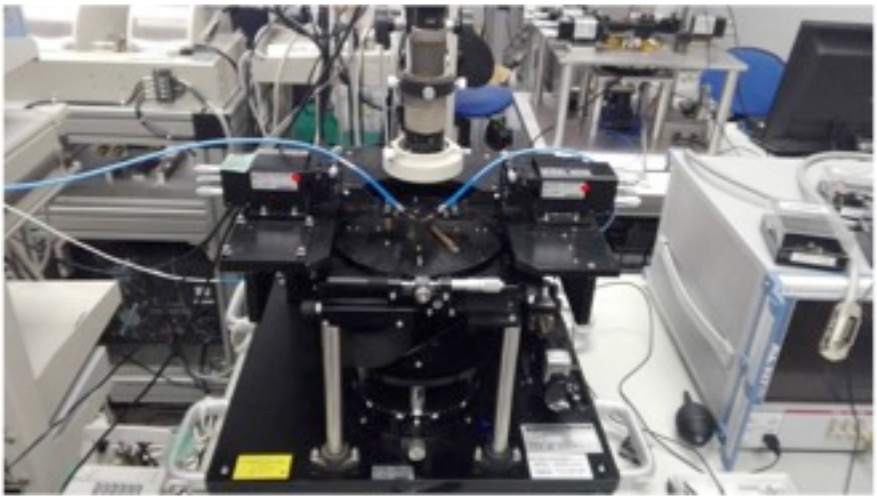

Figure 2.3.2 set-up of 3-terminal prober

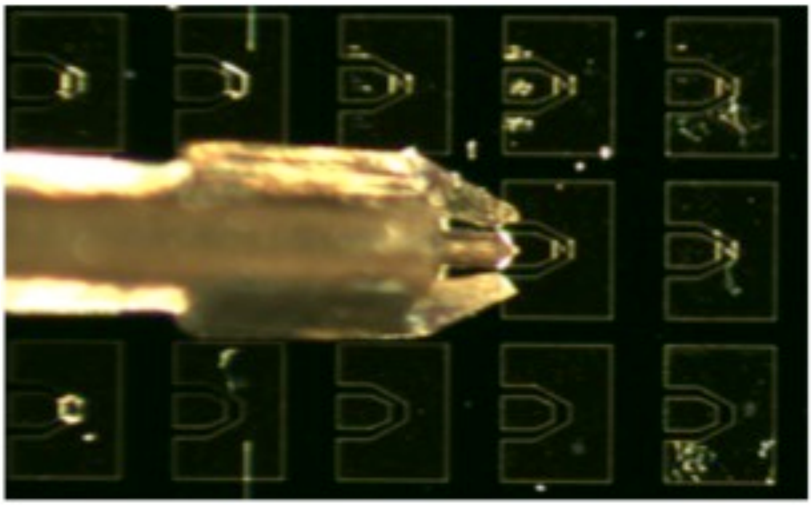

Figure 2.3.3 3-terminal prober and ST-FMR devices

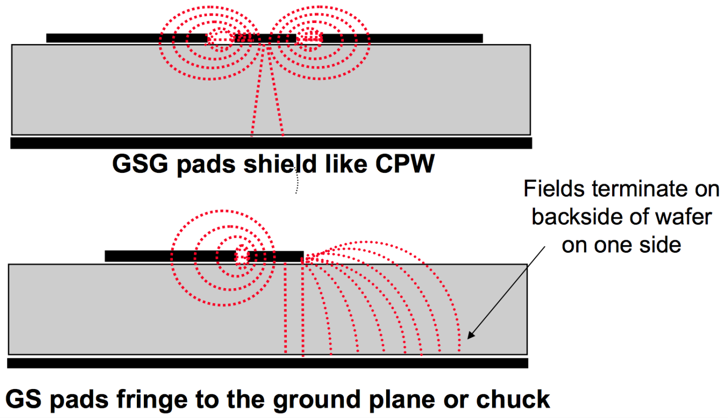

Figure 2.3.4 the merit of GSG probers by comparing GS prober with respect to the Oersted field [1]

### 2.3.3. Set-up and Amplitude Modulation for Measurement

Figure 2.3.5 shows the schematic illustration of the ST-FMR set-up. A signal generator with amplitude modulation (AM) was employed in order to apply rf current into the device and lock-in amplifier was employed in order to detect the output dc voltage.

AM is the method to convey the signal wave. A Lock-in amplifier gives a carrier wave, $V_c = E_c\cos(w_c t+\varphi)$, to the signal generator so that the signal generator which applies signal wave, $V_s = E_s\cos w_s t$, can apply the amplitude-modulated signal wave to the device. The amplitude-modulated signal $V_{am}=(E_c+kE_s\cos w_s t)\cos(w_c t+\varphi)$ can be written as follows, $V_{am}=E_c\cos w_c t+(kE_s/2)\cos(w_s+w_c)t+(kE_s/2)\cos(w_s-w_c)t$ (2.3.1). Therefore, three kinds of frequencies can be detected as $w_s$, $w_s+w_c$ and $w_s-w_c$ shown in Figure 2.3.6, and the voltage finally detected by the diode in lock-in amplifier via the bias-tee. In this experiment, $w_s$ and $w_c$ are selected as 12GHz and 50MHz, respectively, and the detected voltage in this experiment is characterized by the frequency $w_s+w_c$[2].

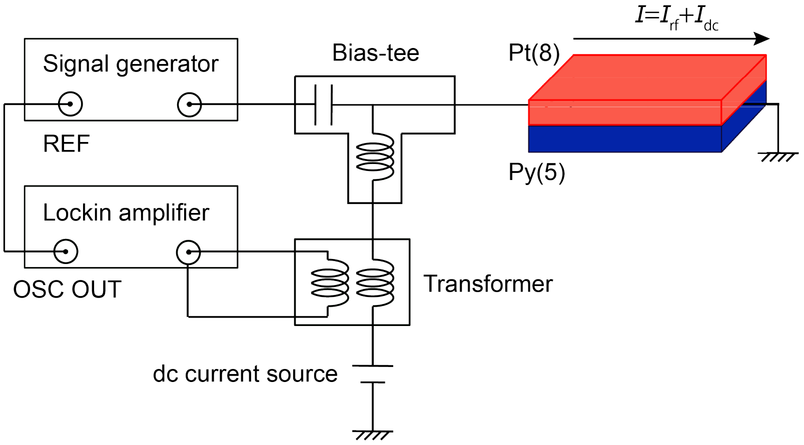

Figure 2.3.5 the schematic illustration for set-up on ST-FMR measurements

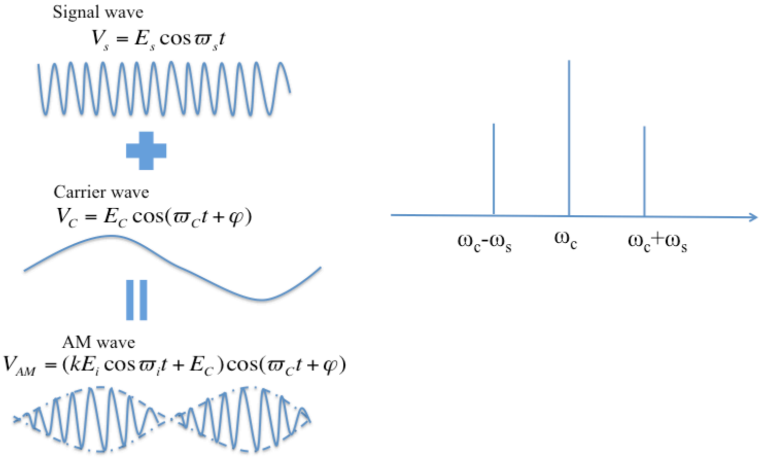

Figure2.3.6 schematic illustrations on amplitude modulations

The DC source is also employed in order to apply a direct current to modulate ST-FMR spectra and to detect the DC voltage. Bias-tee (K251, Anritsu, Japan) shown in figure 2.3.7 is one of diplexers and consisted of a condenser and coil, which enable to separate AC and DC components. Even though direct currents are applied into the device, the DC voltage $E_{const}$ characterized by the direct

currents is not detected in this study, which is advantage of AM. The characteristic voltage including dc voltage can be written as follows,
$V_{am} = (E_{const} + E_s\cos(w_s t) + E_c\cos(w_c t+\varphi))^2$
$=(E_{const})^2+(E_s)^2\cos^2(w_s t)+(E_c)^2\cos^2(w_c t+\varphi)+2E_{const}E_s\cos(w_s t)+2E_sE_c\cos(w_s t)\cos(w_c t+\varphi)$
$+2E_{const}E_c\cos(w_c t+\varphi)$ (2.3.2). As seen in the equation (2.3.2), the equation includes the term $\cos(w_s t)\cos(w_c t+\varphi)$, which is in accordance with equation (2.3.1) and indicating that the voltage at the frequency $w_s+w_c$ can be detected even under direct currents [2].

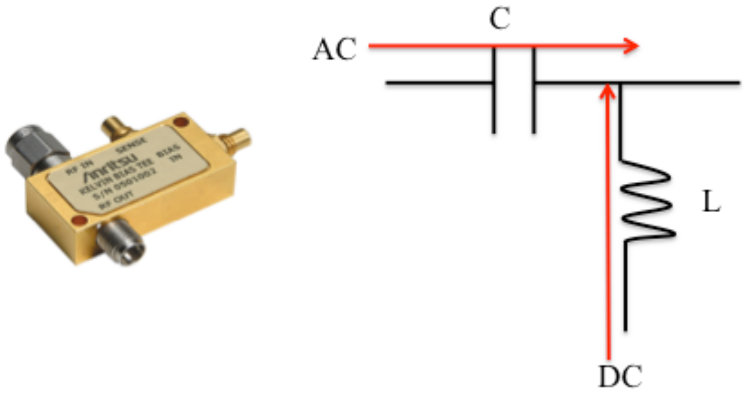

Figure 2.3.7 the bias-tee used in this study and the schematic illustration of bias-tee

Figure 2.3.8 shows a schematic illustration of the ST-FMR measurement. The in-plane external magnetic field $H_{ext}$ is applied to the film and the relative angle between the external magnetic field and rf-current direction is denoted as $\theta$. The external magnetic field is swept from 2.8kOe to 0kOe. In order to apply the current into the rectangular device, Ta (3 nm)/Au (100 nm) electrode is fabricated, and the frequency and power of rf-currents $I_{rf}$ are fixed at 12 GHz and 3dbm which corresponds to around $4.0\cdot10^{10}$A/m$^2$, respectively. In addition, direct current density $I_{dc}$ is varied from -2.52 to 2.52 $\cdot10^{11}$A/m$^2$ in Pt.

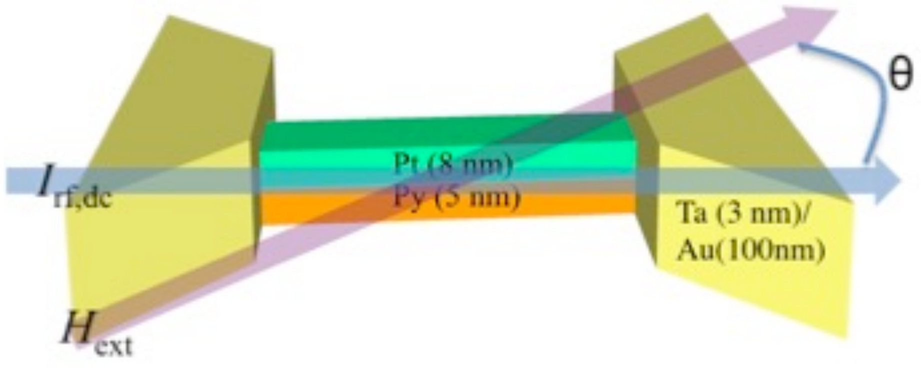

Figure 2.3.8 the schematic illustration of thePy/Pt bilayer films and the electrodes.

Reference

[1]: https://www.keysight.com/upload/cmc_upload/All/OnWaferMillimeter.pdf
[2]: http://oxford.ee.kanagawa-u.ac.jp/lspecs/nico/wp-content/uploads/sites/2/2014/06/AM.pdf

## 3. Interface Perpendicular Magnetic Anisotropy (PMA) of Ta/Py/Pt Layers

The interface PMA is widely studied [1-12, 18, 19] and a key parameter in a magnetization dynamics because an anisotropy filed including interface PMA influences a resonant condition of the FMR [13,14]. In this chapter, I would like to introduce the interface PMA of Ta/Py/Pt trilayer films measured by a vibrating sample magnetometer (VSM). The sample has the interface PMA energy density $K_\mathrm{i}$ as large as 0.17erg/cm$^2$ with a conventional dead layer model [15]. On the other hand, the observed saturation magnetizations ($M_\mathrm{S}$) as a function of the nominal thickness of the Py layer is in coincidence with the calculated saturation magnetization from saturation field of hard axis ($H_\mathrm{k}/4\pi$) as a function of the thickness, which suggests the interface PMA of the films could be fully interrupted as shape anisotropy, excluding any PMA effect.

### 3.1 Hysteresis Loops for Ta/Py/Pt trilayes at RT

In order to demonstrate the interface PMA of the films, the thickness dependence of magnetic anisotropy energy densities is checked because each film would have the same interface PMA, which indicates interface PMA could be evaluated with a following equation:

$K_\mathrm{i} = (K_\mathrm{u} - K_\mathrm{v}) \times t$ (3.1),

where $K_\mathrm{i}$ is an interface PMA energy density, $K_\mathrm{u}$ is a total PMA energy density, $K_\mathrm{v}$ is a total PMA energy density, and $t$ is a thickness of Py, respectively. $K_\mathrm{v}$ is a shape anisotropy energy density to be considered as $2\pi M_\mathrm{s}^2$ [1-12]. In this study, Ta(5 nm)/Py(t)/Pt(5 nm) films are prepared and the thickness of Py $t$ is varied from 1 to 5 nm and 82 nm.

Figure 3.1.1(a)-(f) shows a hysteresis loop for each thickness. The sample of 82 nm thick film is prepared for a test sample expectedly having a saturation magnetization comparable to bulk one that is considered to be around 800 emu/cc [16]. The hysteresis loop for the sample of 82 nm-thickness shown in figure 3.1.1(f) shows a saturation magnetization of 760 emu/cc, which is reasonable to be considered as that of a bulk Py. While the obtained values of saturation magnetizations is shown in table3.1.1, samples having a thickness of more than 4 nm are assumed to be able to keep a saturation magnetization of that of bulk. Reducing the thickness of Py, its saturation magnetization is reduced and it finally shows the hysteresis loop like a super-paramagnetic material, which indicates Py almost loses its own magnetization.

Table 3.1.1 the obtained saturation magnetizations

| | 1 nm | 2 nm | 3 nm | 4 nm | 5 nm | 82 nm |
|---|---|---|---|---|---|---|
| $M_\mathrm{s}$ (emu/cm$^3$) | 243 | 485 | 552 | 692 | 693 | 762 |

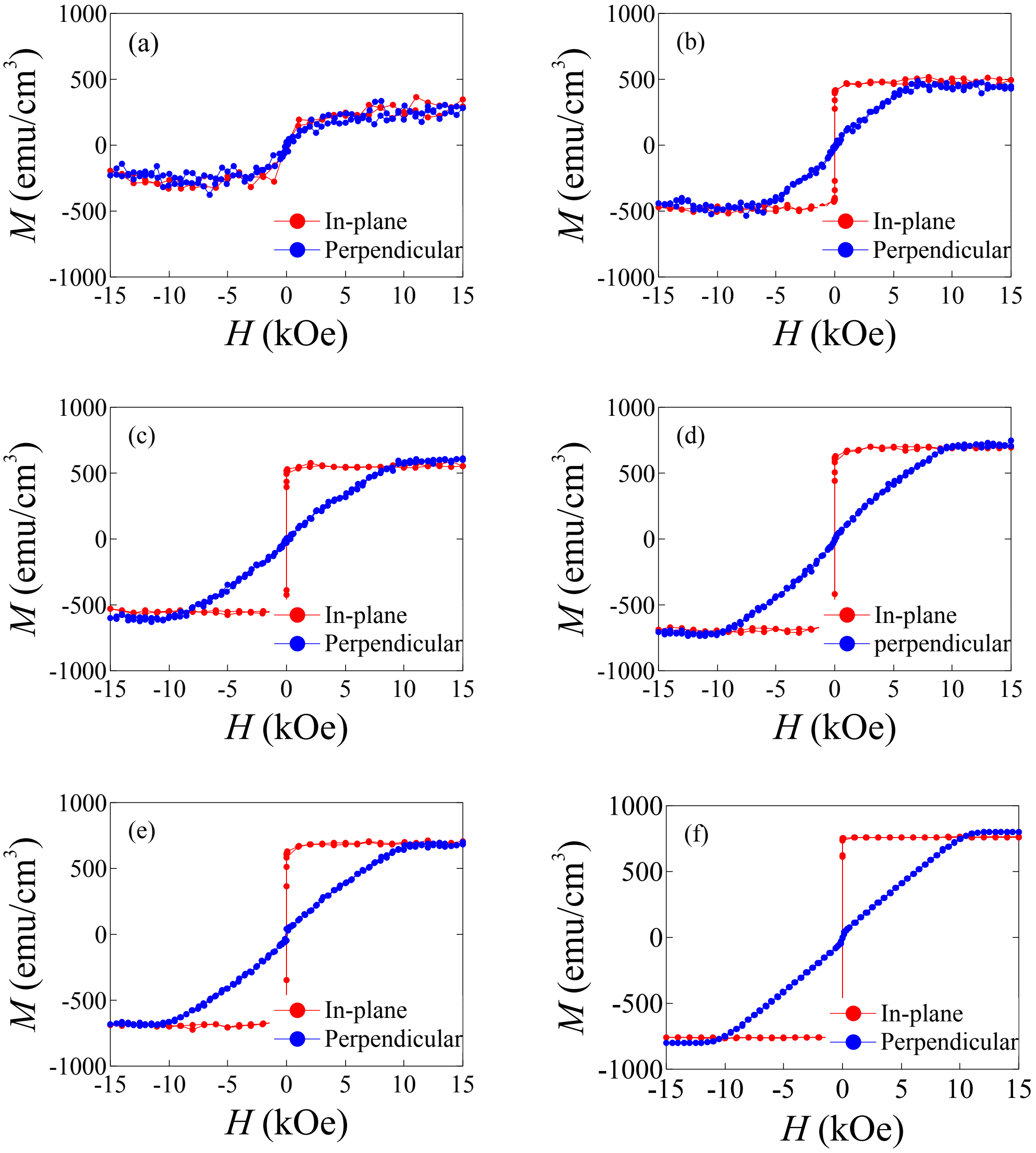

Figure 3.1.1 (a-e) hysteresis loops for Ta/Py/Pt layer with the thickness of Py varied from 1-5 nm and (f) 82 nm, respectively.

### 3.2 Analysis of Saturation Magnetization in Ta/Py/Pt with Dead-Layer Model

Dead-layer model is a commonly used method for an analysis of saturation magnetization because it is well known that an interlayer mixing occurs at the interfaces during sputtering and annealing, and an actual thickness is different from a nominal thickness [1-12, 15]. The model also enables one to estimate a magnetically active thickness of each sample. If there is a finite thickness of a dead-layer, a magnetically active thickness of Py layers in this study is reduced by the thickness of a dead-layer. A dead-layer can be obtained by introducing $M_St$ as a function of $t$. The intersection of x-axis and the sloop correspond to dead-layer and saturation magnetization, respectively, shown in figure 3.2.1. The evaluated dead-layer and saturation magnetization is 0.63±0.09 nm and 768±2 emu/cc, respectively. Surprisingly, a linear function fully fit even in 1 nm region, which indicates that magnetization can survive even for 0.4 nm of an active thickness of Py. The data can support the validity to apply the dead-layer model into our films.

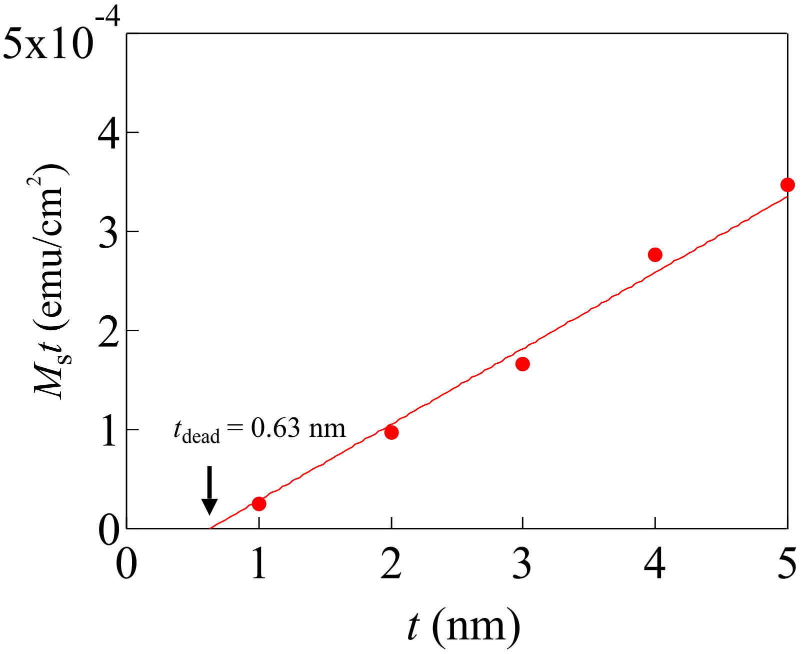

Figure 3.2.1 $M_st$ as a function of thickness of Py, which gives 0.63 nm of the dead layer.

### 3.3 Analysis of The Interface Perpendicular Magnetic Anisotropy by Using Dead-layer Model

PMA is quite important property of magnetic films because it enables us to fabricate perpendicularly magnetized films. Here, I calculated an interface PMA of Ta/Py /Pt with dead-layer model.

In order to evaluate PMA of the films, we introduce the magnetic anisotropy energy $K_{\mathrm{U}}$, $K_{\mathrm{U}}t = \frac{K_{\mathrm{V}}t}{2} + K_{\mathrm{i}}$, where $K_{\mathrm{V}}$ is bulk magnetic anisotropy energy and $K_{\mathrm{i}}$ is interface magnetic anisotropy energy, respectively. In fact, $K_{\mathrm{U}}$ can be calculated as $M_{\mathrm{S}}H_{\mathrm{K}}/2$,shape anisotropy. Here, $H_{\mathrm{K}}$ is denoted as a saturation magnetic field for a hard axis of the out-of-plane. At $t$ = 0.63 nm, the interface magnetic anisotropy energy can be estimated to be 0.17±0.04 erg/cm$^2$ in a dead layer model shown figure 3.3.1, which suggests that the interface magnetic anisotropy energy of Ta/Py/Pt is quite smaller than that of CoFeB/MgO and Fe/MgO [10,11]. Figure 3.3.2 show the saturation magnetizations as a function of the evaluated thickness with the dead-layer mode. The evaluated saturation magnetizations whose thickness less than 3 nm are almost as large as 700 emu/cm3, which suggests that the dead-layer model cannot demonstrate the magnetization distribution in the films because the evaluated saturation magnetization cannot recover up to the bulk one (760 emu/ cm$^3$)

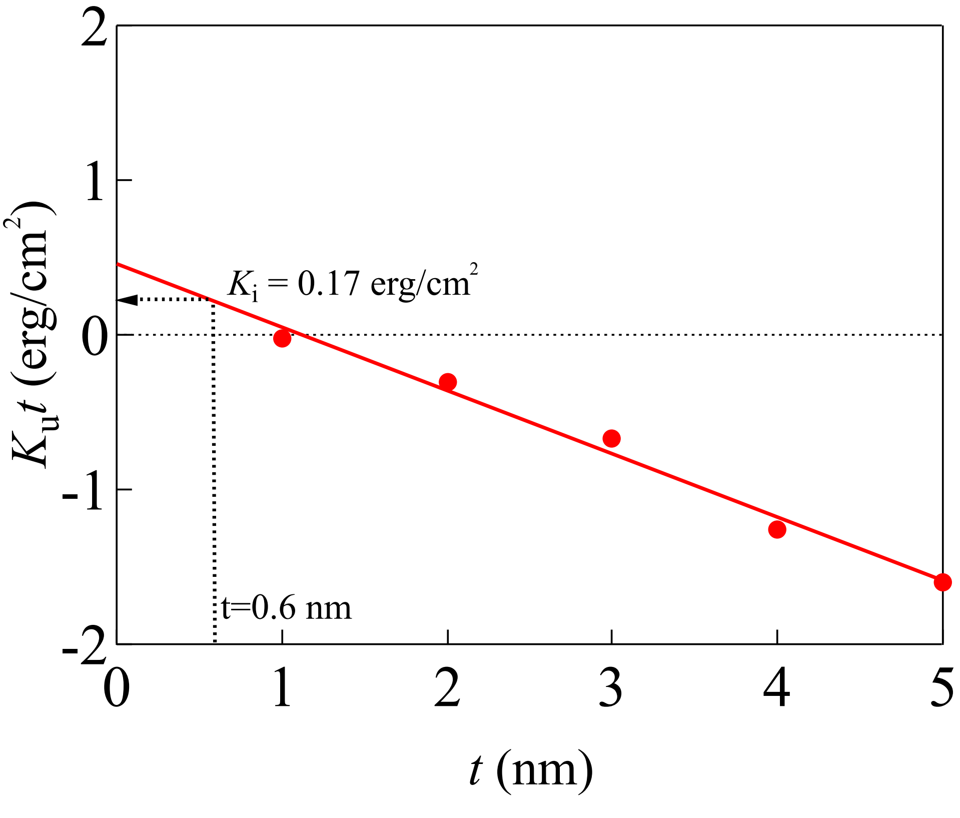

Figure 3.3.1 $K_{\mathrm{u}}t$ as a function of thickness of Py, determining interface PMA of the film.

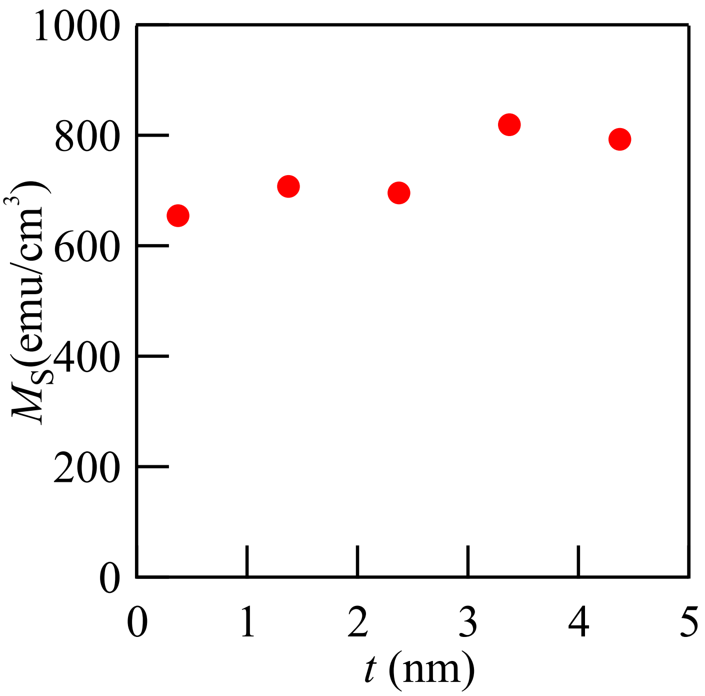

Figure 3.3.2 $M_S$ as a function of the thickness of Py in dead layer model.

### 3.4 Proposal of The Alternative Model to Evaluate Interface Perpendicular Magnetic Anisotropy

As descried in 3.2, the dead-layer model is widely used to investigate an active magnetic thickness of films of more precise. However, the dead-layer model fundamentally require to use different thick films which possess the same magnetic property because a linear fit function is utilized in the dead-layer model to evaluate a saturation magnetization, which indicates all films should possess the same saturation magnetization in a magnetically active thickness and a magnetic dead layer. Namely, the sample with 1 nm thick, active thickness is 0.4 nm, has $M_s$ as large as 768 emu/cc even though the corresponding thickness is two atomic layers. While films in this study can be successfully described by the dead-layer model, one might wonder why the dead-layer model is adaptable to this study. Therefore, we would like to propose another model to evaluate interface PMA of my films.

Why is another model proposed here? Because the obtained saturation magnetization $M_s$ and effective magnetization $M_{eff}$ are comparable in this study shown in figure 3.4.1. Here $M_{eff}$ is calculated as $M_{eff} = H_k/4\pi$. If it is possible to ignore any magnetic anisotropy (e.g. crystal anisotropy and interface anisotropy) except shape anisotropy, $M_{eff}$ becomes comparable to $M_S$. From the point of the view of alternative model, it is determined that Ta/Py /Pt trylayers in this study possess a zero interface PMA.

In order to explain a zero interface PMA in Ta/Py/Pt trylayers, we give two hypotheses and the cartoon based on the following hypotheses is depicted in figure 3.4.2:

(i) The whole Py layer may have really homogeneous magnetization $M_s$, i.e., no dead-layer and therefore $t = t_{act}$.

(ii) The observed decrease in $H_k$ may not be due to a combined effect of interface PMA and t-independent shape anisotropy given by $M_s^{act}$, but may be due to a possible reduction in $M_s$, i.e., a quite simple mechanism described as a t-dependent shape anisotropy of $M_s = H_k/4\pi$.

The hypotheses are plausible and does not require interface PMA. The phenomologically obtained $K_i$ is not genuine but could be originated in homogeneously diluted $M_s$ that consequently introduces the decreased $H_k$ and $K_i$ in ultra thin Py films.

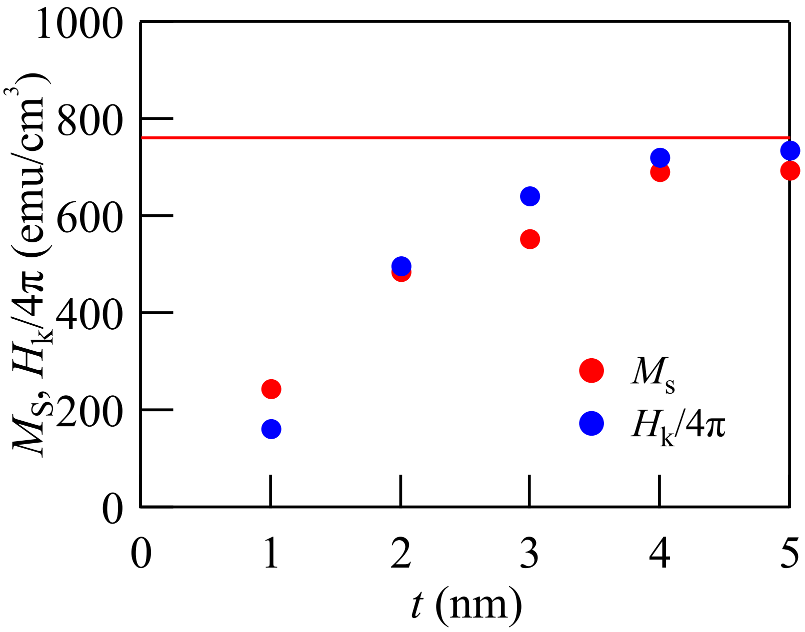

Figure 3.4.1 red and blue show Ms and Hk/4π as a function of the thickness of Py, respectively.

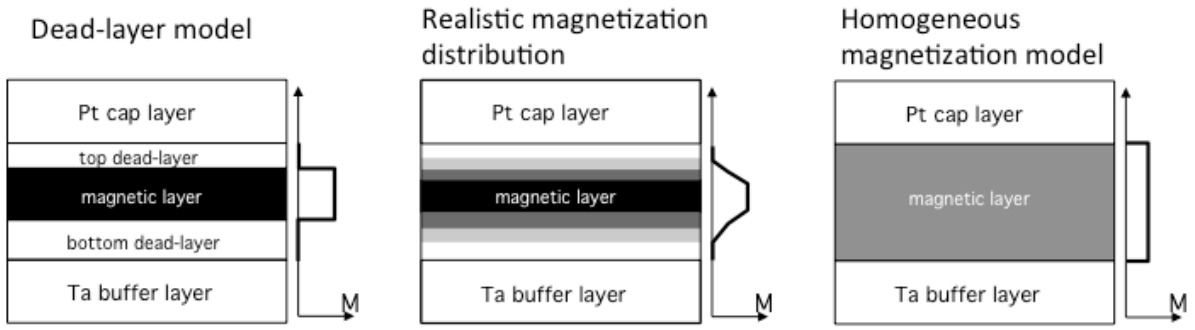

Figure 3.4.2 left and right schematic illustration show the dead-layer model and our proposed model, respectively.

### 3.5 Temperature Dependence of The Saturation Magnetizations in Ta/Py/Pt Films

In the section 3.4, we introduced an alternative model with the dead-layer model which is widely used to evaluate active magnetic layer and also $M_s$. In order to make sure that the model is practical to evaluate $M_s$ of an ultra thin film, we tried to examined temperature dependence of $M_s$ in Ta/Py (2nm)/Pt trylayer and how large thermal fluctuation influence to $M_s$ in ultra thin films because reduction of thermal fluctuation make $M_s$ recovered up to that of bulk according to Curie–Weiss law. Thus, Even in ultra thin Py, $M_s$ can be recovered up to 768 emu/cc if the alternative model can fully explain the reduction of $M_s$ and the consequently reduced $H_k$.

Figure 3.5.1 shows temperature dependence of $M_s$ in Ta/Py (2 nm)/Pt trylayer. The blue and yellow dashed line indicate that temperature dependence of saturation magnetizations in the case of the homogeneous magnetization model and ideal dead-layer model, respectively. It is found that the reduction of $M_s$ from low temperature to R.T. is around 30%. On the other hand, it is well known that the bulky $M_s$ of Py gives 5% reduction in the same temperature change [17]. Therefore the reduction by reducing the thickness of Py layer down to 2 nm thick corresponds to 25%. However, the observed reduction in a Ta/Py(2nm)/Pt film is ~35%, which suggests a thermal effect can not demonstrate the reduction of a saturation magnetization by thinning the thickness of Py.

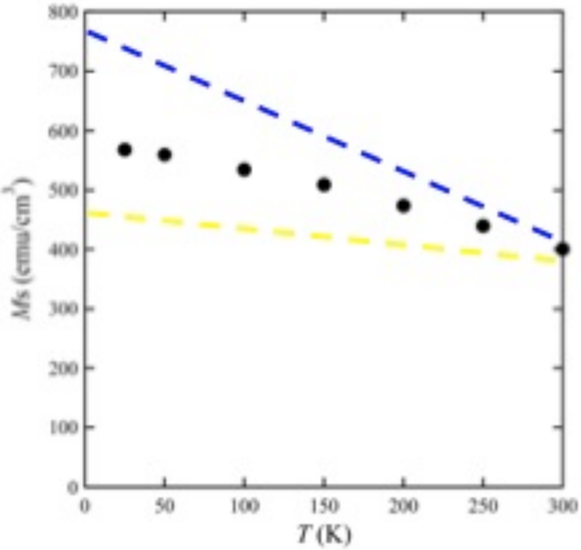

Figure 3.5.1 temperature dependence of $M_s$ in Ta/Py(2nm)/Pt

**3.6 Summary**

I investigated a saturation magnetization of Py and an interface perpendicular magnetic anisotropy in Ta/Py/Pt trilayer with various Py thicknesses. I observed that a saturation magnetization of Py decreases as decreasing the thickness of Py and a bulk sample, t=82nm, has 760 emu/cm$^3$. In dead-layer model, a dead-layer and an interface perpendicular magnetic anisotropy is evaluated to be 0.63 nm and 0.17 erg/cm$^2$, respectively. On the other hand, the alternative model gives zero interface perpendicular magnetic anisotropy because the saturation magnetization and the converted magnetization from a saturation magnetic field for a hard axis of out-of-plane direction are comparable. Temperature dependence of the saturation magnetization in Ta/Py (2 nm)/Pt suggests that the alternative model can not fully describe a reduction of saturation magnetization.

## Reference

[1] P. F. Carcia, A. D. Meinhaldt, and A. Suna.
Perpendicular magnetic anisotropy in Pd/Co thin film layered structures.
Appl. Phys. Lett. **47**, 178 (1985).

[2] F. J. A. den Broeder, W. Hoving, and P. J. H. Bloemen.
Magnetic anisotropy of multilayers.
J. Magn. Magn. Mater. **93**, 562 (1991).

[3] M. T. Johnson, P. J. H. Bloemen, F. J. A. den Broeder, and J. J. De Vries.
Magnetic anisotropy in metallic multilayers.
Rep. Prog. Phys. **59**, 1409 (1996).

[4] S. Monso, B. Rodmacq, S. Auffret, G. Casali, F. Fettar, B. Gilles, B. Dieny and P. Boyer,
Crossover from in-plane to perpendicular anisotropy in Pt/CoFe/AlOx
Pt/CoFe/AlOxsandwiches as a function of Al oxidation:
A very accurate control of the oxidation of tunnel barriers.
Appl. Phys. Lett. **80**, 4157 (2002).

[5] J. H. Jung, S. H. Lim, and S. R. Lee.
Strong perpendicular magnetic anisotropy in thick CoFeB films sandwiched by Pd and MgO layers.
Appl. Phys. Lett. **96**, 042503 (2010)

[6] S. Ikeda, K. Miura, H. Yamamoto, K. Mizunuma, H. D. Gan, M. Endo, S. Kanai,
J. Hayakawa,F. Matsukura, and H. Ohno.
A perpendicular-anisotropy CoFeB–MgO magnetic tunnel junction.
Nature Mater. **9**, 721-724 (2010).

[7] H. Sato, M. Yamanouchi, S. Ikeda, S. Fukami, F. Matsukura, and H. Ohno.
Perpendicular-anisotropy CoFeB-MgO magnetic tunnel junctions with
a MgO/CoFeB/Ta/CoFeB/MgO recording structure.
Appl. Phys. Lett. **101**, 022414 (2012).

[8] J. Sinha, M. Hayashi, A. Kent, S. Fukami, M. Yamanouchi, H. Sato, S. Ikeda,
S. Mitani, S. Yang, S. S. P. Parkin, and H. Ohno.
Enhanced interface perpendicular magnetic anisotropy in Ta|CoFeB|MgO using
nitrogen doped Ta underlayers.
Appl. Phys. Lett. **102**, 242405 (2013).

[9] Z. C. Wen, H. Sukegawa, S. Mitani, and K. Inomata.
Perpendicular magnetization of $Co_2FeAl$ full-Heusler alloy films induced by MgO interface.
Appl. Phys. Lett. **98**, 242507 (2011).

[10] Z. C. Wen, H. Sukegawa, T. Furubayashi, J. W. Koo, K. Inomata, S. Mitani, J. P. Hadorn, T. Ohkubo, and K. Hono.
A 4-Fold-Symmetry Hexagonal Ruthenium for Magnetic Heterostructures Exhibiting Enhanced Perpendicular Magnetic Anisotropy and Tunnel Magnetoresistance.
Adv. Mater. **26**, 6483 (2014).

[11] J. W. Koo, S. Mitani, T. T. Sasaki, H. Sukegawa, Z. C. Wen, T. Ohkubo, T. Niizeki, K. Inomata, and K. Hono.
Large perpendicular magnetic anisotropy at Fe/MgO interface.
Appl. Phys. Lett. **103**, 192401 (2013).

[12] M. S. Gabor, C. Tiusan, T. Petrisor, Jr. and, T. Petrisor.
The Influence of the Capping Layer on the Perpendicular Magnetic Anisotropy in Permalloy Thin Films.
IEEE Trans. Magn. **50**, 2007404 (2014).

[13] C. Slonczewski.
Current-driven excitation of magnetic multilayers.
J. Magn. Magn. Mater. **159**, 1 (1996).

[14] L. Berger.
Emission of spin waves by a magnetic multilayer traversed by a current.
Phys. Rev. B **54**, 9353–9358 (1996).

[15] S. Mizukami, Y. Ando, and T. Miyazaki.
The Study on Ferromagnetic Resonance Linewidth for NM/80NiFe/NM (NM=Cu, Ta, Pd and Pt) Films.
Jpn. J. Appl. Phys. 40, 580 (2001).

[16] K. Ounadjela, H. Lefakis, V.S. Speriosu, C. Hwang, and P.S. Alexopoulos.
Thickness Dependence of Magnetization and Magnetostriction of Py and NiFeRh films
J. de Phys. Collo **49**, C8-1709 (1988).

[17] J. Crangle, and G. C. Hallam.
The magnetization of face-centred cubic and body-centred cubic iron + nickel alloys.
Proc. Phys. Soc. A 272, 119 (1963).

[18] D. Odkhuu, S. H. Rhim, N. Park, and S. C. Hong
Extremely large perpendicular magnetic anisotropy of an Fe(001) surface capped by 5d transition metal monolayers: A density functional study
Phys. Rev. B **88**, 184405 (2013)

[19] H. X. Yang, M. Chshiev, B. Dieny, J. H. Lee, A. Manchon, and K. H. Shin

First-principles investigation of the very large perpendicular magnetic anisotropy at Fe|MgO and Co|MgO interfaces

Phys. Rev. B **84**, 054401 (2011)

## 4. Evaluation of Spin Hall angle in ST-FMR Measurement in Py/Pt Films at $\theta$ = 10° and 45°

This chapter describes ST-FMR in Py/Pt films at at $\theta = 10^{\circ}$ and 45°. The relative angle of $\theta = 45^{\circ}$ has been widely studied because the intensity of ST-FMR spectra is the largest. On the other hand, the relative angle of $\theta = 10^{\circ}$ has been rarely examined because of the weak amplitude of spectra. Therefore, it is important to systematically investigate ST-FMR spectra at $\theta$=10° and 45° with various direct current to establish the ST-FMR measurement on the relative angle. While two methods are employed to evaluated spin Hall angle: spectrum intensity ratio and effective damping modulation method, the spectrum intensity ratio gives anomalous modulation on the evaluated spin Hall angle at $\theta = 10^{\circ}$. On the other hand, the effective damping modulation method gives the evaluated spin Hall angle of 0.034, which suggests that the effective damping modulation method is more reliable than the spectrum intensity ratio method to evaluate the spin Hall angle in ST-FMR measurement [1-9].

### 4.1 Magnetic Properties in Py/Pt Films

I prepared the Py (5 nm)/Pt (8 nm) on a sapphire substrate by using a RF-magnetron sputtering system. The magnetic properties of the films are firstly investigated by using VSM. Figure 4.1.1 shows a hysteresis loop of Py (5 nm)/Pt (8 nm). The saturation magnetization $M_S$ is 576 emu/cm$^3$ and a demagnetizing filed $H_k$ is 7.9 kOe which correspond to 629 emu/cm$^3$, which is effective magnetization $M_{eff}$. The result revealed that the dead layer as thick as 0.4 nm exists while a converted magnetization from a demagnetizing field is larger than a saturation magnetization. Here, we follow the conclusion of section 3 in which an interface magnetic anisotropy is so small that the interface PMA at the interface of Py/Pt can be ignored. In this section, I applied the obtained values to ST-FMR analysis as follow, $M_s$ = 576 emu/cm$^3$, $M_{eff}$= 629 emu/cm$^3$. Note that the effective magnetization is in good agreement with the value obtained from ST-FMR measurement. Figure 4.1.2 shows a sample resistance with a parallel and perpendicular configuration of a current and an in-plane external magnetic field. The resistivities of Py and Pt in this study are 45 and 28 μΩcm, respectively. The AMR ratio is around 0.1% in our sample.

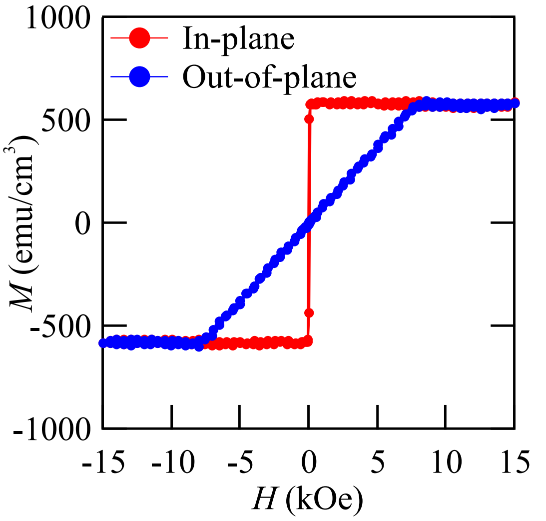

Figure 4.1.1 Saturation magnetization of Py in Py/Pt bilayer film

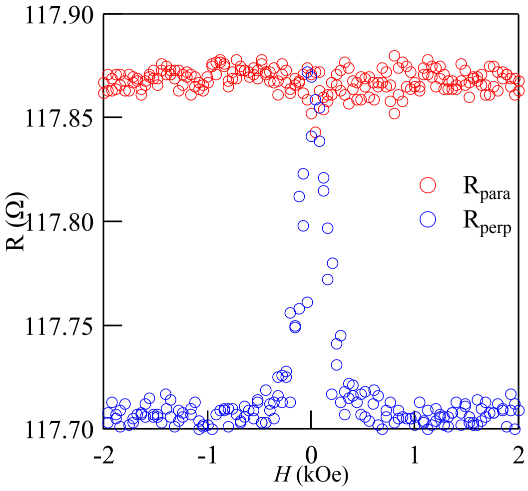

Figure 4.1.2 AMR effect in Py/Pt film

### 4.2 ST-FMR Spectra at $\theta$=45°

In previous reports, ST-FMR measurement at the relative angle has been widely studied because the ST-FMR spectra at the relative angle show one of the largest intensity of spectra. Figure 4.4.1 shows ST-FMR spectra at $\theta$=45° with various direction currents. The half width at half maximum (HWHM) is modulated by direct current described in section 1.9. the direct current dependence can be fully explained by the conventional understanding described in section 1.9.

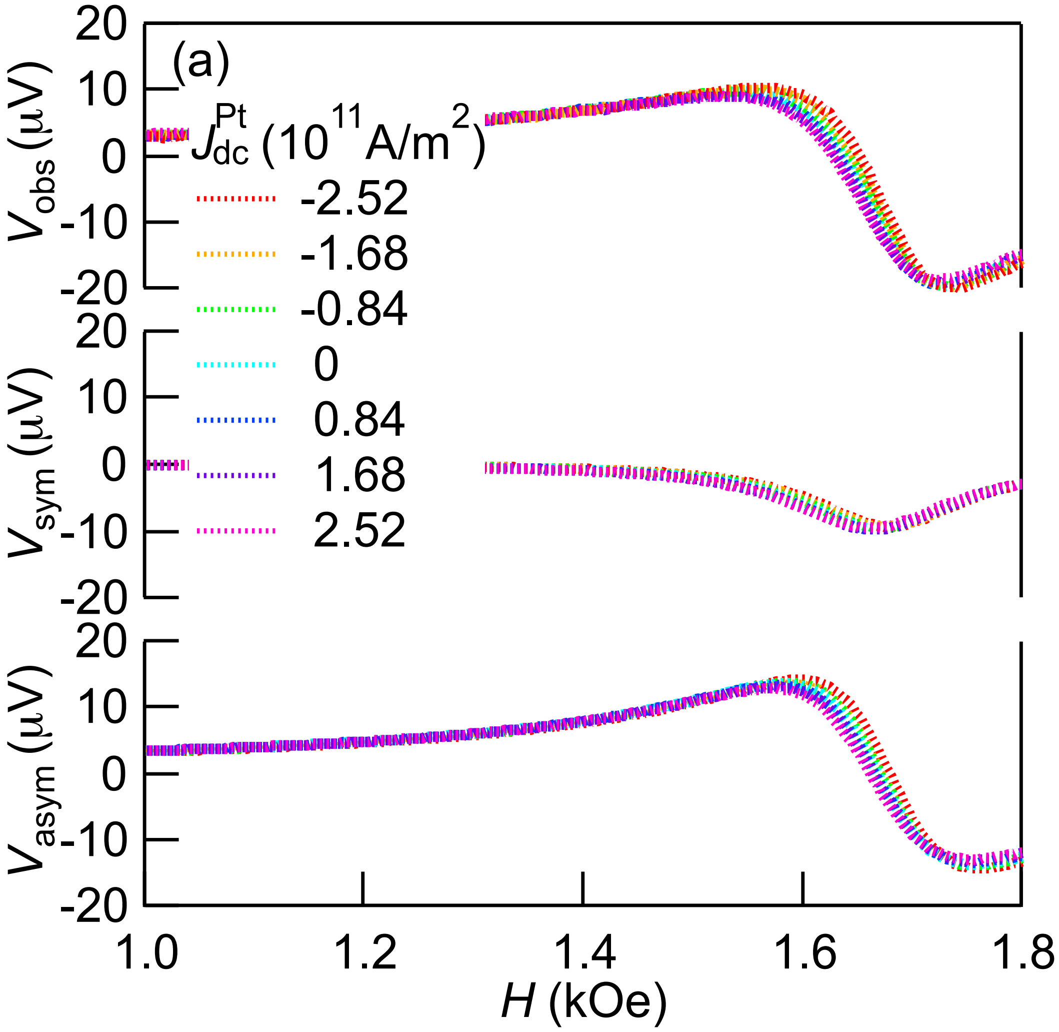

Figure 4.2.1 the observed, symmetric and asymmetric spectrum of the ST-FMR spectrum in Py/Pt films at $\theta$ = 45°

### 4.3 ST-FMR Spectra at *θ*=10˚

In a convectional framework, amplitude of ST-FMR spectra at $\theta = 10^\circ$ is small as written in equation. Therefore, little attention has been paid to at the angle. Figure 4.3.1 shows ST-FMR spectra at $\theta = 10^\circ$ with various direct currents. As is seen clearly, the observed spectrum $V_{\mathrm{obs}}$ is modulated by a direct current $I_{\mathrm{dc}}$ while a HWHM is poorly modified as expected in section 1.9. The modulation on the spectrum intensity cannot be described by the conventional framework based on the macro spin model on the ST-FMR written in the previous paper [1]. Seeing the symmetric component of ST-FMR spectra, it can be determined that the anomalous modulation is caused by the modulation of a symmetric component of ST-FMR spectra $V_{\mathrm{sym}}$ while asymmetric component of ST-FMR is poorly modulated on HWHM and an intensity.

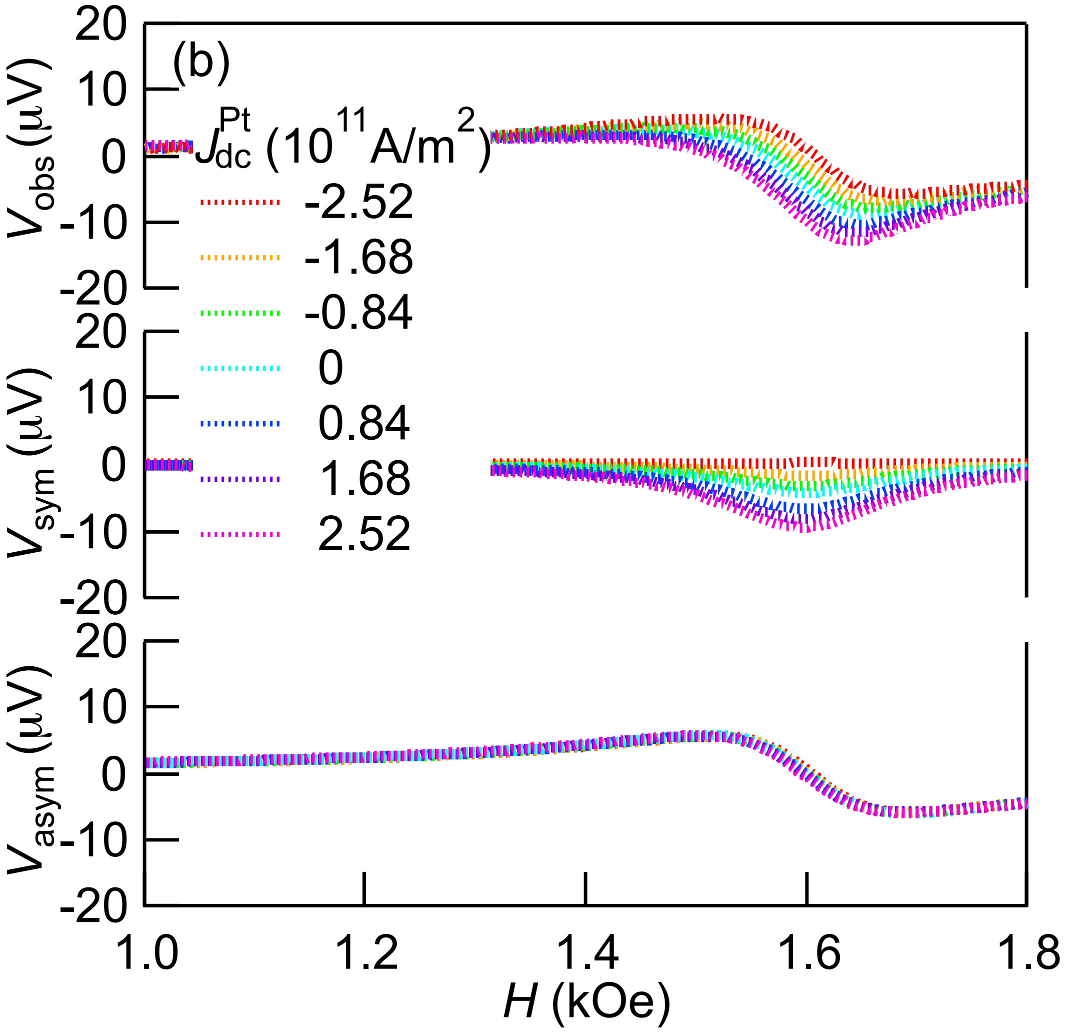

Figure 4.3.1 the observed, symmetric and asymmetric spectrum of the ST-FMR spectrum in Py/Pt films at $\theta = 10^\circ$

### 4.4 Evaluation of The Spin Hall Angles with Spectrum Intensity Ratio

Spin Hall angle can be evaluated with a spectrum intensity ration method and an effective damping modulation method as an introduction in section1.9. In this section I would like to evaluate spin Hall angle with a spectrum intensity ratio method.

Figure 4.4.1 shows the spin Hall angel $\eta_{\mathrm{SIR}}$ at $\theta = 10^{\circ}$ and $45^{\circ}$ evaluated by a spectrum intensity ratio method which is described in section 1.9. The obtained $\eta_{\mathrm{SIR}}$ at $\theta = 10^{\circ}$ is significantly modulated and the sign of $\eta_{\mathrm{SIM}}$ is changed as well by direct currents and the $\eta_{\mathrm{SIR}}$ is varied from -0.003 to 0.088. On the other hand, the obtained $\eta_{\mathrm{SIR}}$ at $\theta = 45^{\circ}$ maintains a constant value as much as 0.034 to direct currents.

In conventional framework, the evaluated spin Hall angle $\eta_{\mathrm{SIR}}$ shows a constant value and reported values are from 0.003 to 0.01.Therefore, $\eta_{\mathrm{SIR}}$ at $\theta = 45^{\circ}$ can be considered to be a reliable value and these results indicate that there problems exists in a spectrum intensity ratio method.

To know the anomalous modulation on the evaluated spin Hall angles, I checked the direct currents dependence of $kS$ and $kA$ shown in figure 4.4.2. There is no significant modulation for $\theta = 45°$. In contrast, the coefficient $kS$ clearly shows a linear dependence on direct currents in Pt at $\theta = 10°$, whereas only DC weak dependence is observed in the coefficient $kA$. The weak dependence of $kA$ guarantees that the prefactor $k$ is not modulated by the direct currents. However, intrinsically, $S$ does not have the direct currents in Pt dependence as defined to be $S = \frac{\hbar J_{\mathrm{rf}}^{\mathrm{FM}}}{2e\mu_0 M_{\mathrm{s}} t_{\mathrm{FM}}}$; thus, within the ST-FMR framework, additional excitation sources that are proportional to $J_{\mathrm{Pt}}J_{\mathrm{Pt}}$ characterized by rf currents and excite only the symmetric component are necessary. One possible origin is the tilting of the precession axis towards the perpendicular direction to films due to the spin Hall torque induced by direct currents, which provides a significant contribution at small θ values. However, the tilting angle estimated by the numerical calculation is too small to explain the aforementioned results shown in figure 4.4.3; a current density one to two order of magnitude larger is necessary. Another candidate is thermal effect such as the spin Seebeck effect due to the Joule heating effect which is proportional to direct currents flowing in Pt and the resulting time-dependent temperature gradient generated along the thickness direction. As is discussed later in next section, the thermal effects weakly influence to the anomalous modulation.

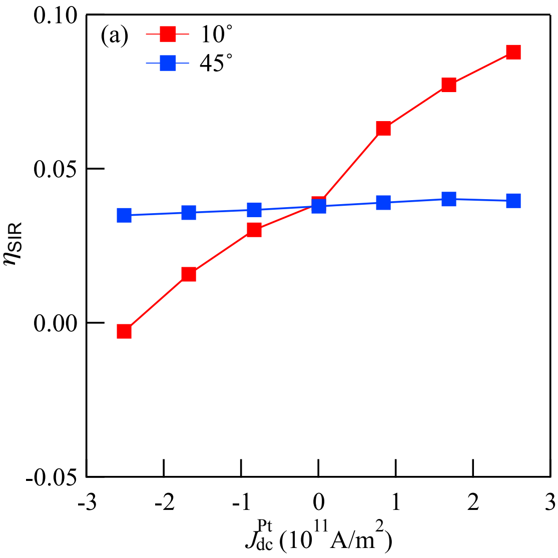

Figure 4.4.1 the evaluated spin Hall angle with spectrum intensity ratio method at θ=10 and 45˚.

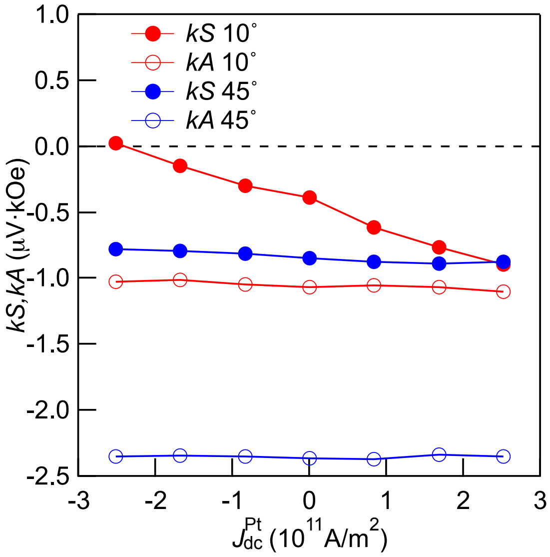

Figure 4.4.2 *kS* and *kA* as a function of direct current density in Pt at θ = 10˚ and 45˚

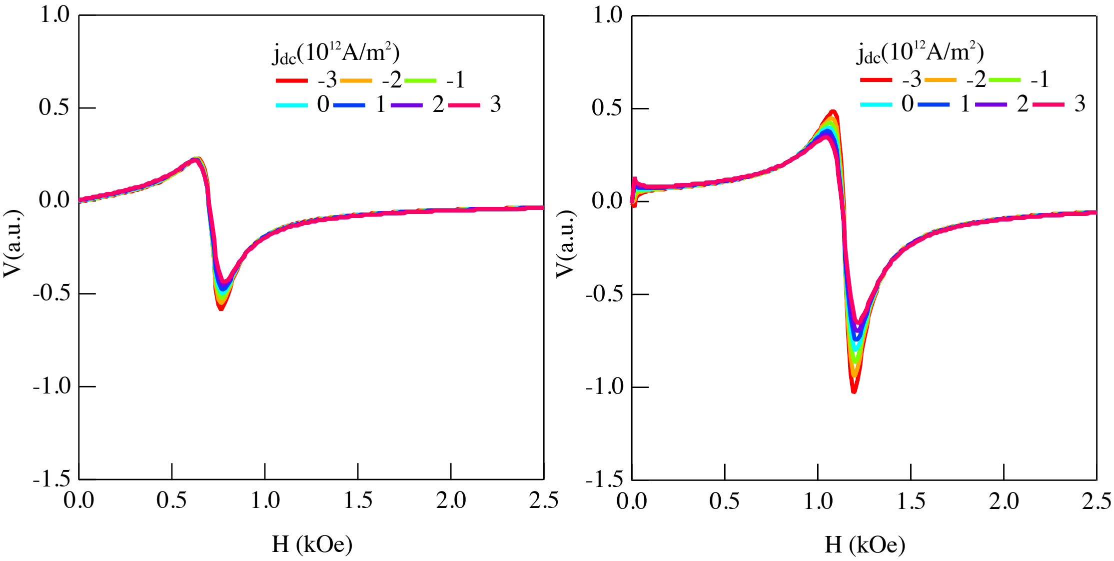

Figure 4.4.3 numerical simulations of ST-FMR with perpendicular magnetic field of (Left) 500Oe and (Right) 0 Oe induced by the tilting of the precession axis towards the perpendicular to films.

## 4.5 Evaluation of The Spin Hall Angles with Effective Damping Modulation

I would like to discuss the evaluation of spin Hall angle $\eta_{\mathrm{EDM}}$ with an effective damping modulation method [1, 3, 8, 10].

Figure 4.5.1 shows the effective damping modulation divided by a direct current flowing in Pt. following the equation $\eta_{\mathrm{EDM}} = \frac{(H_{\mathrm{ext}}+2\pi M_{\mathrm{eff}})\mu_0 M_{\mathrm{S}} t_{\mathrm{FM}}}{sin\theta}\frac{\Delta\alpha}{J_{\mathrm{DC}}^{\mathrm{HM}}}$, the function has sin$\theta$ dependence and the evaluated amplitude gives an evaluated spin Hall angle. The spin Hall angle $\eta_{\mathrm{EDM}}$ is eventually evaluated to be 0.034. In previous works, the spin Hall angle $\eta_{\mathrm{EDM}}$ is obtained around 0.05, which indicates the evaluated value in this study is reasonable compared to the previous reports.

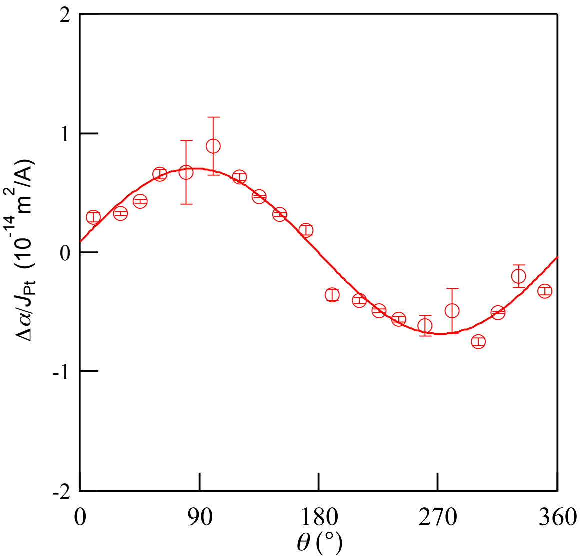

Figure 4.5.1 Damping modulation on the relative angle, indicating the evaluated spin Hall angel with the effective damping modulation method of 0.034.

## 4.6 Frequency Dependence of The Spin Hall angles Evaluated by Spectrum Intensity Ratio and Effective Damping Modulation

Figure 4.6.1 shows the ST-FMR spectra with various frequencies at the zero bias at θ =10˚ and 45˚. Fundamentally, ST-FMR spectra with lower frequency show the higher amplitudes because the amplitudes are inversely proportional to the resonant fields. However, the amplitudes seem to be unexpectedly independent on the frequency at both angles.

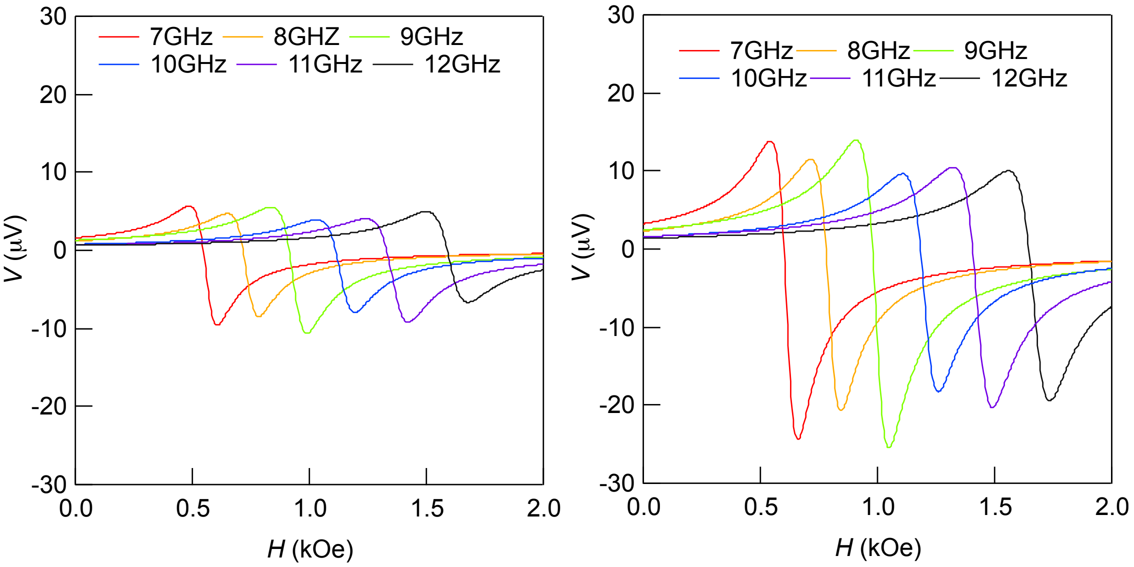

Figure 4.6.1 ST-FMR spectra with various frequency at (left) θ=10˚ and (Right) 45˚.

For further investigation on the amplitude problems, I checked the magnitude of ST-FMR spectra of asymmetric components $V_{PP}^{asym}$ and the applied frequency as a function of the resonant field shown in figure 4.6.2. As is clearly seen in figure 4.6.2, $V_{\mathrm{pp}}$ does not have an inversely linear function of the resonant field and the resonant field is well fitted to the Kittle function, which can suggest that the observed spectra on the amplitude are not wrong while they seem to be independent of the resonant fields.

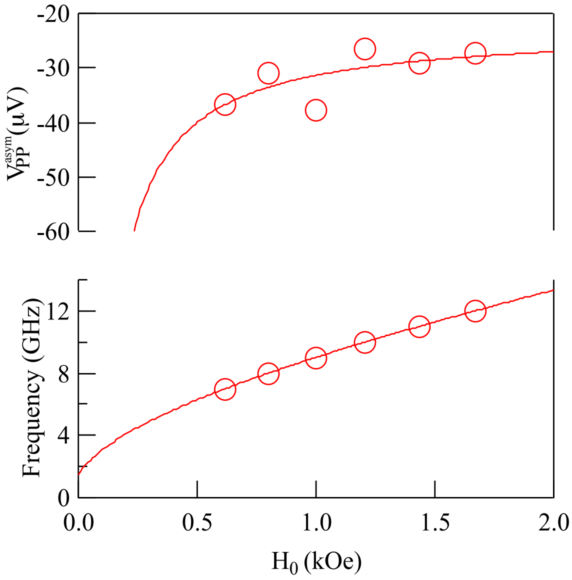

Figure 4.6.2 (Top) the magnitude of ST-FMR spectra of asymmetric components and (bottom) the applied frequency on the resonant field.

Figure 4.6.3 show the frequency dependence of the evaluated spin Hall angles by using SIR at $\theta =$ 10˚ and 45˚. While the spin Hall angles at the zero bias is almost the same value at any frequency, the magnitudes of the sloop on the evaluated spin Hall angles versus the applied direct currents increases with decreasing the frequency. The SIR at $\theta = 45˚$ shows the frequency dependence of the evaluated spin Hall angles. The evaluated spin Hall angles are independent of not only the applied direct currents but also the frequency.

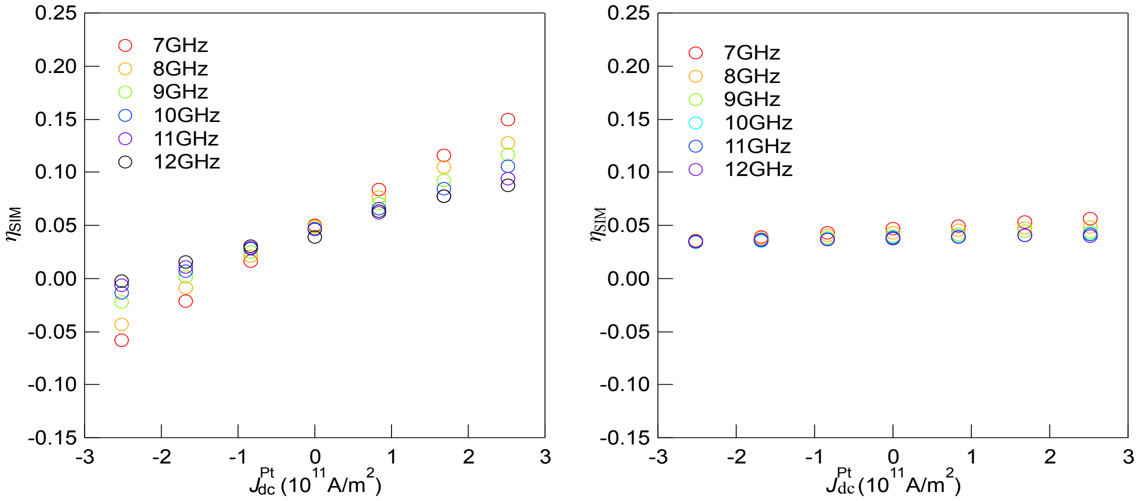

Figure 4.6.3 the spin Hall angles with various frequency at (Left) $\theta = 10$ °and (Right) 45°

To further understanding of the frequency dependence on the evaluated spin Hall angles at $\theta = 10°$, I checked *S*/*A* shown in figure 4.6.4, *kS*, and *kA* and compared the $\theta = 10°$ and 45° shown in figure 4.6.5. According to the equation $\eta_{SIR} = t_{\mathrm{FM}} d_{\mathrm{HM}} \frac{S}{A} \frac{e\mu_0 M_{\mathrm{S}}}{\hbar} \frac{2\pi f}{\gamma H_{\mathrm{ext}}}$, $\eta_{SIR}$ is proportional to the *S*/*A* so that *S*/*A* should have the same trend to $\eta_{SIR}$. In this study, the evaluated spin Hall angles and *S*/*A* have the same trend at each angle, which suggests that the obtained $\eta_{SIR}$ and S/A are reasonable. While the figure 4.4.2 show the *kS* and *kA* at 12GHz, *kS* and *kA* shown in figure 4.6.5 also show the same tendency demonstrated in figure 4.4.2., and they do not show the frequency dependence. *S* and *A* are denoted to be $S = \frac{\hbar J_{\mathrm{rf}}^{\mathrm{FM}}}{2e\mu_0 M_{\mathrm{s}} t_{\mathrm{FM}}}$ and $A = \frac{J_{\mathrm{rf}}^{\mathrm{HM}} d_{\mathrm{HM}}}{2} [1 + \frac{M_{\mathrm{eff}}}{H_{\mathrm{eff}}}]^{1/2}$ so that the S and A are independent of the frequency. Therefore, the evaluated *kS* and *kA* are reasonable.

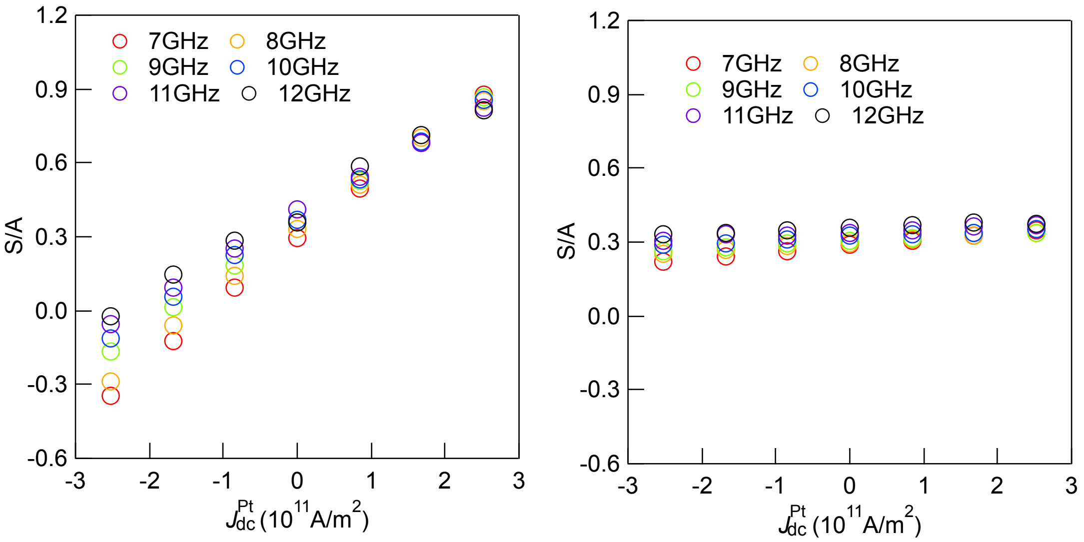

Figure 4.6.4 S/A on direct currents with various frequencies at (Left) θ = 10˚ and (Right) 45˚

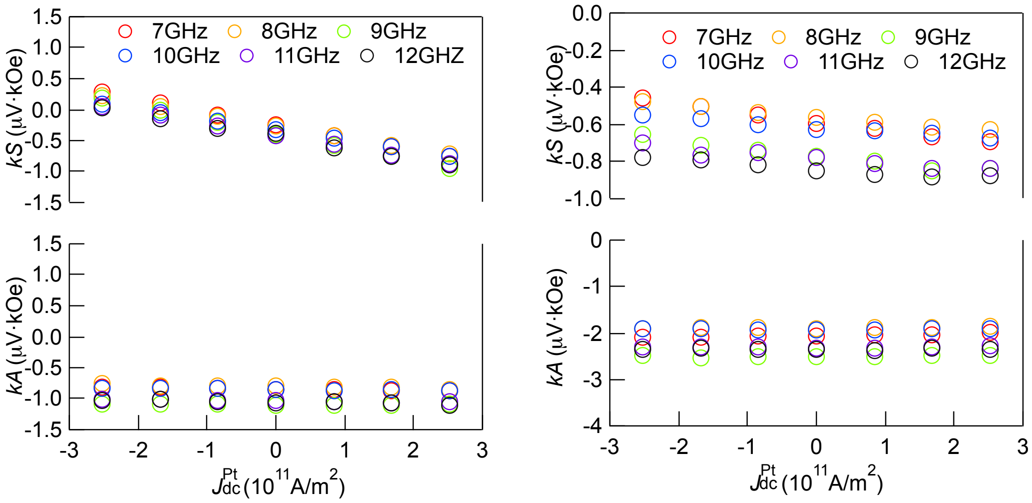

Figure 4.6.5 kS and kA on direct currents with various frequencies at (Left) θ = 10˚ and (Right) 45˚

### 4.7 Power Dependence of The Spin Hall Angle and The Related Parameters

I investigated the applied power dependence, and the applied powers were chosen to be -6, 0, and 6 dbm. Fundamentally, -6, 0, and 6 dbm correspond to 0.25, 1, and 4 mW, respectively. Figure 4.7.1 and 4.7.2 shows the power dependence of *S*/*A*, *kS* and *kA* at $\theta = 45^\circ$ and 10˚. *S*/*A* is independent of the applied power and linear dependence on the applied direct currents, which is consistent with the data mentioned in section 1.9. While *S*/*A* is independent on the applied power, *kS* and *kA* show the applied power dependence, which suggesting that *k* is dependent on the applied power because *k* is the prefactor on output voltages characterized by the sample resistance.

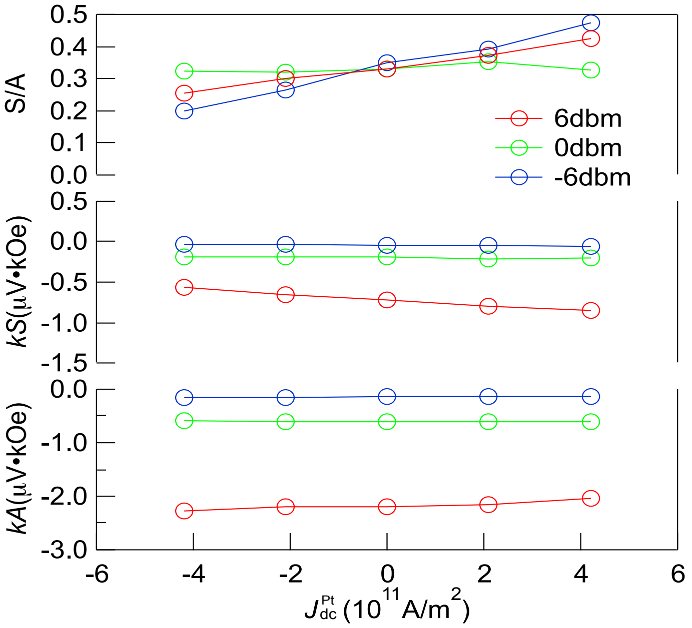

Figure 4.7.1 the power dependence of *S*/*A*, *kS* and *kA* at $\theta = 45^\circ$ in Py/Pt films on a sapphire substrate

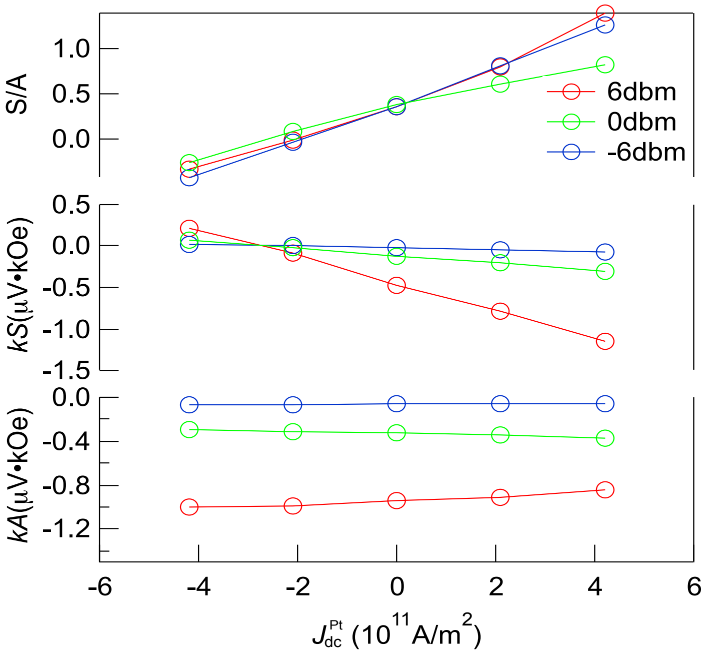

Figure 4.7.2 the power dependence of *S*/*A*, *kS* and *kA* at $\theta = 10^\circ$ in Py/Pt films on a sapphire substrate

### 4.8 Discussion

Figure 4.7.1 shows damping parameter of the Py/Pt films as a function of a relative angle. The obtained damping parameter keeps a constant value as much as 0.022 on the relative angle, which is consistent with the values in previous reports. In addition, figure 4.7.2 shows a resonant frequency as a function of resonant field, so-called the kittle formula. The curve is fitted well to the experimental data and the obtained effective magnetization is 7.9 kOe which is comparable to one of the VSM values shown in Figure 4.1.2. Therefore, it is possible to insist that the quality of the films in this study does not have any problem and the anomalous modulation to direct currents at $\theta = 10^\circ$ is a characteristic phenomenon in a ST-FMR measurement under direct currents. Moreover, the evaluated damping parameter can clarify that magnetization dynamics is not affected by direct currents even though the anomalous modulations on the intensity of symmetric component of ST- FME spectra are observed.

I would like to discuss two evaluation methods: spectrum intensity ratio and effective damping modulation because the spectrum intensity ratio method give relative angle dependence of spin Hall angle while the effective damping ratio method gives a constant value. Originally, the spin Hall angle of Pt should be constant with any methods because spin Hall angle is a physical constant. From the point of view, the effective damping modulation method is more reliable than the spectrum intensity ratio to evaluate spin Hall angle in ST-FMR method.

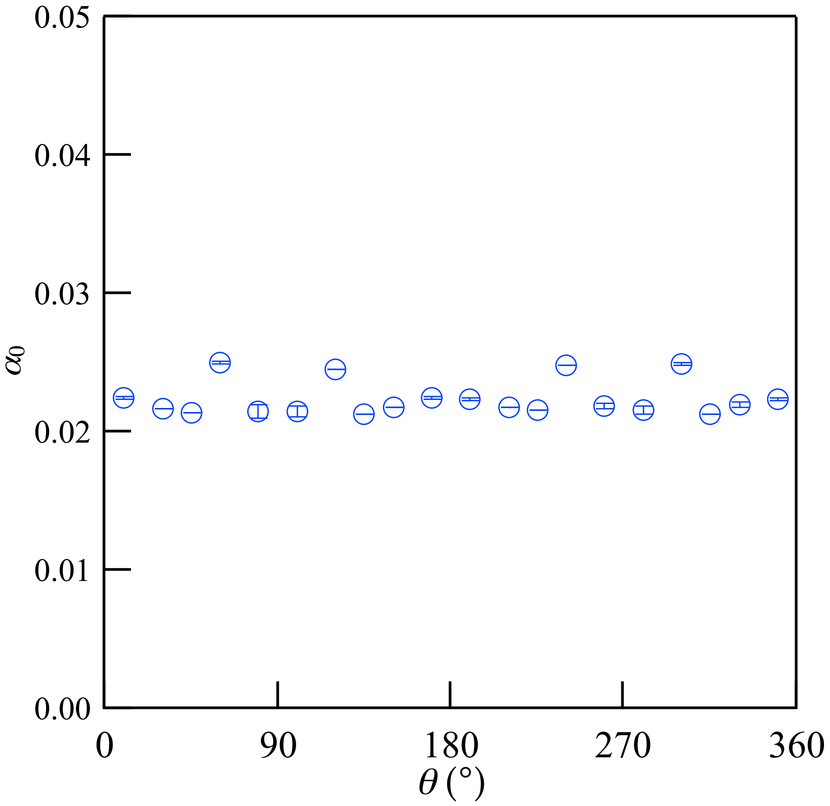

Figure 4.7.1 damping parameter on the relative angle

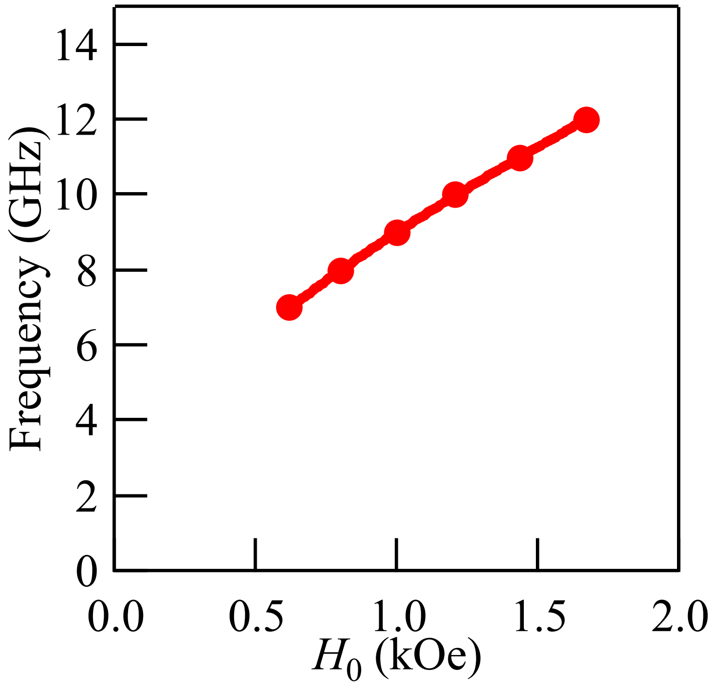

Figure 4.7.2 the resonant frequencies as a function of the resonant field at θ =45°

### 4.9 Summary

I investigated the spin Hall angle in Pt by using two methods: the spectrum intensity ratio and the effective damping modulation method. While data of VSM and kittle formula demonstrated that the Py does not have any problem to be examined, the anomalous modulation in a symmetric component in ST-FMR spectra to direct current is observed at $\theta = 10^\circ$. As a result of the anomalous modulation, the evaluated spin Hall angle in the spectrum intensity ratio method is varied from -0.003 to 0.088 while the effective damping modulation method provides the spin Hall angle of 0.034.Therefore, the effective damping modulation method is more reliable than the spectrum intensity ratio method and there may be undiscussed phenomena in the conventional framework of ST-FMR in respect of the intensity of ST-FMR.

## Reference

[1] L. Liu, T. Moriyama, D. C. Ralph, and R. A. Buhrman.
Spin-Torque Ferromagnetic Resonance Induced by the Spin Hall Effect.
Phys. Rev. Lett. **106**, 036601 (2011).

[2] K. Kondou, H. Sukegawa, S. Mitani, K. Tsukagoshi, and S. Kasai.
Evaluation of Spin Hall Angle and Spin Diffusion Length by Using Spin Current-Induced Ferromagnetic Resonance.
Appl. Phys. Express **5**, 073002 (2012).

[3] S. Kasai, K. Kondou, H. Sukegawa, S. Mitani, K. Tsukagoshi, and Y. Otani.
Modulation of effective damping constant using spin Hall effect.
Appl. Phys. Lett. **104**, 092408 (2014).

[4] K. Kondou, H. Sukegawa, S. Kasai, S. Mitani, Y. Niimi, and Y. Otani,
Influence of inverse spin Hall effect in spin-torque ferromagnetic resonance measurements.
Appl. Phys. Express **9**, 023002 (2016).

[5] J.-C. Rojas-Sánchez, N. Reyren, P. Laczkowski, W. Savero, J.-P. Attané, C. Deranlot, M. Jamet, J.-M. George, L. Vila, and H. Jaffrès.
Spin Pumping and Inverse Spin Hall Effect in Platinum: The Essential Role of Spin-Memory Loss at Metallic Interfaces.
Phys. Rev. Lett. **112**, 106602 (2014).

[6] Y. Wang, P. Deorani, X. Qiu, J. H. Kwon, and H. Yang.
Determination of intrinsic spin Hall angle in Pt.
Appl. Phys. Lett. **105**, 152412 (2014).

[7] W. Zhang, W. Han, X. Jiang, S. Yang, and S. S. P. Parkin.
Role of transparency of platinum–ferromagnet interfaces in determining the intrinsic magnitude of the spin Hall effect.
Nat. Phys. **11**, 496 (2015).

[8] A. Ganguly, K. Kondou, H. Sukegawa, S. Mitani, S. Kasai, Y. Niimi, Y. Otani, and A. Barman
Thickness dependence of spin torque ferromagnetic resonance in $Co_{75}Fe_{25}$/Pt bilayer films
Appl. Phys. Lett. **104**, 072405 (2014)

[9] T. X. Nan , S. Emori , C. T. Boone , X. J. Wang , T. M. Oxholm , J. G. Jones , B. M. Howe , G. J. Brown , and N. X. Sun
Comparison of spin-orbit torques and spin pumping across NiFe/Pt and NiFe/Cu/Pt interfaces
Phys. Rev. B **91**, 214416 (2015)

[10] K. Ando, S. Takahashi, K. Harii, K. Sasage, J. Ieda, S. Maekawa, and E. Saitoh.

Electric Manipulation of Spin Relaxation Using the Spin Hall Effect.
Phys. Rev. Lett. **101**, 036601 (2008).

## 5 Analyses for The Anomalous Modulation of ST-FMR Spectrum in Py/Pt Films

In the chapter 4, I introduced the anomalous modulation of a symmetric component of ST-FMR spectra in Py/Pt films [1-8]. The modulation makes it difficult to evaluate the spin Hall angle by using the spectrum intensity ratio method. Therefore, it is worth investigating the origin of the modulation in a symmetric component to evaluate the reliable spin Hall angle. In this chapter, I would like to show the results of direct current dependences of a symmetric and an asymmetric component that are expanded with polynomial function. These polynomial functions reveal that the anomalous modulation in a symmetric component in ST-FMR spectra is characterized by the first harmonics of the polynomial function of a symmetric component, which might be able to be described by AMR-induced photoresistance-like effect [9-11]. Note that the device and experimental set-up are shown in Figure 2.4.5 and 2.4.8, respectively.

### 5.1 Analysis with Polynomial Expansion of ST-FMR Spectra

Figure 5.1.1 show the direct current dependence of $kS$ and $kA$ on the relative angle. The $kS$ and $kA$ show the $\sin 2\theta\cos\theta$ dependence on the relative angle θ, which is demonstrated by conventional understanding. By changing the magnitude of direct currents, the magnitude of $kS$ also changes especially in the regions of 0˚ ~ 30˚, 150˚ ~ 210˚, and 330˚ ~ 360˚ while the magnitudes of $kA$ poorly changes by changing the magnitude of direct currents. This results demonstrated that the anomalous modulation in a symmetric component and no modulation in an asymmetric component of ST-FMR spectra to direct current shown in the chapter 4.1 are not limitedly observed at θ = 10˚. In this section, I introduce a polynomial expansion to analyze the anomalous modulation of ST-FMR spectra as follows:

$kS = kS_0 + kS_1 I + kS_2 I^2, kA = kA_0 + kA_1 I + kA_2 I^2$ (Eq. 5.1.1),

here $kS_0$ and $kA_0$ is the coefficient characterized by the excitation of rf-current, $kS_1$ and $kA_1$ is a coefficient of the first harmonics on direct currents, and $kS_2$ and $kA_2$ is a coefficient of the second harmonics on direct currents, respectively.

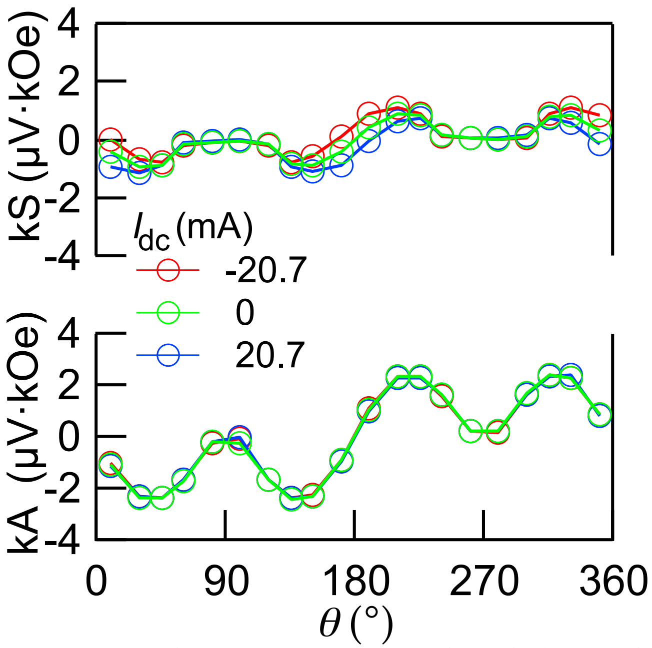

Figure 5.1.1 $kS$ and $kA$ as a function of the relative angle with various direct currents.

Figure 5.1.2 shows in-plane relative angle dependence of the expanded elements of (a) $kS_0$, (b) $kS_1$, (c) $kS_2$, (d) $kA_0$, (e) $kA_1$ and (f) $kA_2$, respectively. $kS_0$ and $kA_0$ shows the sin2$\theta$cos$\theta$ dependence that can be described by the convectional framework because the $kS_0$ and $kA_0$ are characterized by an excitation by rf-current. It is impossible, however, to explain why the $kS_1$ has angle dependence with a conventional framework in spite of the poor signal in $kA_1$. Higher order elements, $kS_2$ and $kA_2$, do not show clear angle dependence. While further investigations are required, the results described that the anomalous modulation in ST-FMR spectra is characterized by $kS_1$, namely, which is a linear modulation of only symmetric component in respect of direct currents.

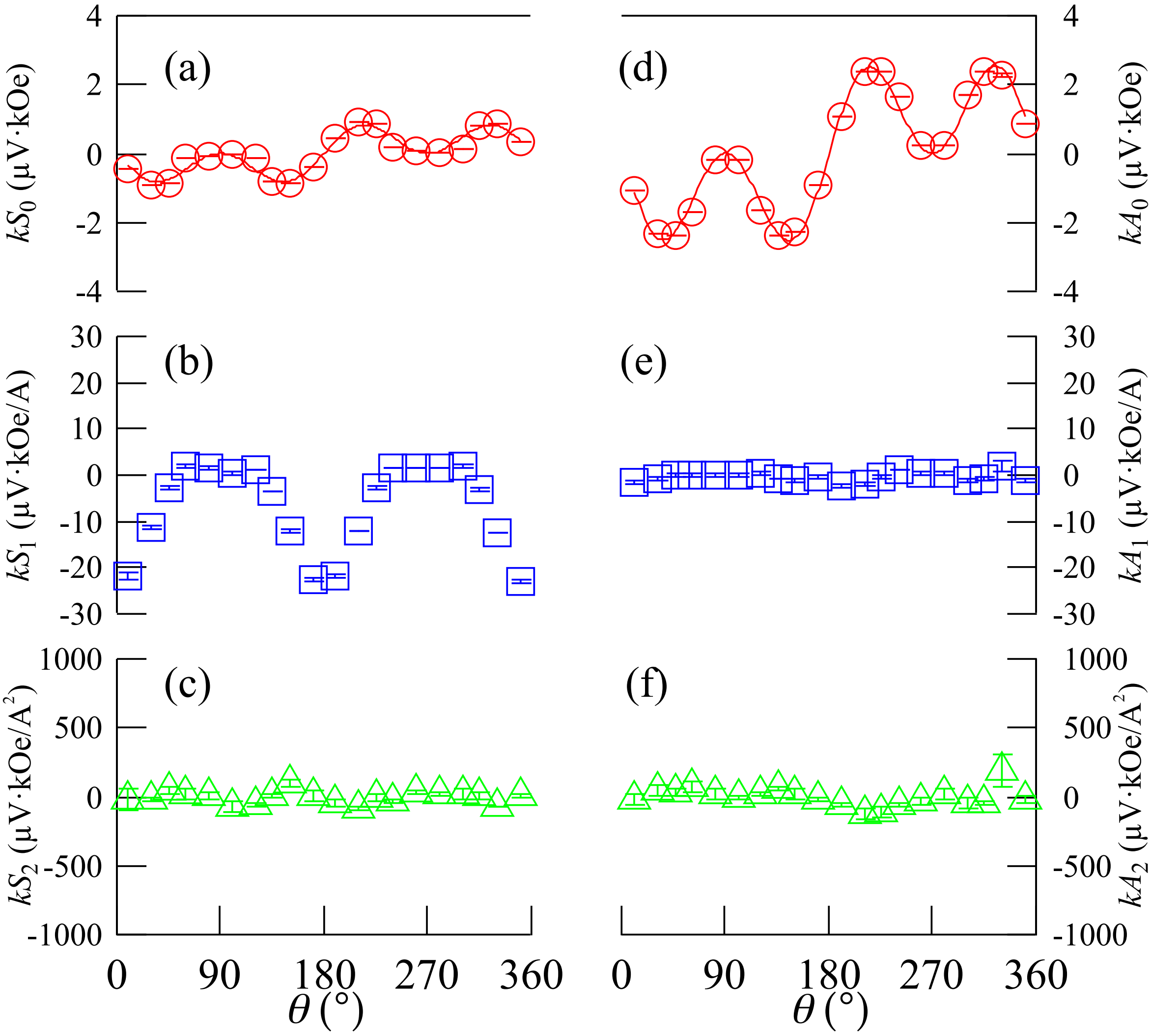

Figure 5.1.2 the expanded elements in the polynomial equation

### 5.2 Width dependence of The Expanded Components in Py/Pt Films

As is discussed in the section 1.10, the width of deveice in FM/HM is critical for development of the device application on the spin Hall auto oscillator. The device is operated by direct currents flowing the device, which suggests that the DC effect may influence to the operation of auto oscillator. Therefore, the width dependence of the expanded component is important to be examined.

Figure 5.2.1-3 show the expanded elements of $kS$ and $kA$ at the width = 1.0, 0.6, and 0.2 nm, respectively. Note that the data shown in figure 5.2.1 should be the same as those in figure 5.1.1. However, values are different because I used a different prober that caused the change of the contact resistance and consequently the change of $k$. Each device has each impedance matching so that it is impossible to directly compare the values, which means that the parameter k should be deleted. Namely, to compare the $kS_1$, $kS_2$, $kA_1$, and $kA_2$ of the three devices, they are normalized by $kS_0$ or $kA_0$.

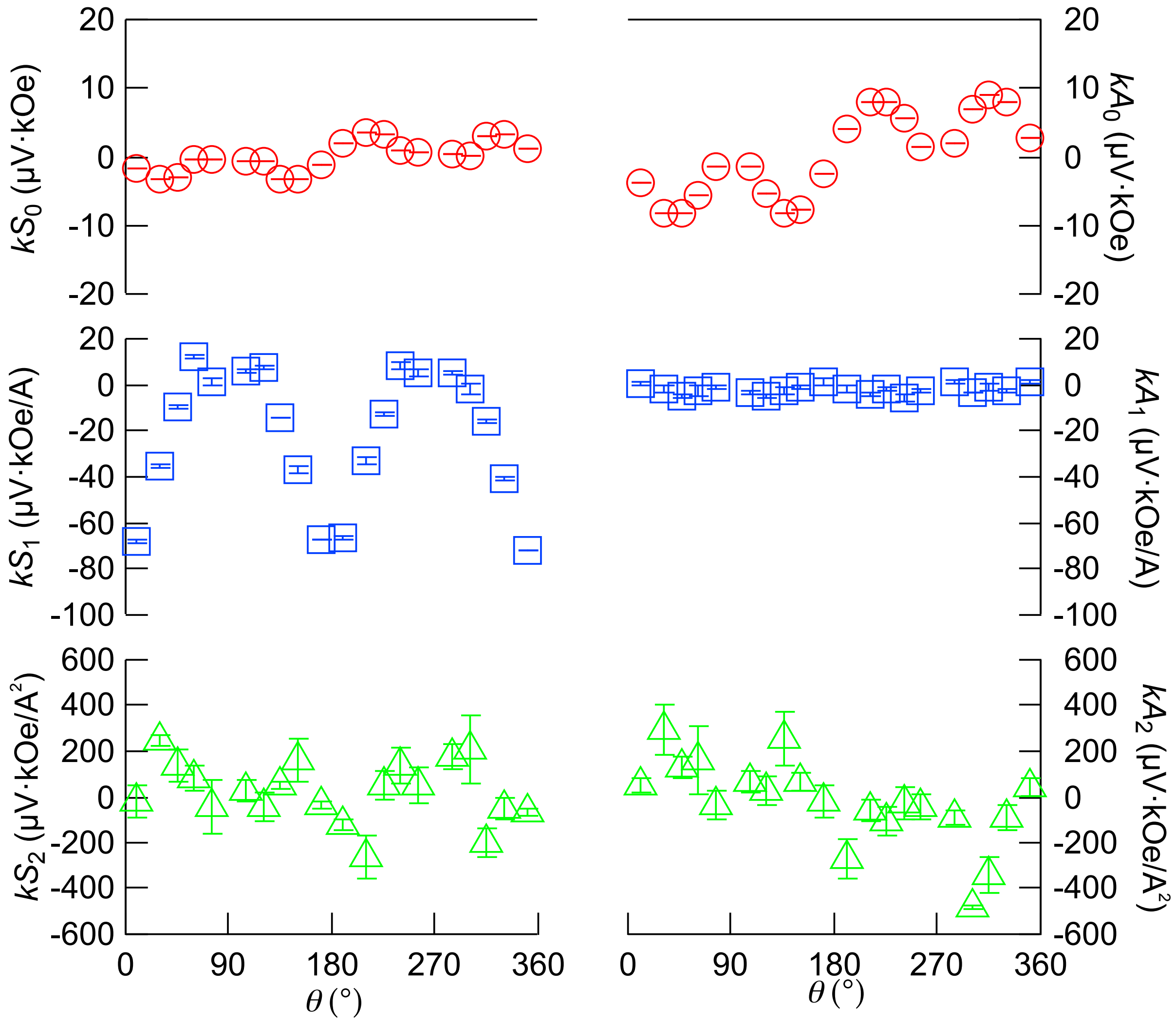

Figure 5.2.1 the expanded elements in the polynomial equation in the Py/Pt films with 1μm width.

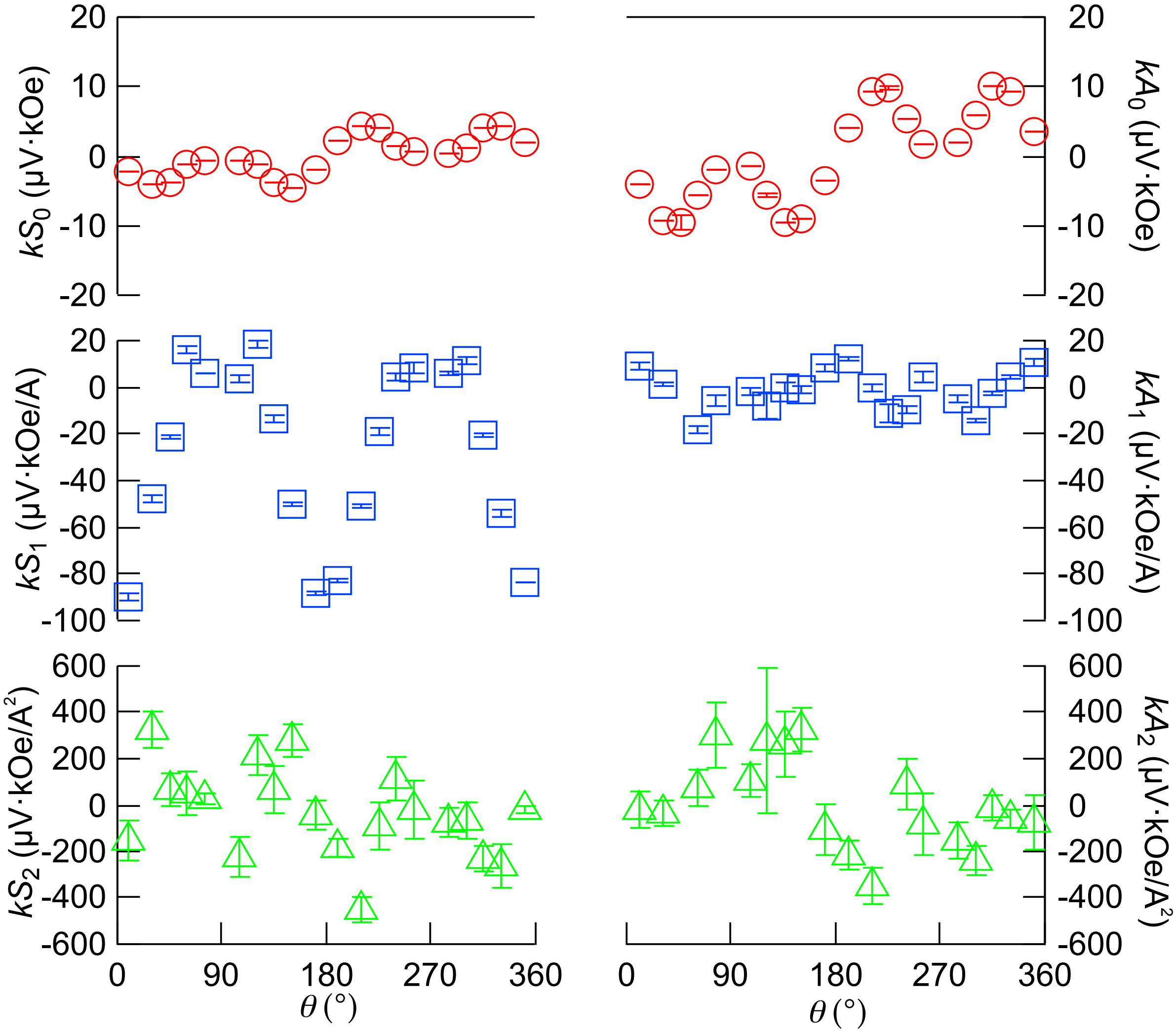

Figure 5.2.2 the expanded elements in the polynomial equation in the Py/Pt films with 0.6μm width.

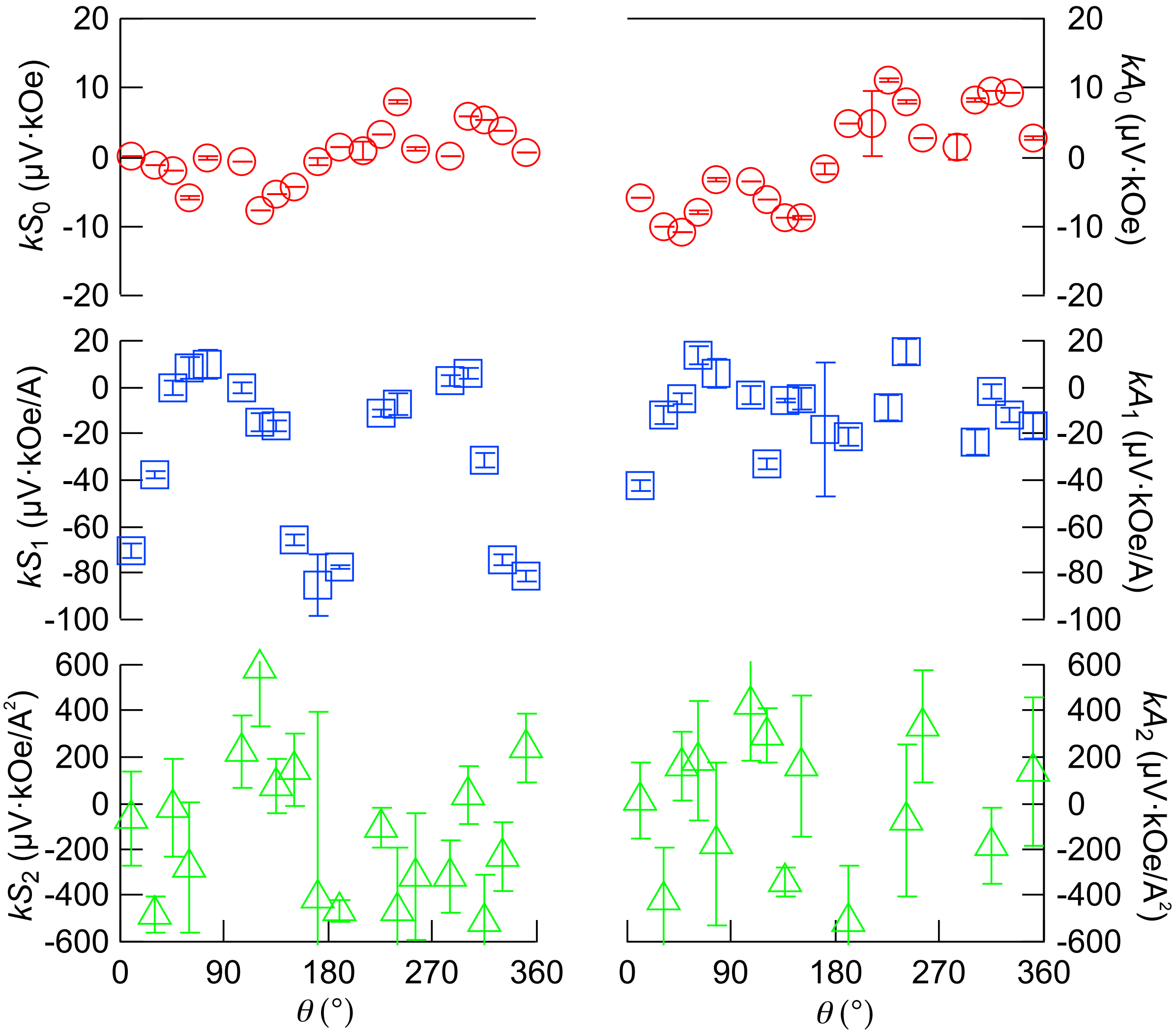

Figure 5.2.3 the expanded elements in the polynomial equation in the Py/Pt films with 0.2 μm width.

Figure 5.2.4 and 5.2.5 show the $kS_1/kS_0$, $kS_2/kS_0$, $kA_1/kA_0$, and $kA_2/kA_0$, respectively. Obviously, every normalized parameter does not show the width dependence on the relative angle $\theta$, which indicates that the observed anomalous modulation on the amplitudes in the symmetric components of ST-FMR spectra is not affected by the width of the device.

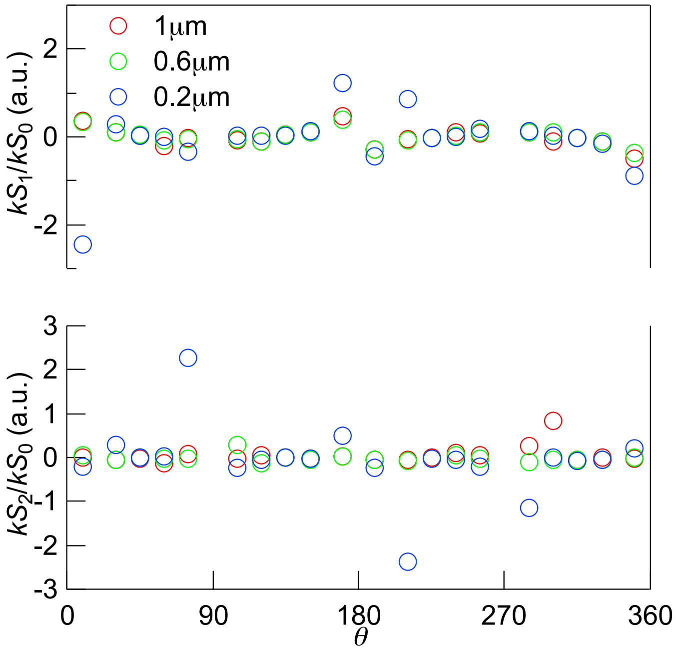

Figure 5.2.4 the $kS_1$ and $kS_2$ normalized by $kS_0$.

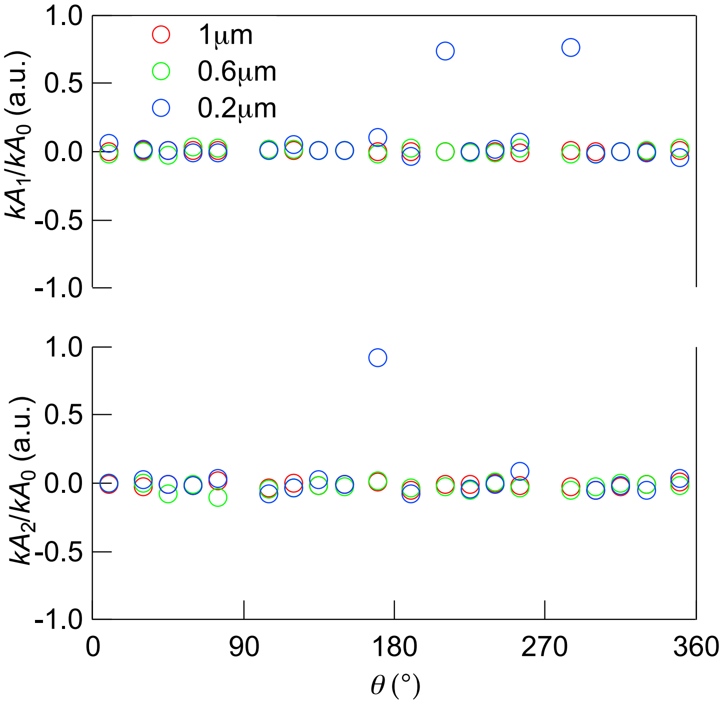

Figure 5.2.5 the $kA_1$ and $kA_2$ normalized by $kA_0$

### 5.3 **Investigation of Influence from Thermal Flow Accompanying Spin Transfer Torque**

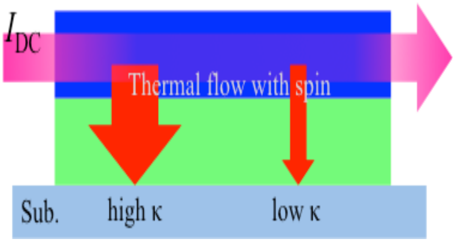

Figure 5.3.1 The schematic illustration of effects of thermal flows in the films

In a previous section, I introduced that direct currents induce the anomalous modulation in symmetric component in ST-FMR spectra. It is worth considering that direct currents flowing in Pt layer provide an unexpected spin transfer torque. A thermal flow accompanying spin transfer torque generated in Pt due to direct currents is one of the candidates to characterize $kS_1$ because it is well known that thermal flow accompany a spin transfer torque, e.g. spin Seebeck effect and spin Peltier effect [12-16]. Moreover, the Joule heating in Pt due to an applied current can be written with a following equation, $W \propto \left(J_{\mathrm{rf}}^{\mathrm{Pt}} + J_{\mathrm{dc}}^{\mathrm{Pt}}\right)^2$. The equation has a term including $J_{\mathrm{rf}} J_{\mathrm{dc}}$ which satisfies the requirement to be detected via rectification effect as described in section 1.6.

Therefore, in this section, I prepare the devices on both a sapphire and a thermally oxidized non-doped Si substrate to tune the magnitude of a thermal flow from Pt into Py by changing a substrate. The thermal conductivity of a sapphire and thermally non-doped Si substrate is 23.0 and 1.5W/mK, respectively. Figure 5.3.1 shows the schematic illustration on the thermal flows in the films. The expected $kS_1$ in devices on a thermally oxidized non-doped Si substrate is lower than that on a sapphire substrate because a magnitude of a thermal flow is considered to be reduced by reducing the thermal conductivity of a used substrate. Figure 5.3.2 shows the in-plane relative angle dependence of the expanded elements of (a) $kS_0$, (b) $kS_1$, (c) $kS_2$, (d) $kA_0$, (e) $kA_1$ and (f) $kA_2$ on a thermally oxidized non-doped Si substrate, respectively. However, every component shows the similar dependence and amplitude compared to that on a sapphire substrate, which demonstrate that thermal flow accompanying spin transfer torque generated in Pt gives less influence to $kS_1$.

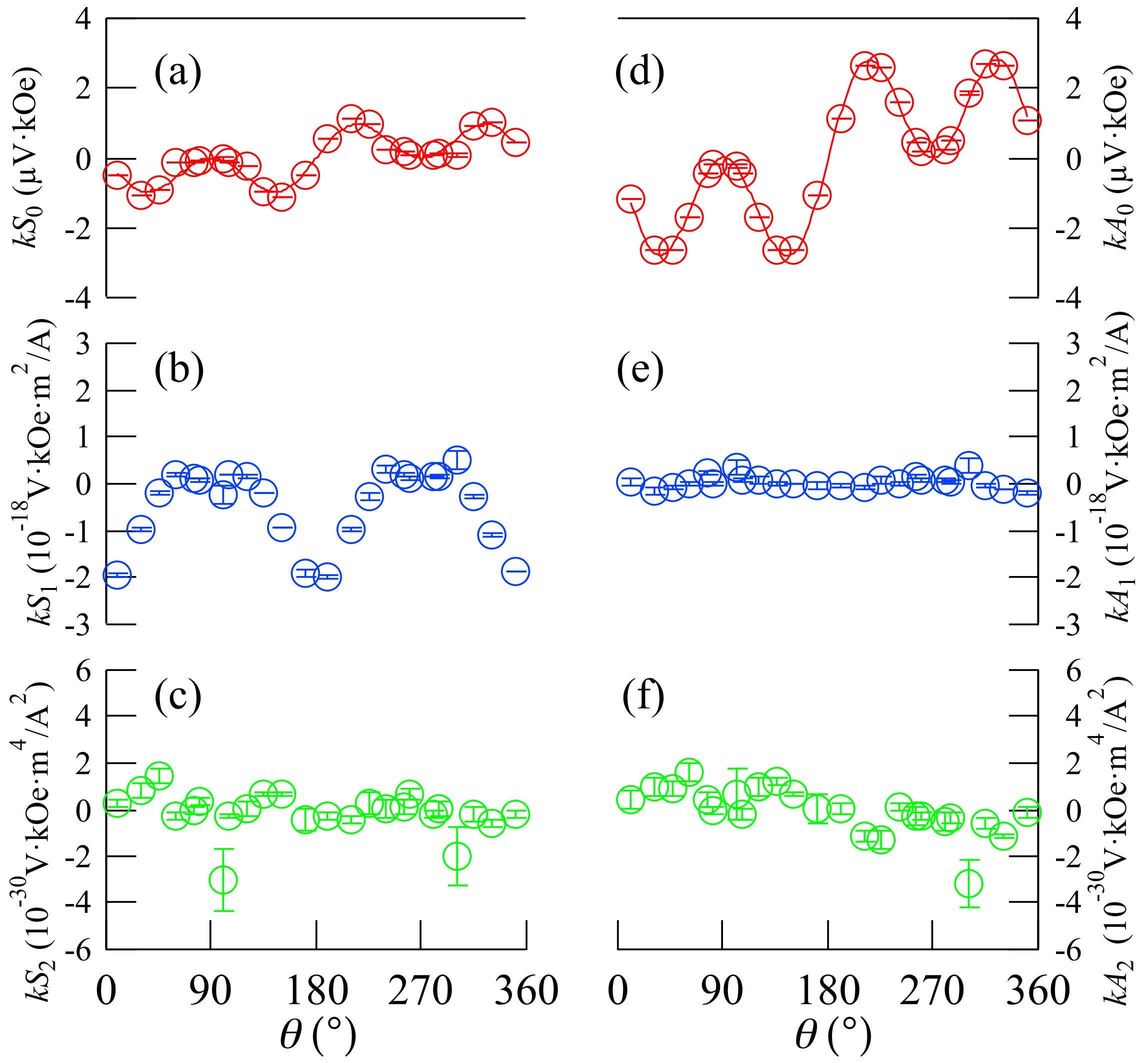

Figure 5.3.2 the expanded elements in the polynomial equation on $SiO_2$ substrate

Figure 5.3.3 show the *S*/*A* on the direct current in Pt at θ = 10° and 45° on the sapphire and thermally oxidized non-doped Si substrate. As is obviously seen in the figure, the evaluated *S*/*A* show almost the same values on the sapphire and $SiO_2$ substrate, which confirms that the effects of thermal flows and the effects modified by changing the substrates are not related to $kS_1$. Namely, these data denies our expectations.

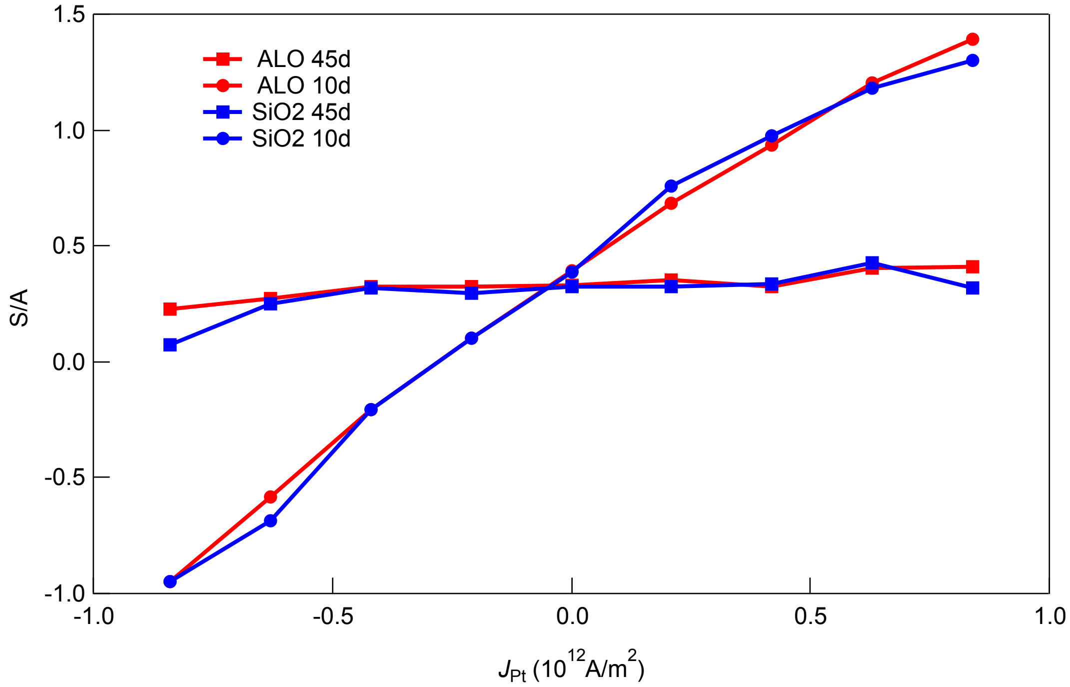

Figure 5.3.3 *S*/*A* on the direct current in Pt at $\theta = 10$ and 45° on the sapphire and $SiO_2$ substrate.

## 5.4 Restriction of Electrical Spin Injection by Inserting $SiO_2$ Layer

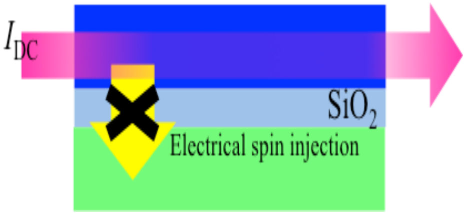

Figure 5.4.1 the schematic illustration on the restriction of electric spin injections by the inserting the insulator.

In general, ST-FMR has two sources for a resonance: spin transfer torques and torques from the magnetic fields. Figure 5.4.1 show the schematic illustration on restriction of the spin injection from Pt into Py by inserting the insulator. Insertion of non-magnetic insulator such as $SiO_2$ enables to restrict electrical spin injection from Pt to Py and enable us naively to expect zero signals in $kS_0$ and $kS_1$. In this section, I describe the analysis with a polynomial expansion for ST-FMR spectra in Py/$SiO_2$ (3 nm)/Pt films.

Before the main description on the anomalous modulation in symmetric components, I would like to show the magnetic properties of Py/$SiO_2$/Pt films on a sapphire substrate. Figure 5.4.2 shows the magnetic hysteresis loop for the trilayers characterized by using VSM. The observed saturation magnetization $M_s$ is slitely larger than that of Py/Pt bilayer film because the $SiO_2$ insertion layer can protect each layer from the intermixing effect near the interface. Interestingly, the coercivity for in-plane configuration the films is just zero, which means that the film possess the weak but observable interface perpendicular magnetic anisotropy. The weak interface perpendicular magnetic anisotropy is more clearly shown in the Py/$SiO_2$ films on a sapphire substrate shown in figure 5.4.3. The reasons are not clear yet.

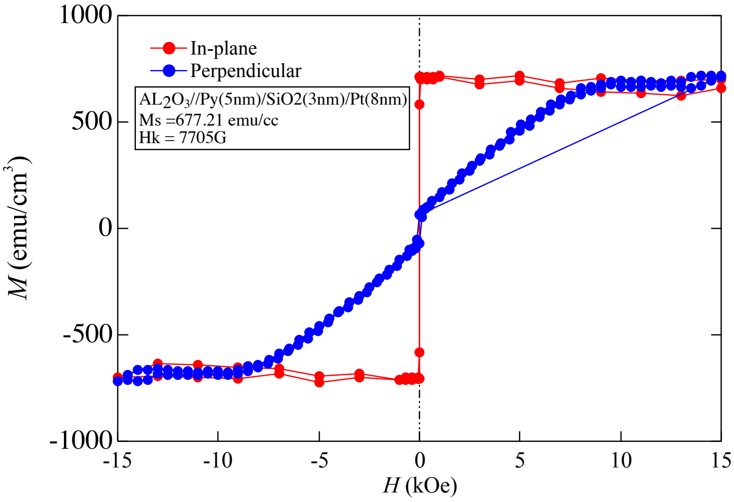

Figure 5.4.2. the saturation magnetization as a function of magnetic field in Py/$SiO_2$/Pt on a sapphire substrate.

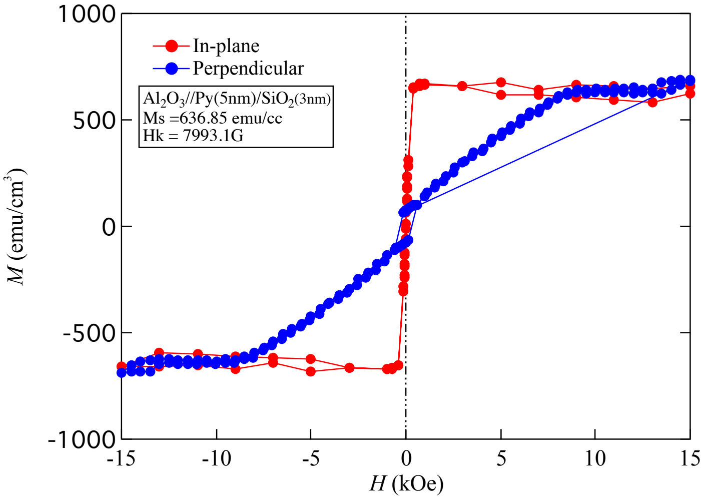

Figure 5.4.3. the saturation magnetization as a function of magnetic field in Py/$SiO_2$ on a sapphire substrate.

Figure 5.4.4 shows the damping parameter as a function of an in-plane relative angle in Py/$SiO_2$/Pt films. The obtained damping parameter in Py/$SiO_2$/Pt films is 0.001 which is compared to that in previous reports. In addition, the obtained value is half of that in Py/Pt films, which demonstrate that the path of a spin pumping effect is restricted and spin injection due to rf-current is also suppressed. The results allow us to expect the reduction of $kS_0$ in the films because the spin pumping effect is characterized by the spin injection by the rf-current. Figure 5.4.5 shows the effective damping modulation divided by direct currents as a function of an in-plane relative angle. As is seen clearly, the damping modulation due to direct currents is not observed, which demonstrates spin injection due to direct current is also restricted as well by the $SiO_2$ insertion layer. The results allow us to expect the observed $kS_1$ would be zero if the origin of $kS_1$ is the electric spin injection due to direct currents flowing in Pt.

Figure 5.4.6 shows the in-plane relative angle dependence of the expanded elements of (a) $kS_0$, (b) $kS_1$, (c) $kS_2$, (d) $kA_0$, (e) $kA_1$ and (f) $kA_2$ in Py/SiO$_2$/Pt films, respectively. $kA_0$ shows the $\sin2\theta\cos\theta$ dependence while kS0 does not show any signals, which suggests that a field excitation survives and the excitation due to spin transfer torque caused by spin Hall effect is suppressed. The feather of $kS_0$ is consistent with the obtained damping parameter and effective damping modulation shown in figure 5.3.1 and 5.3.2, respectively. In contrast to the disappearance of $kS_0$, $kS1$ shows the same in-plane relative angle dependence and, moreover, the intensity is comparable to that in Py/Pt films, which suggests that the direct currents not in Pt but in Py is related to $kS_1$.

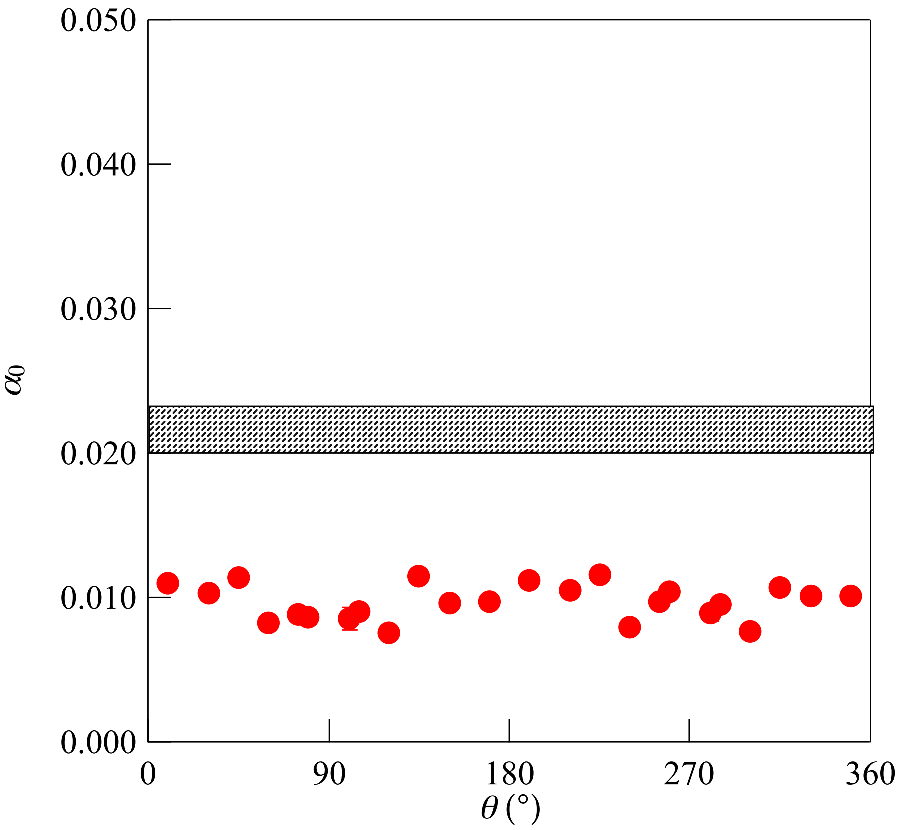

Figure 5.4.4 the damping parameters of Py/SiO2/Pt films on a sapphire substrate on the relative angles. Dashed area shows the damping parameter in Py/Pt films

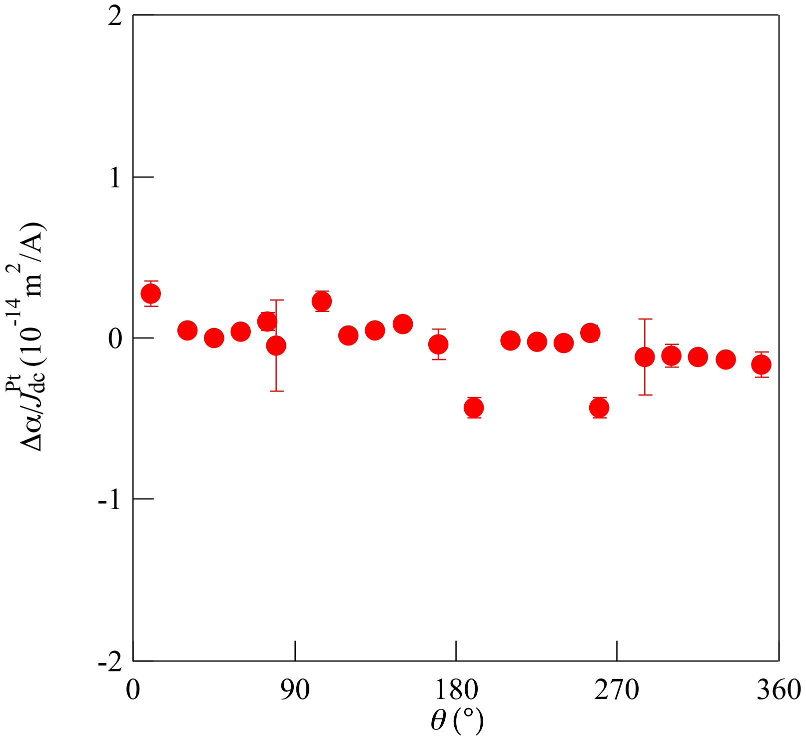

Figure 5.4.5 the damping modulation factor in Py/SiO$_2$/Pt films on a sapphire substrate

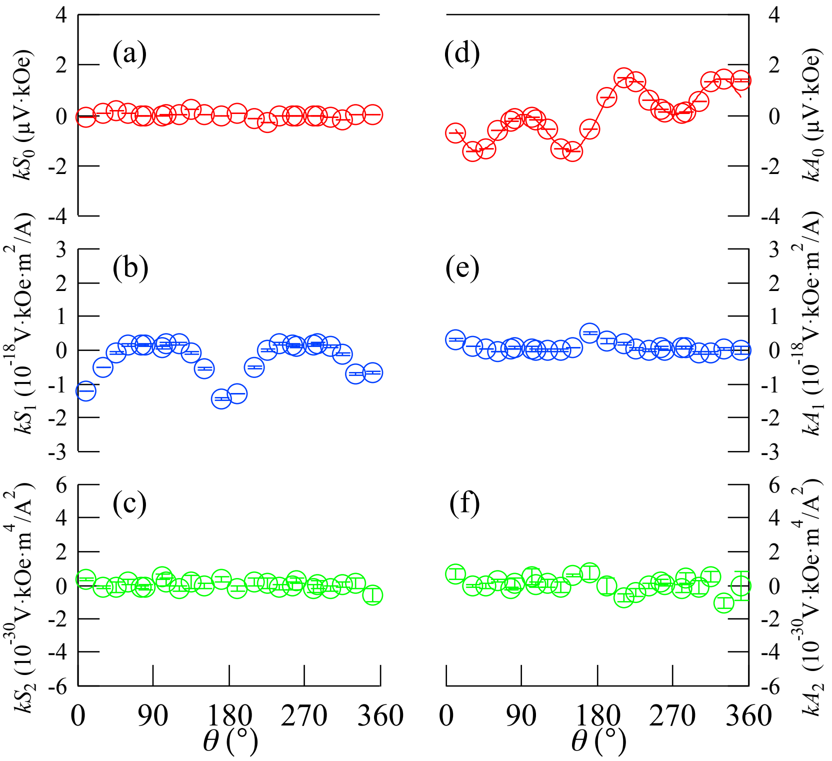

Figure 5.4.6 expanded components in Py/SiO$_2$/Pt films in a sapphire substrate.

### 5.5 Discussion

In the last section, it is suggested that direct currents flowing in Py characterize the anomalous modulation in symmetric component, $kS_1$, with in-plane relative angle dependence. Namely, I will discuss the expectation that the interplay between direct currents flowing in Py and magnetization dynamics induces the anomalous modulation of symmetric components on the intensity (shown in figure 5.4.1).

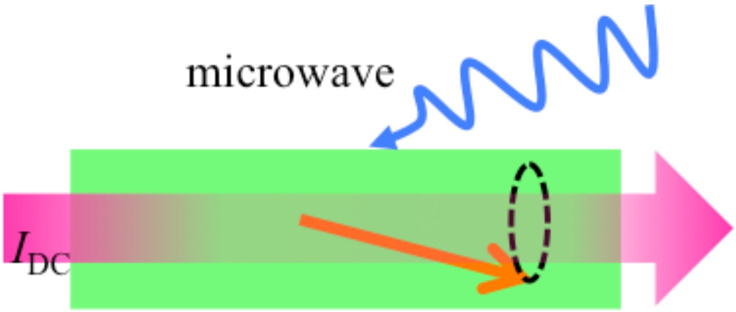

Figure 5.5.1 the schematic illustration on the interplay between direct current and magnetization dynamics.

AMR induced photoresitance is plausible effect because the effect occurs under the coupling of direct current in a ferromagnetic metal and magnetization dynamics and the amplitude is linear proportional to an intensity of direct currents [9-11]. The photoresistance effect was demonstrated by M.V. Costache et al. in 2006 shown in figure 5.5.2 by using different configuration form our set-up [9]. In their report, a coplanar stripe waveguide is employed to introduce rf magnetic field, and direct current is applied direct into Py single layer. The output voltage is detected by using 4-terminal detection. In their configuration, the rf and dc current are separately applied, and also the detection has specific path. On the other hand, rf, dc currents and the detection paths are identical in our sample shown in figure 5.5.3.

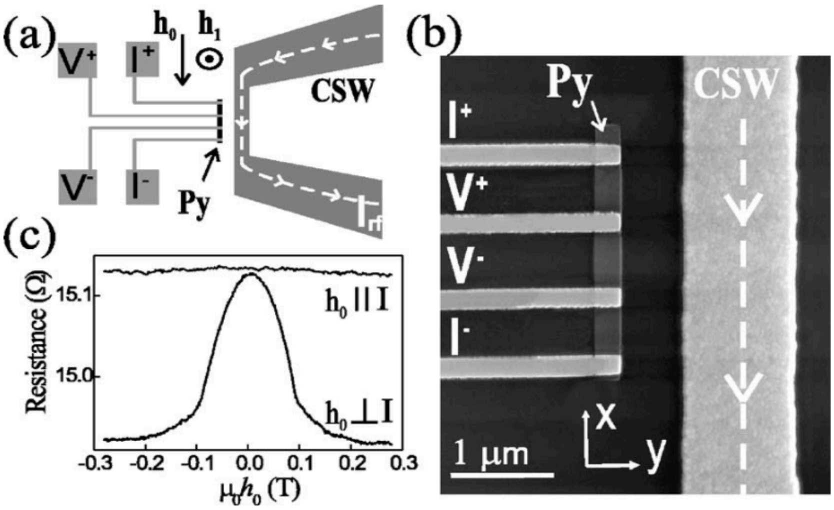

Figure 5.5.2 the device structures for the photoresistance effect in [9]. Reprinted figures with permission from M. V. Costache et al., Applied Physical Letters **89**, 232115 (2006), with the permission of AIP Publishing.

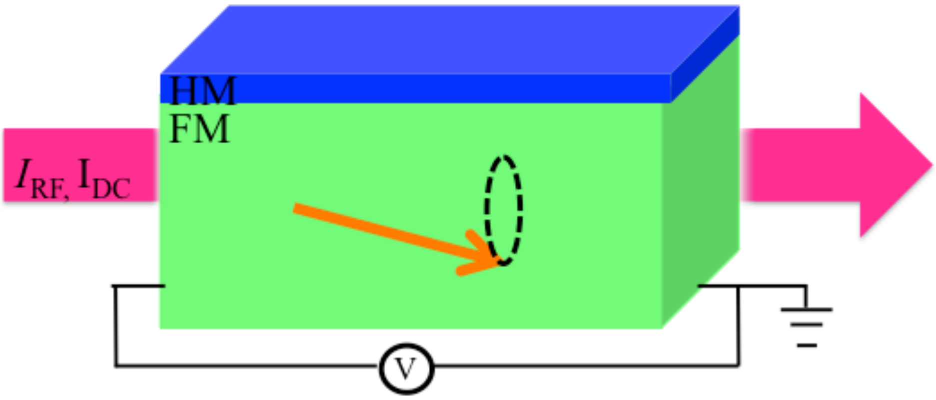

Figure 5.5.3 the schematic illustration for current and voltage path in our device.

In their report, output voltage induced by direct currents flowing into Py is proportional to the magnitude of direct currants shown in figure 5.5.4. the output voltage can be written as follows;$V_{\mathrm{Photo}} = A\frac{1}{(\gamma\mu_0/\varpi)^2(h_0-h_c)^2+\alpha^2}$. Here, $h_0$, $h_c$, $\alpha$ , $\omega$ and $A = (1/2)\Delta R(h_1/2h_c + m_s)^2\left(1+(\gamma\mu_0/\varpi)^2(h_c+N_y m_s)^2\right)I_{dc}$ are external magnetic field, resonant field, damping parameter, frequency and pre-factor of the photoresistance effect, respectively, and ΔR is the resistance change due to ARM effect. Thus, $V_{\mathrm{photo}}$ suggests output voltage can be proportional to the direct current flowing in Py.

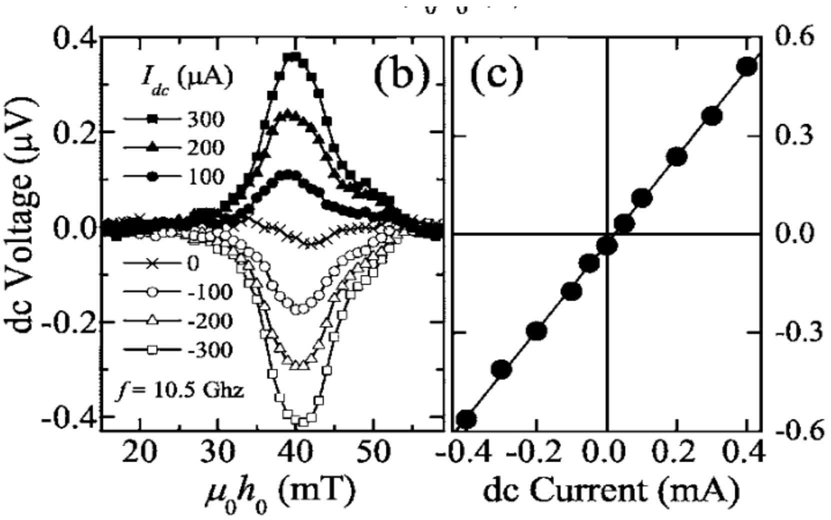

Figure 5.5.4 the photoresistance voltage demonstrated in [9].

Firstly, I would like to compare the photoresistance effect and rectification effect through AMR effects shown in figure 5.5.5. The photoresistance effect through AMR effects is reflected and induced by the change of the magnitudes of the magnetizations along the rotation axis between precessional state and saturated state (orange allow in the figure), and the change is probed by direct current. On the other hand, the rectification effects through AMR effects is directly reflected and induced by the state of the magnetization in the precession (dashed circle in the figure). Both of them allow us to detect as time-independent voltages.

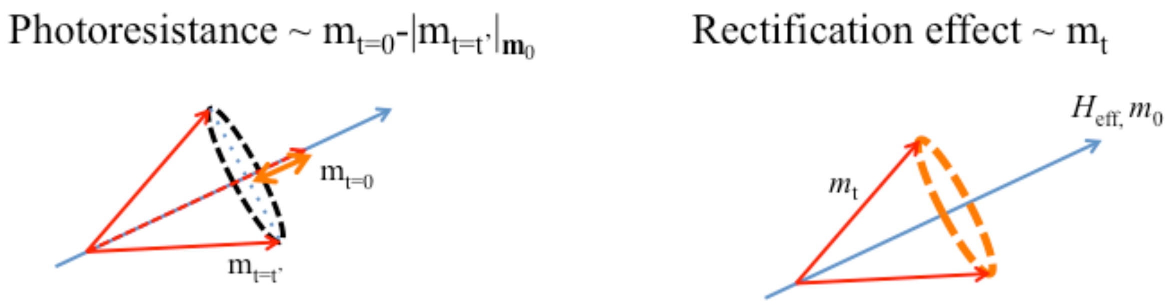

Figure 5.5.5 the schematic illustration for Photoresistance effect and rectification effect through AMR effects. The orange arrow and dashed circle induce the time-independent voltage.

In order to qualitatively describe the experimental results with AMR induced photoresistance, a numerical simulation based on the simple macro spin model is performed and shown in figure 5.5.6 (Courtesy of Dr. Kasai.). The numerical calculations at $\theta$ = 10° show that the AMR induced photoresistance effect is comparable to the AMR induced rectification effect, and the numerical calculations at $\theta$ = 45° show that AMR induced photoresistance effect is quite small compared to that of AMR induced rectification effect, which is in good agreements with the experimental results. Also, The intensity of AMR induced photoresitance is proportional to the amplitude of direct currents and the intensity itself is also comparable to the experimental results in the case that the applied direct current is around $1\times10^{11}\mathrm{A/m^2}$.

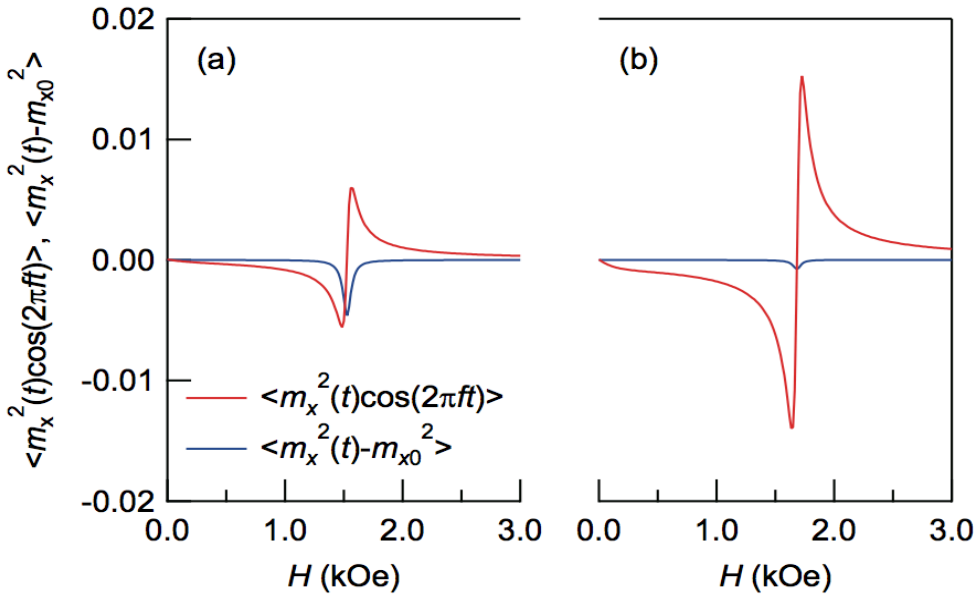

Figure 5.5.6 the numerical calculations for (Blue)the photoresistance and (Red) rectification effects through AMR effects at (a) $\theta$ = 10° and (b) 45°. The direct currents density in Pt is fixed at $1\bullet10^{11}\mathrm{A/m^2}$.

Moreover, the intensity as a function of the in-plane relative angle dependence shows a similar function to the experimental results as well shown in figure 5.7.7. the red and blue curves show the numerically calculated simulation on the rectification effect through the AMR effect and the photoresistance effect, respectively. The blue shows the curve with π-period with respect to in-plane relative angle which is consistent with the experimental data, while the red shows typical $\sin 2\theta \cos\theta$ function which is consistent with the conventional understanding on the ST-FMR. These results suggest that the numerical simulation could demonstrate the experimental data, which indicate that $kS_1$ could be described by the photoresistance effect.

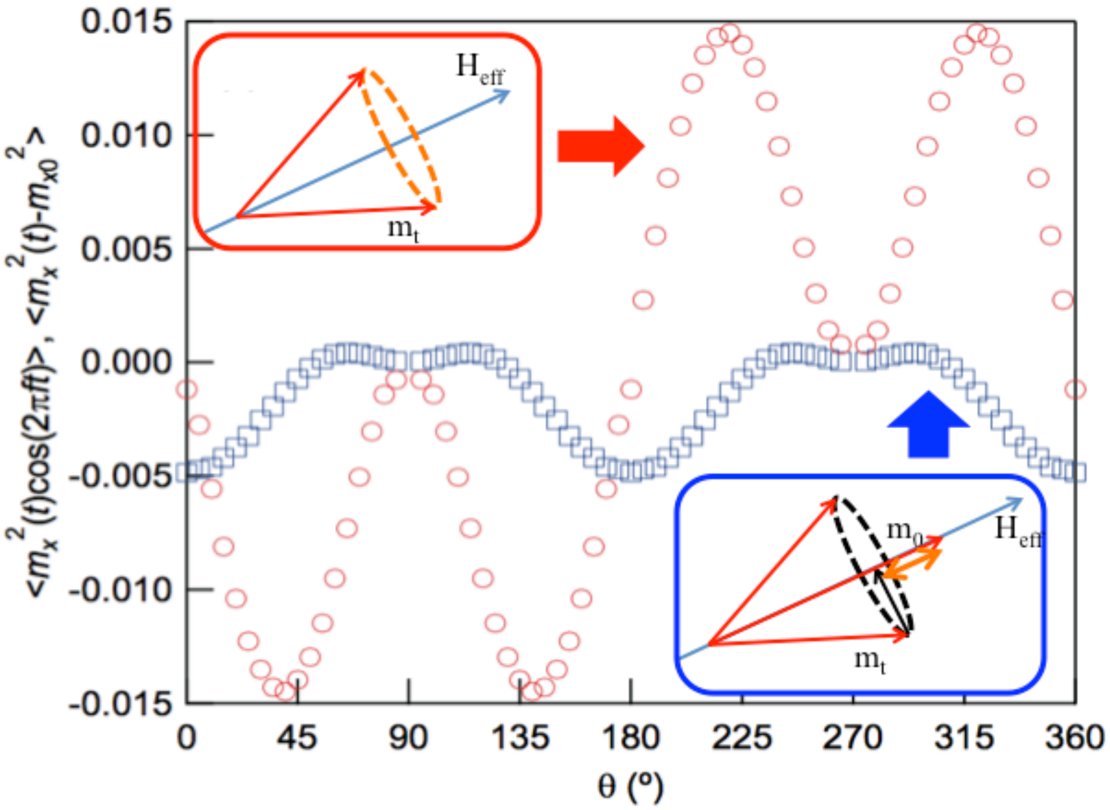

Figure 5.5.7 the numerical calculations for (Blue) the photoresistance and (Red) rectification effects through AMR effects on the relative angles. The direct currents density in Pt is fixed at $1 \cdot 10^{11}$ A/m$^2$.

## 5.6 Summary

In this chapter, the anomalous modulation on the intensity of ST-FMR spectra under direct currents. It is demonstrated that the modulation is linearly changed by magnitude of direct currents. The modulation is found in not only Py/Pt films but also Py/SiO$_2$/Pt films, which suggests that the phenomena is caused by the coupling of direct currents flowing in Py and magnetization dynamics. The AMR induced photoresistance is a plausible effect to describe the modulation and the effect can quantitatively demonstrate the experimental results from our numerical simulation.

## Reference

[1] L. Liu, T. Moriyama, D. C. Ralph, and R. A. Buhrman.
Spin-Torque Ferromagnetic Resonance Induced by the Spin Hall Effect.
Phys. Rev. Lett. **106**, 036601 (2011).

[2] K. Kondou, H. Sukegawa, S. Mitani, K. Tsukagoshi, and S. Kasai.
Evaluation of Spin Hall Angle and Spin Diffusion Length by Using Spin Current-Induced Ferromagnetic Resonance.
Appl. Phys. Express **5**, 073002 (2012).

[3] S. Kasai, K. Kondou, H. Sukegawa, S. Mitani, K. Tsukagoshi, and Y. Otani.
Modulation of effective damping constant using spin Hall effect.
Appl. Phys. Lett. **104**, 092408 (2014).

[4] K. Kondou, H. Sukegawa, S. Kasai, S. Mitani, Y. Niimi, and Y. Otani,
Influence of inverse spin Hall effect in spin-torque ferromagnetic resonance measurements.
Appl. Phys. Express **9**, 023002 (2016).

[5] J.-C. Rojas-Sánchez, N. Reyren, P. Laczkowski, W. Savero, J.-P. Attané, C. Deranlot, M. Jamet, J.-M. George, L. Vila, and H. Jaffrès.
Spin Pumping and Inverse Spin Hall Effect in Platinum: The Essential Role of Spin-Memory Loss at Metallic Interfaces.
Phys. Rev. Lett. **112**, 106602 (2014).

[6] Y. Wang, P. Deorani, X. Qiu, J. H. Kwon, and H. Yang.
Determination of intrinsic spin Hall angle in Pt.
Appl. Phys. Lett. **105**, 152412 (2014).

[7] W. Zhang, W. Han, X. Jiang, S. Yang, and S. S. P. Parkin.
Role of transparency of platinum–ferromagnet interfaces in determining the intrinsic magnitude of the spin Hall effect.
Nat. Phys. **11**, 496 (2015).

[8] K. Ando, S. Takahashi, K. Harii, K. Sasage, J. Ieda, S. Maekawa, and E. Saitoh.
Electric Manipulation of Spin Relaxation Using the Spin Hall Effect.
Phys. Rev. Lett. **101**, 036601 (2008)

[9] M. V. Costache, S. M. Watts, M. Sladkov, C. H. van der Wal, and B. J.van Wees,
Large cone angle magnetization precession of an individual nanopatterned ferromagnet with dc electrical detection.
Appl. Phys. Lett. 89, 232115 (2006).

[10] N. Mecking,Y. S. Gui, and C.-M. Hu,
Microwave photovoltage and photoresistance effects in ferromagnetic microstrips.

Phys. Rev. B 76, 224430 (2007).

[11] O. Mosendz, J.E. Pearson, F.Y. Fradin, G.E. W. Bauer, S.D. Bader, and A. Hoffmann
Quantifying Spin Hall Angles from Spin Pumping: Experiments and Theory
Phys. Rev. Lett **104**,046601 (2010).

[12] K. Uchida, S. Takahashi, K. Harii, J. Ieda, W. Koshibae, K. Ando, S. Maekawa, and E. Saitoh
Observation of the spin Seebeck effect
Nature **455**, 778 (2008)

[13] K. Uchida, J. Xiao, H. Adachi, J. Ohe, S. Takahashi, J. Ieda, T. Ota, Y. Kajiwara, H. Umezawa, H. Kawai, G. E. W. Bauer, S. Maekawa, and E. Saitoh
Spin Seebeck insulator
Nat. Mater. **9**, 894 (2010)

[14] K. Uchida, H. Adachi, T. Ota, H. Nakayama, S. Maekawa, and E. Saitoh
Observation of longitudinal spin-Seebeck effect in magnetic insulators
Appl. Phys. Lett. **97**, 172505 (2010)

[15] J. Flipse, F. L. Bakker, A. Slachter, F. K. Dejene, and B. J. van Wees
Direct observation of the spin-dependent Peltier effect
Nat. Nanotech. **7**, 166 (2012)

[16] J. Flipse, F. K. Dejene, D. Wagnaar, G. E. W. Bauer, J. Ben Youssef, and B. J. van Wees
Observation of the Spin Peltier Effect for Magnetic Insulator

# 6. Direct Currents Dependence of The Magnetic Properties Obtained by The Spin Torque Ferromagnetic Resonance in Py/Pt Films

The one-dimensional structure, so-called nano-wire, is mainly used for the study on propagating spin waves. I introduced and discussed the utility and merit of the one-dimensional structure, namely Py/Pt bilaer films possibly enable us to evaluate the cone angle of the magnetization dynamics [1-7]. Therefore, FM/HM bilayer films would widely be utilized to obtain magnetic properties under the magnetization dynamics. In this chapter, I would like to show the direct currents dependence of the magnetic properties obtained by ST-FMR such as the resonant field, the damping parameter and so on.

## 6.1 Direct Currents Dependence of The Resonant Field

Figure 6.1.1 shows the resonant fields on the relative angle with various magnitudes of direct currents. The resonant field can be fitted with sin2θ because the resonant field is derived from the magnetostatic energy E as follows [8], $E = -\frac{1}{2}M_s \cdot H_d \sim \frac{1}{2}(N_y - N_x)M_s^2 sin^2\theta$. Here, $M_s$, $H_d$, $N_y$ and $N_x$ are the saturation magnetization, the demagnetizing field, the demagnetization parameter for in-plane hard axis, and the demagnetization parameter for in-plane easy axis, respectively. The ferromagnetic resonance can detect effective magnetic fields so that anisotropy magnetic field is directly influenced to the resonant fields. Since the effective fields $H_{eff}$ can be descried as $H_{eff} = H_{ext} + H_{ex} + H_{sta} + H_{ani}$. Here, $H_{ext}$, $H_{ex}$, $H_{sta}$ and $H_{ani}$ are the external magnetic field, the exchange magnetic field, the magnetostatic field and anisotropy magnetic fields, respectively. The device can be considered to possess uniaxial anisotropy, and only the $H_{ani}$ has $\theta$ dependence. Thus, $H_0$ has consequently $\sin 2\theta$ dependence. By comparing the resonant fields with $I_{dc}$=-20.7 and 20.7 mA, it can be considered that the phase is 180°. It is in good agreement with the measurement condition, namely the generated Oersted fields have opposite direction compared to each other. The difference of the $H_0$ in the figure can be observed to be ~30 Oe at ~270°. On the other hand, the calculated deference by using $H_{Oe} = J_{HM}d/2$ is around 20 Oe. The resonant filed can be described by the kittle equation $\varpi = \gamma\sqrt{(H_0 + H_{Oe})(H_0 + H_d)}$. Here, $\omega$ is the fix parameter so that the right term should be constant, and $H_d$ is quite large compared to $H_{Oe}$. The resonant field can be simply considered to be $H_0$-$H_{Oe}$. Namely, the Oersted field generated by direct currents directly changes the resonant field. Thus, the Observed difference is in good agreement with the simple calculation.

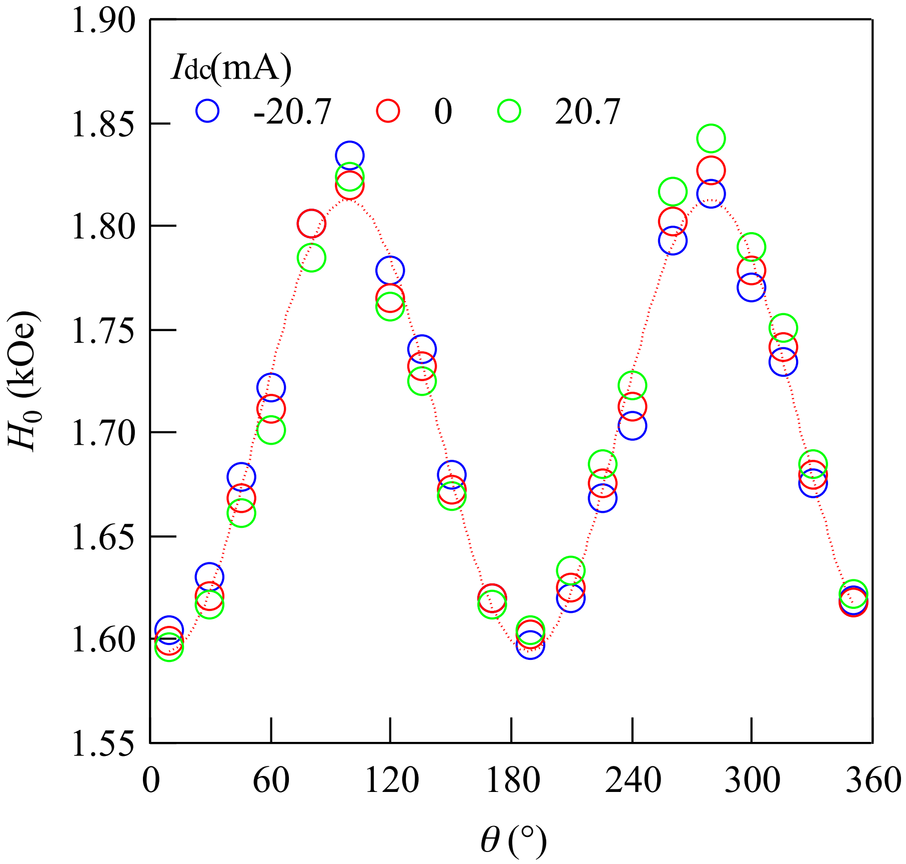

Figure 6.1.1 the resonant field on the relative angle with various direct currents

### 6.2 Direct Currents Dependence of the Half Width at Half Maximum

As shown in figure 1.9.3, the $\varDelta$ should be constant at any angle. However, the half width at half maximum $\varDelta$ shown in figure 6.2.1 is not constant on the relative angle $\theta$ for any direct currents case. If the in-plane magnetic anisotropy can not be ignored, $\varDelta$ can not be considered to be constant on θ [9-13]. According to the description in the reference 13 , $\varDelta$ show the largest value at $\theta_H \sim 30^\circ$. Here, $\theta_H$ is relative angle of magnetic field and direction normal to the film. Therefore, it is assumed that magnetic anisotropy is largest at $\theta_H = 0^\circ$, which may suggest that $\varDelta$ in my study show the large value with θ slightly tilted from 90° and 270°. While numerical consideration is not performed on the effect of the in-plane anisotropy, the angle dependence of Δ could be explained.

The $\varDelta$ on $I_{dc}$= -20.7 and 20.7 mA are almost symmetric at $\theta = 180^\circ$, which can be demonstrated by the effective damping modulation theory described in section 1.6.1 because $\varDelta$ can be modulated by injected spin transfer torques generated by direct currents flowing in Pt layer in this study.

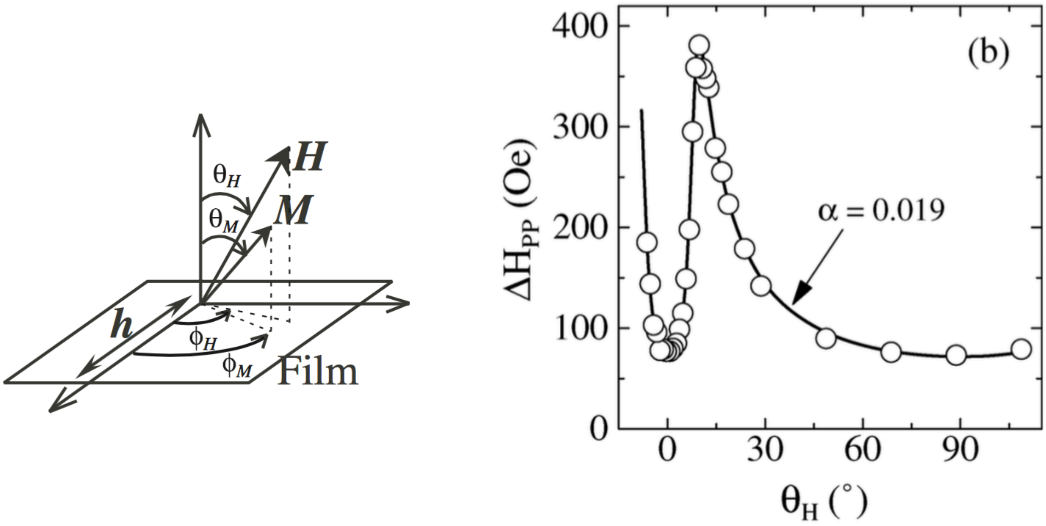

Figure 6.2.1 (Left) the schematic illustration of the coordinate system used in ref. 13(Right) the half width at half maximum on the $\theta_H$ shown in [13]. Copyright 2018 The Japan Society of Applied Physics.

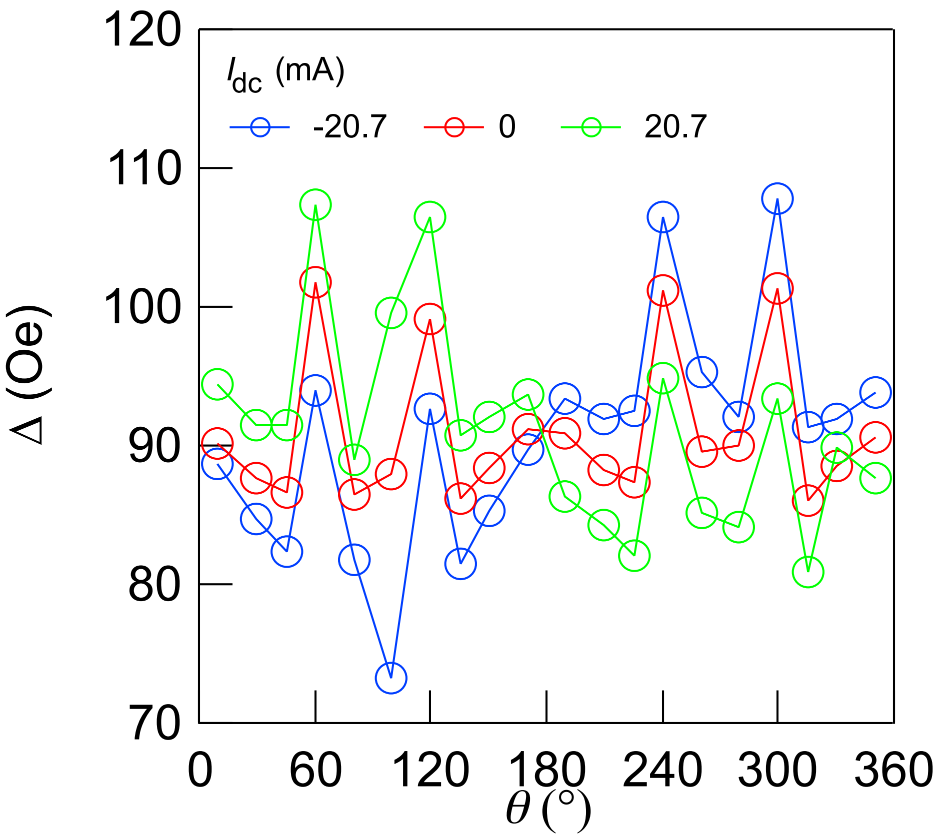

Figure 6.2.2 the half width at the half maximum on the relative angles with various direct currents.

## 6.3 Direct Currents Dependence of the Spin Hall Angles

Figure 6.3.1 shows the direct currents dependence of the spin Hall angles on the relative angle $\theta$ by evaluating the SIR method. The spin Hall angles evaluated by using the SIR can be described to be $\eta_{SIR} = t_{\mathrm{FM}} d_{\mathrm{HM}} \frac{S}{A} \frac{e\mu_0 M_{\mathrm{S}}}{\hbar} \frac{2\pi f}{\gamma H_{\mathrm{ext}}}$. As is shown in Figure 1.9.3, *S*/*A* that is proportional to $\eta_{SIR}$ is constant on the relative angle so that $\eta_{SIR}$ at $I_{\mathrm{dc}}$= 0 mA should be constant. However, $\eta_{SIR}$ at $I_{\mathrm{dc}}$=0 mA is not obviously constant, which is possibly affected by the other magnetic properties such as the magnetic anisotropy pointed out in the previous chapter and the low pre-factor k characterized by applied rf power. Increasing the pre-factor *k*, the amplitude of ST-FMR spectra increase, which enables us to accurately fit the ST-FMR curves and evaluate spin Hall angle.

At $I_{\mathrm{dc}}$= 20.7 and -20.7 mA, the evaluated spin Hall angle significantly increases and decrees in the regions of 0˚~30˚, 150˚~210˚, and 330˚~ 360˚, which is in good agreements with results shown in the previous sections. The evaluated spin Hall angles are finally varied from -0.016 to 0.10 in the direct currents range.

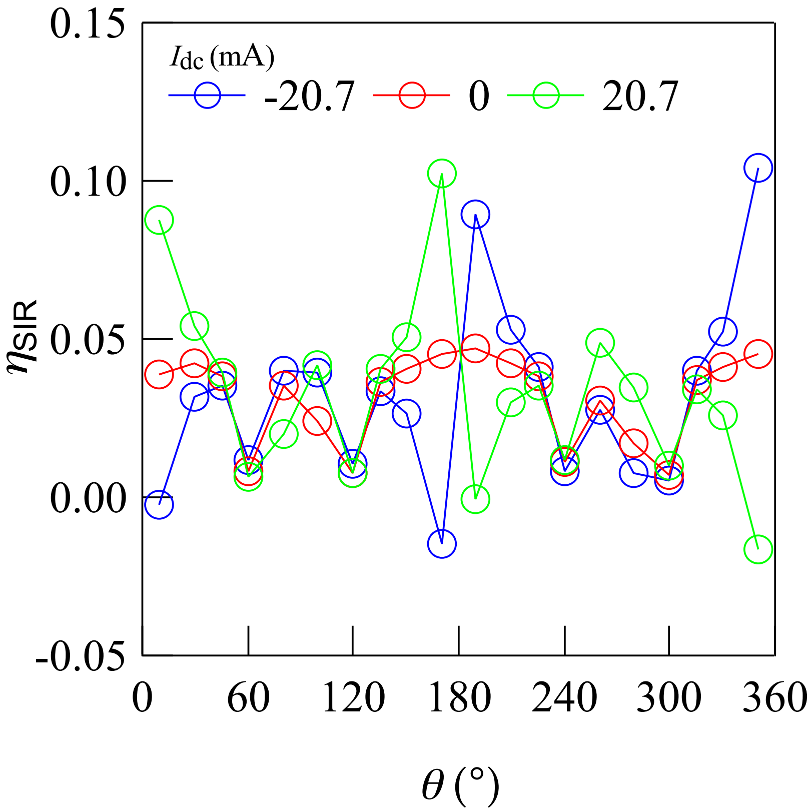

Figure 6.3.1 the spin Hall angles evaluated by using the SIR on the relative angle with various direct currents.

Figure 6.3.2 shows the spin Hall angles evaluated by using the EDM method. The evaluated spin Hall angles are almost constant at any angles except 10˚, 170˚, 190˚, and 350˚, and the value is around 0.04. The spin Hall angle evaluated by using the EDM method can be described to be $\eta_{\mathrm{EDM}} = \frac{(H_{\mathrm{ext}}+2\pi M_{\mathrm{eff}})\mu_0 M_{\mathrm{S}} t_{\mathrm{FM}}}{sin\theta} \frac{\Delta\alpha}{J_{\mathrm{DC}}^{\mathrm{HM}}}$. The equation indicates that the evaluated spin Hall angles should be constant at any angle. However, the evaluated spin Hall angles are inversely proportional to the sin$\theta$ so that the spin Hall angles at θ = 10˚, 170˚, 190˚, and 350˚ could be overestimated.

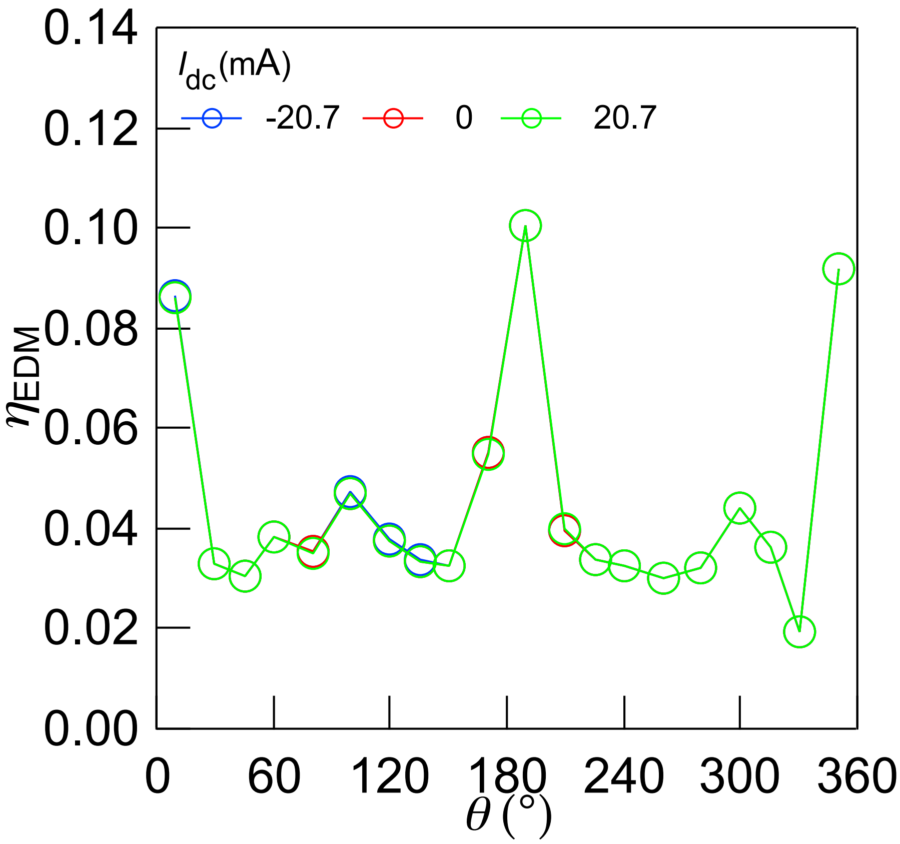

Figure 6.3.2 the spin Hall angles evaluated by using the EDM on the relative angle with various direct currents.

## 6.4 Summary

In this section, the direct currents dependence of the parameters obtained by ST-FMR spectra on the relative angle were shown. While the aforementioned parameters are constant on the relative angle in the conventional understanding, the obtained parameters are not so. That's because the in-plane magnetic anisotropy cannot be ignored in the sample whose width and length are 1 μm and 6 μm, respectively. As is mentioned in section 1.10, the developments of the spintronics device application require the devices with the width much narrower than 1μm so that we have to consider the in-plane magnetic anisotropy.

## Reference

[1] L. Liu, T. Moriyama, D. C. Ralph, and R. A. Buhrman.
Spin-Torque Ferromagnetic Resonance Induced by the Spin Hall Effect.
Phys. Rev. Lett. **106**, 036601 (2011).

[2] K. Kondou, H. Sukegawa, S. Mitani, K. Tsukagoshi, and S. Kasai.
Evaluation of Spin Hall Angle and Spin Diffusion Length by Using Spin Current-Induced Ferromagnetic Resonance.
Appl. Phys. Express **5**, 073002 (2012).

[3] S. Kasai, K. Kondou, H. Sukegawa, S. Mitani, K. Tsukagoshi, and Y. Otani.
Modulation of effective damping constant using spin Hall effect.
Appl. Phys. Lett. **104**, 092408 (2014).

[4] K. Kondou, H. Sukegawa, S. Kasai, S. Mitani, Y. Niimi, and Y. Otani,
Influence of inverse spin Hall effect in spin-torque ferromagnetic resonance measurements.
Appl. Phys. Express **9**, 023002 (2016).

[5] J.-C. Rojas-Sánchez, N. Reyren, P. Laczkowski, W. Savero, J.-P. Attané, C. Deranlot, M. Jamet, J.-M. George, L. Vila, and H. Jaffrès.
Spin Pumping and Inverse Spin Hall Effect in Platinum: The Essential Role of Spin-Memory Loss at Metallic Interfaces.
Phys. Rev. Lett. **112**, 106602 (2014).

[6] Y. Wang, P. Deorani, X. Qiu, J. H. Kwon, and H. Yang.
Determination of intrinsic spin Hall angle in Pt.
Appl. Phys. Lett. **105**, 152412 (2014).

[7] W. Zhang, W. Han, X. Jiang, S. Yang, and S. S. P. Parkin.
Role of transparency of platinum–ferromagnet interfaces in determining the intrinsic magnitude of the spin Hall effect.
Nat. Phys. **11**, 496 (2015).

[8] C. Kittel.
On the Theory of Ferromagnetic Resonance Absorption
Phys. Rev. **73**, 155 (1948).

[9] A. A. Hussain
The Angular Dependence Of The Main Spin-Wave Resonance Linewidth In Ferromagnetic Nickel Films
Physica B **162**, 321 (1990)

[10] S. Mizukami, Y. Ando, and T. Miyazaki
Effect of spin diffusion on Gilbert damping for a very thin permalloy layer in Cu/permalloy/Cu/Pt films

Phys. Rev B **66**, 104413 (2002)

[11] S.Mizukami, Y. Ando, and T.Miyazaki
Ferromagnetic resonance linewidth for NM/80NiFe/NM films (NM = CU, Ta, Pd and Pt)
JMMM **226-230,** 1640 (2001)

[12] S.Mizukami, Y. Ando, and T.Miyazaki
Magnetic relaxation of normal-metal (NM)/80NiFe/NM films
JMMM **239**, 42 (2002)

[13] S.Mizukami, Y. Ando, and T.Miyazaki
The study on ferromagnetic resonance linewidth for NM/80NiFe/NM (NM =Cu, Ta, Pd and Pt) films
Jpn. J. Appl/ Phys. **40**, 580 (2001)

## 7. Summary

The spin Hall effect induced ST-FMR was studied for Py/Pt bilayer films in the framework of the SIR and EDM methods, as well as the interface perpendicular magnetic anisotropy. The major finding in this study is that anomalous direct current modulation occurs in the ST-FMR spectra with the small relative angles between the external field and the exciting electric current. The anomalous modulation appears only in the symmetric part of the spectra. Interestingly, the EDM method gives the correct spin Hall angle of Pt even for the spectra modulated anomalously, suggesting that the EDM method is much beneficial in evaluating the spin Hall angles. The anomalous modulation found in this study can be attributed to the photoresistance-like effect. The results obtained in this study are summarized as follows:

(1) The interface perpendicular magnetic anisotropy was investigated by using the vibrating sample magnetometer and the ST-FMR method. The interface perpendicular magnetic anisotropy energy of 0.17 erg/cm$^2$ was obtained based on the so-called dead layer model, in which the magnetic dead-layer thickness was estimated to be of 0.63 nm.

(2) Based on the results of magnetization measurements, the validity of the dead layer model was discussed. A possibility that the dead layer model over-estimated the interface perpendicular magnetic anisotropy was suggested.

(3) The spin Hall effect induced ST-FMR was systematically investigated. In the case when the relative angle between the external magnetic field and the exciting electric current was 10˚, anomalous direct current modulation was found in the ST-FMR spectra. It was also confirmed that the anomalous modulation appeared only in the symmetric part of the spectra, which lead the unphysical and unreasonable behavior of the effective spin Hall angle by SIR. It was also confirmed that no anomalous behavior was observed at the relative angle between the magnetic field and the electric current of 45˚, which is conventionally used in the ST-FMR.

(4) The spin Hall angle determined by the EDM method was reasonable ($\theta_{\mathrm{SHE}} = 0.034$) even for the ST-FMR spectra modulated anomalously. This fact showed that the EDM method is advantageous for the evaluation of the spin Hall angles.

(5) In order to elucidate the mechanism of the anomalous direct current modulation at the small angle of the magnetic field and the current, thermal effects were examined by changing the thermal conductivity of the substrates and by implementing the poly-nominal expansion of the modulation intensity on the current density. The results showed that the thermal effect was excluded for the mechanism of the anomalous modulation.

(6) Based on numerical calculations using a macro-spin model, the anomalous direct current modulation of the ST-FMR spectra was attributed to the photoresistance-like effect. The results may lead to a new way to characterize the cone angle in the magnetization dynamics.

(7) The influence of the applied direct currents to the magnetic properties was observed. The influence to the resonant fields could be described by the magnetostatic energy, while that to the half width at half maximum could not described well. The in-plane magnetic anisotropy was possible reason, and it is not negligible so that the half width at half maximum was not in agreement with the convectional understanding, which consequently make it difficult to more accurately estimate the spin Hall angle by EDM.

# Appendix

## A Microfabrication

### A.1 Top-down process

Top-down process requires preparing a thin film prior to the microfabrication process. At the first step, negative tone resist is spin-coated and backed to optimize the condition for a subsequent lithography step. Baking process can make resist evaporated and get thin. After an exposure with electron beam or light for pattering a device and then development and removal of the resist exposed to electron beam or light, Ar-ion etching is performed to remove the thin firm. Finally, the resist that still remains on the thin film is removed by using acid. In the case of negative tone resist, the resist is made to get insoluble to its developer due to an exposure. Namely, resists at the unexposed area are easily solved to the developer and the designed pattern can be formed as electron beam and light are radiated.

In this study ma-N1407 for electron beam lithography (EBL) and ma-N2403 for photolithography (PL) with HMDS as promoter. In order to prevent electron charge-up during performance of EBL ESPACER was also on top of PMMA employed.

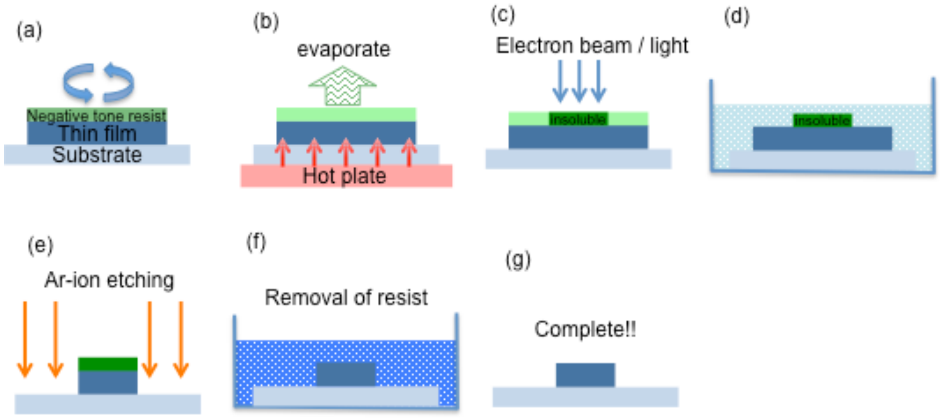

Figure A the schematic illustration of the flow chart on the top-down process

## A.2 Bottom-up process

Bottom-up process is available not only directly to a substrate but also to a thin film. In contrast to the top-down process, positive tone resist is used because it is secured to make space for deposition positive tone resist is spin-coated and backed. After exposure and development, a deposition process is required for forming a designed pattern. Finally, the remaining resist is removed. In the case of positive tone resist, the resist is made to get soluble to its developer due to an exposure in contrast to negative tone resist. Therefore, the exposed area allows the deposition and formation of the designed pattern after development.

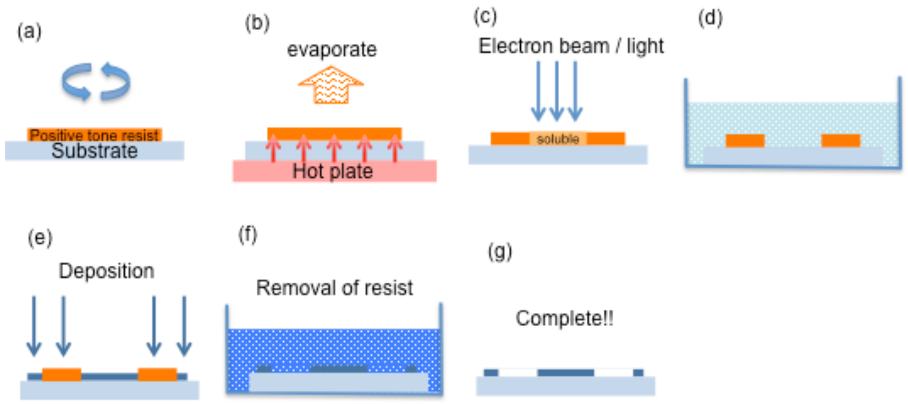

Figure B the schematic illustration of the flow chart on the bottom-up process

# Acknowledgment

First and foremost, I would like to express my profound gratitude to my supervisor, Prof. S. Mitani. I would like to appreciate for the advice, supports, discussions, and supervision of Prof. Mitani since I came to Spintronics group, National Institute for Materials Science/University of Tsukuba in 2011 as a master student over seven years. He has taught me how researcher think about a research, have a attitude to a own research, and make a scientific document such as a paper and presentation material. I also thanks to his humor and jokes that always make me relaxed and happy.

I am grateful to the six-committee members of my Ph.D thesis, Prof. S. Mitani, Prof. K. Hono, Prof. H. Yanagihara, Prof. S. Uji, Prof. S. Kuroda and Dr. S. Kasai for the evaluation of contents of my presentation and thesis. Especially, I would like to thank Dr. S. Kasai kindly for joining the committee and evaluating my thesis.

I would like to express my deep gratitude to my main collaborate and teacher, Dr. S. Kasai. He has given many talks about from fundamentally scientific to practical things. Now I aspire to be the scientist like him because he is significantly honest to science and, moreover, his experimental skills are extremely high-level. I respect himself and also his skills and intelligence.

I would like to thank Dr. H. Sukegawa for his advice. His logical talk based on his experiences always makes me convinced and encouraged and also have me find what I have to study. I will never forget the Takoyaki/Gyoza parties he kindly arranged in his house.

I would like to thank to other staffs in Research Center for Magnetic and Spintronic Materials. Because of their help and advice, I have learned how to use the state-of-art experimental equipment. I also thank Ms. A. Tomaru. She always helps me make business and financial documents.

I would like to thank colleagues and friends I have met in NIMS, especially Dr. J.W.Koo, Dr. Ikhtiar, and Dr. T. Scheike. I have spent longer time with the above three friends probably because they are quite strange and nice guys.

I thank to financial support from NIMS which have made me concentrated on my research and enabled me to realized successful achievements including three papers and Ph.D.

Finally, I really thank my family for supporting me during my student life in Tsukuba for seven years. I appreciate that my grandfather and grandmother have believed my brilliant future, my father and mother kindly have allowed me to keep studying in the Ph.D course, and nieces and nephews have given me lovely smiles.

Finally, again, I deeply thank all people who have supported me in my life ever. Without their support and help, I could not obtain the Ph.D.

## Publications

### Reports

1) Shigeyuki Hirayama, S. Mitani, Y. Otani, and S. Kasai
"Detection of higher order contribution in spin Hall induced ST-FMR measurement"
Applied Physics Express (To be submitted)

2) Shigeyuki Hirayama, S. Kasai, and S. Mitani
"Interface perpendicular magnetic anisotropy in ultrathin Ta/NiFe/Pt layered structures",
Japanese Journal of Applied Physics **57**, (2018). (Accepted)

3) Shigeyuki Hirayama, S. Mitani, Y. Otani, and S. Kasai
"Anomalous modulation of spin torque-induced ferromagnetic resonance caused by direct currents in permalloy/platinum bilayer thin films",
Applied Physics Express **11,** 013002 (2018).

-----Master course-----

4) S. Kasai, Shigeyuki. Hirayama, Y. K.Takahashi, S. Mitani, K. Hono, H. Adachi, J. Ieda, and S. Maekawa
"Thermal engineering of non-local resistance in lateral spin valves"
Applied Physics Letters **104,** 162410 (2014).

5) Y. K. Takahashi, S. Kasai, Shigeyuki Hirayama, S. Mitani and K. Hono
"All-metallic lateral spin valves using $Co_2Fe(Ge_{0.5}Ga_{0.5})$ Heusler alloy with a large spin signal"
Applied Physics Letters **100,** 052405 (2012).

### Conferences

1) Shigeyuki Hirayama, S. Kasai and S. Mitani
"Influence of dc-bias current on spin transfer torque ferromagnetic resonance in NiFe/Pt bilayer"
61st Annual Conference on Magnetism and Magnetic Materials Oct. 31-Nov. 4, 2016
New Orleans, Lousiana

2) Shigeyuki Hirayama, S. Kasai, and S. Mitani
"Modeling and evaluation of interface perpendicular magnetic anisotropy in Ta/NiFe/Pt trilayers"
2016 International Conference on Solid State Devices and Materials Sep. 26-29, 2016
Tsukuba, Japan

3) 平山重之 、葛西伸哉、三谷誠司
“Ta/NiFe/Pt 三層膜の界面垂直磁気異方性の評価”
第40回日本磁気学会学術講演会 2016/9/5-8 金沢大学

4) 平山重之 、葛西伸哉、三谷誠司
“アンチドット格子におけるスピン流誘起強磁性共鳴”
日本物理学会第70回年次大会、 2015/3/21-24 早稲田大学

5) 平山重之 、葛西伸哉、三谷誠司
“Systematic measurements of transport properties in permalloy-based lateral spin valve”
第７４回応用物理学会秋季学術講演会、 2013/9/16-20 同志社大学

6) Shigeyuki Hirayama, S. Kasai, Y. K. Takahashi, S. Mitani, and K. Hono
“Effect of buffer layers on non-local transport properties in lateral spin valves”
The 8th International Symposium on Metallic Multilayers. May 19-24, 2013 Kyoto, Japan

-----Master course-----

7) 平山重之、高橋有紀子、葛西伸哉、三谷誠司
“面内型スピンバルブ素子における非局所スピンシグナルの温度および物質依存性 I”
日本物理学会第67回年次大会、 2012 /3/24-27 関西学院大学

## Patent

1) 高橋有紀子 、アナアタクリシュナンスリニバサン 、ボラプラガタバラプラサド 、アマナボルルラジニカンス 、シンハジェイヴァーダン 、林将光 、古林孝夫 、葛西伸哉 、平山重之 、三谷誠司 、宝野和博 No. 5696990 Ｃｏ２Ｆｅ基ホイスラー合金とこれを用いたスピントロニクス素子 (2015)